

RD-R180 197

USAF/SCEEE (SOUTHERN CENTER FOR ELECTRICAL  
ENGINEERING EDUCATION) AIR. (U) SOUTHERN CENTER FOR  
ELECTRICAL ENGINEERING EDUCATION INC S. H D PEELE

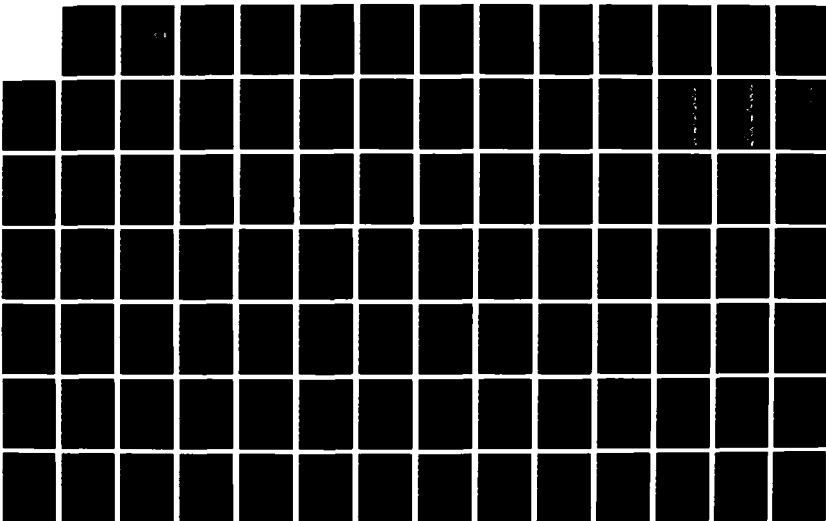
1/2

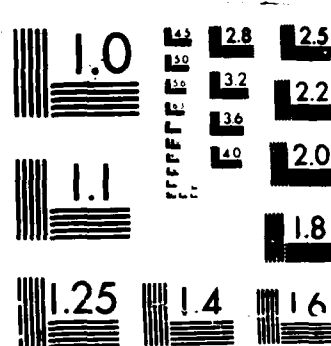
UNCLASSIFIED

NOV 86 AFGL-TR-87-0038 F19628-83-C-0097

F/G 7/4

NL





MICROCOPY RESOLUTION TEST CHART  
NATIONAL BUREAU OF STANDARDS 1964A

DTIC FILE COPY

12

AFGL-TR-87-0038

AD-A180 197

Title: USAF/SCEEE Air Force Geophysics Scholar Program 1985-1986

Editor: Professor Warren D. Peele

Southeastern Center for  
Electrical Engineering Education (SCEEE)  
11th & Massachusetts Avenue  
St. Cloud, FL 32769

November 1986

DTIC  
ELECTED  
MAY 14 1987  
S D  
A D

Final Report

Period Covered: September 1, 1985 - August 31, 1986

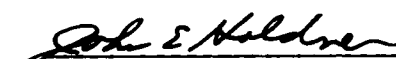
Approved for public release; distribution unlimited.

AIR FORCE GEOPHYSICS LABORATORY  
AIR FORCE SYSTEMS COMMAND  
UNITED STATES AIR FORCE  
HANSOM AIR FORCE BASE, MA 01731

"This technical report has been reviewed and is approved for publication"

  
\_\_\_\_\_  
ADOLPH S. JURSA  
Contract Manager

FOR THE COMMANDER

  
\_\_\_\_\_  
JOHN E. HOLDNER, Lt Col, USAF  
Director of Research Services

This report has been reviewed by the ESD Public Affairs Office (PA) and is releasable to the National Technical Information Service (NTIS).

Qualified requestors may obtain additional copies from the Defense Technical Information Center. All others should apply to the National Technical Information Service.

If your address has changed, or if you wish to be removed from the mailing list, or if the addressee is no longer employed by your organization, please notify AFGL/DAA, Hanscom AFB, MA 01731. This will assist us in maintaining a current mailing list.

Do not return copies of this report unless contractual obligations or notices on a specific document requires that it be returned.

## Unclassified

SECURITY CLASSIFICATION OF THIS PAGE

## REPORT DOCUMENTATION PAGE

1a. REPORT SECURITY CLASSIFICATION Unclassified		1b. RESTRICTIVE MARKINGS	
2a. SECURITY CLASSIFICATION AUTHORITY		3. DISTRIBUTION, AVAILABILITY OF REPORT Approved for public release; distribution unlimited.	
2b. DECLASSIFICATION/DOWNGRADING SCHEDULE			
4. PERFORMING ORGANIZATION REPORT NUMBER(S)		5. MONITORING ORGANIZATION REPORT NUMBER(S) AFGL-TR-87-0038	
6a. NAME OF PERFORMING ORGANIZATION Southeastern Ctr for Electrical Engineering Education (SCEEE)	6b. OFFICE SYMBOL (if applicable)	7a. NAME OF MONITORING ORGANIZATION Air Force Geophysics Laboratory	
6c. ADDRESS (City, State and ZIP Code) 11th & Massachusetts Avenue St. Cloud, FL 32769		7b. ADDRESS (City, State and ZIP Code) Hanscom AFB Massachusetts 01731	
8a. NAME OF FUNDING/SPONSORING ORGANIZATION	8b. OFFICE SYMBOL (if applicable)	9. PROCUREMENT INSTRUMENT IDENTIFICATION NUMBER F19628-83-C-0097	
8c. ADDRESS (City, State and ZIP Code)		10. SOURCE OF FUNDING NOS.	
		PROGRAM ELEMENT NO 62101F	PROJECT NO 9993
		TASK NO GE	WORK UNIT NO SP
11. TITLE (Include Security Classification) USAF/SCEEE Air Force Geophysics Scholars Program 1985-1986 (Unclassified)	12. PERSONAL AUTHORITY Warren D. Peete (Editor)		
13a. TYPE OF REPORT Final Report	13b. TIME COVERED FROM 9/1/85 TO 8/31/86	14. DATE OF REPORT (Yr, Mo, Day) 1986 November	15. PAGE COUNT 198
16. SUPPLEMENTARY NOTATION			
17. COSATI CODES	18. SUBJECT TERMS (Continue on reverse if necessary and identify by block number) Alkali Ions Line Coupling Fourier Transform Spectroscopy		
19. ABSTRACT (Continue on reverse if necessary and identify by block number)  Management and Technical Report describing the Air Force Geophysics Scholars Program at the Air Force Geophysics Laboratory. Covers the period from September 1, 1985 to August 31, 1986. Contains technical reports describing research work of eight scholars.			
20. DISTRIBUTION, AVAILABILITY OF ABSTRACT UNCLASSIFIED/UNLIMITED <input checked="" type="checkbox"/> SAME AS RPT <input type="checkbox"/> DTIC USERS <input type="checkbox"/>		21. ABSTRACT SECURITY CLASSIFICATION Unclassified	
22a. NAME OF RESPONSIBLE INDIVIDUAL A.S. Jursa		22b. TELEPHONE NUMBER (Include Area Code) (617) 377-3010	22c. OFFICE SYMBOL AFGL/CA

↓  
TABLE OF CONTENTS

1985-1986 Air Force Geophysics Scholar Program

Introduction	2
→ Collision Induced Electronic Transitions in $N_2^{(+)}$	3
→ Neutral Reactions in the Presence of Alkali Ions	25
→ Collisional Quenching of vibrationally excited NH IN $N_2^{\cdot}/H_2^{\cdot}$	49
→ Line Coupling in the Fundamental Q Branch of $CO_2^{\cdot}$ at 667 <del>CM-1</del>	53
→ Improving the Resolution of Infrared Spectral Lines From Fourier Transform Spectroscopy (FTS)	69
On the Tectonic Significance of the "Delayed Aftershock" Sequence Associated With the 1977 Sumba Earthquake	73
The SCRIBE Program: An Overview	152
Simulating Nonperiodic Systems	176



Accession For	
NTIS	CRA&I <input checked="" type="checkbox"/>
DTIC	TAB <input type="checkbox"/>
Unannounced <input type="checkbox"/>	
Justification	
By _____	
Distribution/	
Availability Codes	
Dist	Avail. <input type="checkbox"/> or Special <input type="checkbox"/>
A-1	

LIST OF RESEARCH REPORTS  
1985-86 USAF-SCEEE GEOPHYSICS SCHOLAR PROGRAM

<u>TITLE</u>	<u>RESEARCH ASSOCIATE</u>
1. Neutral Reactions In The Presence Of Alkali Ions	Dr. Carol Deakyne
2. Collision Induced Electronic Transitions In $N_2^+$	Dr. Anthony Dentamaro
3. Collisional Quenching of vibrationally Excited NH in $N_2/H_2$ Mixtures	Dr. Dorothy Flanagan
4. Line Coupling In The Fundamental Q Branch of CO <sub>2</sub> At 667 CM-1	Dr. Michael Hoke
5. Improving The Resolution of Infrared Spectral Lines From Fourier Transform Spectroscopy (FTS)	Dr. Samuel Howard
6. On The Tectonic Significance Of The "Delayed Aftershock" Sequence Associated With The 1977 Sumba Earthquake.	Dr. Robert McCaffrey
7. Report Delayed	Dr. John Mycroft
8. The Scribe Program: An Overview	Dr. George Tucker
9. Simulating Nonperiodic Systems	Dr. Earl Witt

1985-1986 USAF/SCEEE  
AIR FORCE GEOPHYSICS SCHOLAR PROGRAM

conducted by

Southeastern Center for  
Electrical Engineering Education

under

USAF Contract Number F19628-83-C-0097

MANAGEMENT AND TECHNICAL REPORT

submitted to

Air Force Geophysics Laboratory

Hanscom Air Force Base

Massachusetts, 01731

by

Southeastern Center for  
Electrical Engineering Education

November 1986

## 1985-1986 AIR FORCE GEOPHYSICS SCHOLAR PROGRAM

### INTRODUCTION

The Geophysics Scholar Program was initiated to provide research scholars with one year appointments to conduct research at the Air Force Geophysics Laboratory, Hanscom AFB, MA.

Extensive mailings were made to technical departments at universities around the United States where programs of prime interest to the Geophysics Laboratory were established. These included atmospheric studies, space science, geophysics, meteorology and related applied sciences.

Nine scholars were appointed during the period starting September 1985 and running through the end of the Contract on 31 August 1986. Two of these were continued in this Geophysics Scholar Program for a second year after having held scholar appointments under a previous contract.

The scholars attended 7 meetings or conferences during their appointment period. Several technical papers were presented by the scholars during the year. The final technical reports on the scholar's work are included in this report.

This program was judged a success by both the scholars and their laboratory associates. The opportunity of having new research people on a short term basis was felt to be very stimulating and worth while. Their interactions with the laboratory were very positive.

The program was scheduled to end during the summer of 1985 but was extended to 31 August 1986 in order to accommodate scholar continuation of 2nd year selectees from the 1984-85 program. As a result, there were only 9 scholars during the 1985-86 academic year.

1985-1986 AFGL-SCEEE GEOPHYSICS SCHOLAR PROGRAM

Sponsored by the

AIR FORCE GEOPHYSICS LABORATORY

Conducted by the

SOUTHEASTERN CENTER FOR ELECTRICAL ENGINEERING EDUCATION

FINAL REPORT

COLLISION INDUCED ELECTRONIC TRANSITIONS IN N<sub>2</sub><sup>+</sup>

Prepared by: Anthony V. Dentamaro

Research Location: Air Force Geophysics Laboratory  
LIU Division

AFGL Research Contact: Daniel H. Katayama

Date: 25 July 1986

COLLISION INDUCED ELECTRONIC TRANSITIONS IN  $N_2^+$

by

Anthony V. Dentamaro

ABSTRACT

An optical-optical double resonance technique is used to determine propensities for collision induced electronic relaxation by helium atoms from a specific  $A^2\Pi_{u1}(v=4, J)$  rotational level to the  $X^2\Sigma_g^+(v=7)$  manifold of  $N_2^+$ . The propensities for collisional transfer from this specific level to the nearly degenerate ( $\sim 0.04$  cm $^{-1}$  separation) spin components of the  $X(v=7)$  state are resolved by scanning the probe laser through the  $B^2\Sigma_u^+ - X^2\Sigma_g^+(5,7)$  band whose upper state is perturbed. The results show the propensities to be quite different and strongly dependent on the  $A(v=4,J)$  level initially populated by the pump lasers. The observation of these propensities for collisional electronic energy transfer through a large energy gap of approximately 1760 cm $^{-1}$  demonstrates the remarkable fact that this process occurs as fast or faster than rotational energy transfer through gaps of  $\sim 10$  cm $^{-1}$ . These results are found to be in qualitative agreement with theoretical relative cross-sections derived by Alexander and Corey [J. Chem. Phys. 84, 100(1986)] for inelastic collision induced transitions between  $2\Pi$  and  $2\Sigma$  electronic states of a diatomic molecule.

## I. Introduction

Selection rules for optical transitions in diatomic molecules are well documented and listed in the standard texts of molecular physics. However, very little is known even now about transitions in molecules due to collisions with atoms or other molecules. Although such collisions have been examined both theoretically and experimentally for many years, only recently have there been comprehensive studies of the resulting propensity rules. The majority of these experiments and models have been concerned with vibrational and rotational energy transfer, and very little has been done in the line of collision-induced electronic transitions.

Alexander and Corey<sup>2</sup> have expanded upon past work involving rotational transition propensity rules and have developed a quantum mechanical theory for  $2\Pi-2\Sigma$  collisional transitions. Predictions from earlier papers authored by Alexander<sup>3,4,5</sup> have been experimentally tested with the results being in generally good agreement with the theory. In particular, Daniel H. Katayama of AFGL has performed many of these tests, and during this past year we have examined the propensities for transitions in the A-X Meinel system of  $N_2^+$  when the collision partner is atomic helium<sup>6</sup>.

Both the quantum formulation and the experimental results show underlying dipole behavior in that there is a propensity toward  $\Delta J=0,\pm 1$  in these electronic transitions. Aside from this similarity, the agreement between theory and experiment is only fair. This is perhaps due to the fact that the quantum mechanical formulation does not explicitly depend on the form of the atom-molecule potential. Therefore, the next step would be to calculate cross sections for these transitions using a specific interaction between the  $N_2^+$  and He. Several possible forms exist for the missing potential. The

dipole behavior suggests a long-range attractive interaction, while the deviation from strict optical selection rules may indicate the existence of repulsive forces. Of particular interest is the collision complex model of bound atom-molecule states which allows for the inclusion of the energy gap. Thus far, collision complex models have been considered mainly for vibrational predissociation, but we feel that an electronic analogue is possible.

Cross sections and transition rates may be calculated numerically for any of these models, and our goal is to find the right potential to reproduce our recent experimental results.

## II. Objectives of the Research Effort

The primary goal of this past research period was to study collision-induced transitions in diatomic molecules and determine the resulting propensities. Specifically, we were interested in electronic transitions. Continuing work by Daniel H. Katayama at AFGL involved using an optical-optical double resonance technique in order to obtain rotational resolution in collision experiments.

Various theories of atom-molecule collisions exist which describe the different aspects of these interactions and yield a wide range of predictions for combinations of molecules, partners and energy levels; however, there has been no single general model which describe all of these systems. Certainly, no one approach is able to account for our observations. Incorporating the ideas of all of these models, our next objective was to choose a specific potential which was representative of the atom-molecule interaction and calculate the resulting cross sections for comparison with our experimental results for the  $\text{N}_2^+$ -He system.

### III. Experimental Method and Results

The two laser, double resonance system used to conduct the experiment is essentially the same as that described previously<sup>7,8</sup>. The "pump" and "probe" dye lasers are excited simultaneously by the green and UV light pulses, respectively, of a Nd:YAG laser. The pump laser with Rh 640 dye solution selectively populates a specific rotational level of the  $N_2^+ A^2_{\Pi_{u,i}} - X^2_{\Sigma_g^+}$  (4,0) band. The collision induced electronic transitions by helium atoms to the  $X^2_{\Sigma_g^+} (v=7)$  rotational manifold which lies approximately  $1760 \text{ cm}^{-1}$  lower in energy relative to the  $A (v=4)$  level are detected by scanning the probe laser with Coumarin 450 dye solution through the  $B^2_{\Sigma_u^+} - X^2_{\Sigma_g^+}$  (5,7) band. The  $N_2^+$  are formed by interacting nitrogen with helium metastable atoms downstream from a dc discharge. The nitrogen partial pressure is a few microns and the helium pressure is kept at a few Torr to produce a sufficient metastable concentration. Room temperature helium is the collision partner since the radiative decay curves from the  $A (v'=4)$  level are sensitive to pressure changes in helium and not nitrogen.

The probe laser scan of the B-X (5,7) band will resolve the nearly degenerate spin splitting of the  $X^2_{\Sigma_g^+} (v=7, N)$  rotational levels because the  $B^2_{\Sigma_u^+} (v=5)$  manifold is perturbed<sup>9,10</sup> by the  $A^2_{\Pi_{u,i}} (v=17)$  level of  $N_2^+$ . These perturbations not only cause shifts in the B state rotational levels but affect the relative intensities of the rotational structure in the probe laser scan of the  $B^2_{\Sigma_u^+} - X^2_{\Sigma_g^+} (5,7)$  band. The effects of these perturbations on the line strengths can be determined by<sup>11</sup>

$$S = (2J'+1)(2J+1) | C_{\Sigma} \begin{matrix} J' & 1 & J \\ 1/2 & 0 & -1/2 \end{matrix} + (\mu_1/\mu_2) [\epsilon C_{\Pi} \begin{matrix} 1/2 & 1/2 & -1 & 1/2 \\ 3/2 & 3/2 & -1 & -1/2 \end{matrix} - C_{\Pi} \begin{matrix} 3/2 & 3/2 & -1 & -1/2 \end{matrix}]|^2 \quad (1)$$

where  $\mu_1$  and  $\mu_2$  are transition moments between the  $X^2\Sigma_g^+(v=7)$  level and the  $A^2\Pi_u(v=17)$  and  $B^2\Sigma_u^+(v=5)$  states, respectively. The 3-j symbols in parentheses are evaluated using standard techniques<sup>12</sup>. The C coefficients are wavefunction mixing factors that can be determined<sup>9,10</sup> from the perturbation shifts, spacing between the unperturbed levels and the non Born-Oppenheimer matrix elements of the spin-orbit ( $\xi$ ) and orbit-rotation ( $\eta$ ) interactions,

i.e.

$$\xi = \langle A^2\Pi_u | AL_+ / 2 | B^2\Sigma_g^+ \rangle \quad (2)$$

and

$$\eta = \langle A^2\Pi_u | BL_+ | B^2\Sigma_g^+ \rangle . \quad (3)$$

The dominant factors in our case is the small value of the  $\mu_1/\mu_2$  ratio which is approximately<sup>13</sup> 0.03 and the fact that the rotational manifolds do not "cross"<sup>9,10</sup> which result in the intensities<sup>14</sup> of the perturbed  $R_1$  branch being reduced by only a few percent for the levels observed in our experiment. Indeed, Klynning and Pages<sup>9</sup> have failed in their attempts to observe "extra lines" due to this perturbation. These intensity changes are negligible for our present experimental results but should be considered in greater detail when the signal to noise ratio is substantially improved over our data.

Figures 1, 2, and 3 show probe laser scans of the same R branch portion of the B-X (5, 7) band with the pump laser tuned to the  $Q_1(6)$ ,  $P_1(8)$  and  $Q_2(8)$  transitions, respectively, of the A-X (4,0) band. The same helium pressure of approximately four Torr is used for these scans and the pump and probe laser pulses of about 20 ns duration are coincident in time to maximize single collision effects. The nearly degenerate spin components for the N rotational levels of the  $X^2\Sigma_g^+(v=7)$  level are clearly resolved in these

figures and the different intensity patterns demonstrate that propensities for collision induced electronic energy transfer are strongly dependent on the  $A^2\Pi_{u1}$  ( $v=4$ ,  $J$ ) level initially populated. The  $R_1$  and  $R_2$  branches refer to transitions from the  $F_1$  ( $J=N+1/2$ , e) and  $F_2$  ( $J=N-1/2$ , f) spin components, respectively, of the  $X^2\Sigma_g^+$  vibrational level and only even  $N$  values are observed because of the symmetric (s)  $\leftrightarrow$  antisymmetric (a) rule<sup>1,2,8</sup>. The e and f labels<sup>15</sup> refer to the upper and lower series of parity doublets, respectively.

#### IV. Theoretical Interpretation

The propensity for  $\Delta J = 0$  implies that optical selection rules may be important, but the significant intensities of the higher  $|\Delta J|$  lines indicate the presence of mechanisms beyond dipole transitions. Alexander and Corey<sup>2</sup> have developed a quantum mechanical description of inelastic collision induced transitions between  $2\Pi$  and  $2\Sigma$  electronic states of a diatomic molecule. Their theory of electronic transfer by collisions is an exact formulation but requires the use of approximations to yield propensity rules. They use an infinite order sudden (IOS) approximation, which assumes a short range potential and collision energies large with respect to the energy gaps. A Born approximation may be more appropriate for our experiment where the energy gap is not insignificant compared to collision energies. The results for relative intensity strengths, though, are similar in the two limits, indicating that the IOS approximation may be used to analyze our data.

Equations 52 and 55a<sup>2</sup> for the  $2\Pi$  state in Hund's case (a) coupling may be combined to yield the following expression for the cross section of a transition between  $2\Pi(J)$  and  $2\Sigma^+(J')$  rotational states of specific  $\epsilon(e/f)$  symmetry:

$$\sigma_{J\epsilon 2\Pi \rightarrow J'\epsilon' 2\Sigma} = \sum_{\Omega} k_{\Omega}(J, J') \sigma_{J=\Omega+1/2, \epsilon, 2\Pi \rightarrow J'=1/2, \epsilon, 2\Sigma} \quad (4)$$

where

$$k_{\Omega}(J, J') = 1/2 [1 - \epsilon \epsilon' (-1)^{J+J'+\Omega}] (2J'+1)(2\Omega+1)(\Omega+1)/(\Omega+2\Omega-1) \times$$

$$[ \begin{array}{ccccccccc} J' & \Omega & J & 2 & & J' & \Omega & J & 2 \\ -1/2 & 1 & -1/2 & \delta_{\Omega, 1/2} & + & -1/2 & -1 & 3/2 & \delta_{\Omega, 3/2} \end{array} ] \quad (5)$$

The 3-j symbols in the bracket of Eq. (5) determine the magnitude of the coupling between the initial and final rotational states. Allowed values of  $\lambda$  are determined by the phase factor term in Eq. (5) and the triangle rule for the magnitudes of  $J$ ,  $J'$  and  $\lambda$ . Alexander and Corey<sup>2</sup> get propensity rules only in the high- $J$  limit, but predictions of relative line intensity strengths for transitions between low-lying rotational states may also be obtained by evaluating the  $k_\lambda(J, J')$  coefficients for specific rotational e/f labels and spin states. For transitions between electronic states of opposite inversion symmetry, only odd  $\lambda$  values contribute to the series in Eq. (1). Taking only the  $\lambda=1$  term recovers the dipole selection rules, while inclusion of the  $\lambda=3, 5, \dots$  terms adds necessary corrections. From Eq. (4), the cross-sections can be determined only in terms of the  $\lambda$  dependent "base" cross-sections,  $\sigma(J=\lambda+1/2, \epsilon, 2_\Pi + J'=1/2, \epsilon, 2_\Sigma)$ . Thus, a priori cross-sections cannot be obtained from this formulation but relative values can be determined only if reasonable estimates of the base cross sections can be extracted from the experimental data.

In Fig. 1, the probe laser's scan reflects the propensities for collision induced transfer from the  $J=6.5$  ( $f, s, -$ ) level of the  $A^2_{\Pi_u} 3/2(v=4)$  state to the various nearly degenerate spin components of the  $X^2_{\Sigma_g} + (v=7)$  rotational manifold. Although the spin components are clearly resolved, the separations are due to perturbations in the  $B^2_{\Sigma_u} + (v=5)$  rotational levels so that the relative intensities of a pair of spin components in this figure represent relative populations of levels separated by  $\sim 0.04 \text{ cm}^{-1}$  in the  $X^2_{\Sigma_g} + (v=7)$  state. Because of the propensity for  $\Delta J=0$  and our inability to determine the contributions of the base cross sections with  $\lambda=5$  or greater, we compare calculated cross-sections from Eqs. (4) and (5) having

only  $\lambda=1$  and 3, with the experimental data. In order to get the relative calculated cross sections, the ratio of the  $\sigma(\lambda=1)$  to  $\sigma(\lambda=3)$  base cross sections must be known. We chose this ratio to be two in order to get the most reasonable agreement to the data. The calculated cross sections predict that the  $\Delta J=0$ ,  $R_1(6.5)$  line should be strongest with nearly twice (1.8) the intensity as the next most intense line which is the  $\Delta J=-1$ ,  $R_2(5.5)$  transition. Fig. 4(a) which compares the calculated and observed intensities of Fig. 1 shows the experimental  $R_1(6.5)$  line is slightly stronger than the other lines but not nearly as strong as predicted. Most of the other observed lines are in reasonable agreement with the calculated intensities.

It should be noted that in Figs. 2 and 3, the levels initially populated in the  $A^2_{\Pi_u} 3/2$  and  $A^2_{\Pi_u} 1/2$  manifolds, respectively, have the same rotational angular momentum, permutation symmetry and parity, i.e.,  $J=7.5(e,s,-)$ . The intensity patterns for these two figures are, however, quite different. If we make the same assumptions for the base cross-sections as in the previous paragraph, the most intense peak in Fig. 2 is predicted by Eqs. (4) and (5) to be the  $\Delta J=0$ ,  $R_2(7.5)$  peak which is expected to be almost twice (1.8) as large as the  $R_1(6.5)$ ,  $\Delta J=-1$  peak. In Fig. 4(b) the experimental intensities of Fig. 2 are compared with their calculated values. As in Fig. 4(a), the experimental  $R_2(7.5)$  peak in Fig. 4(b) does not agree with its predicted intensity. The other peaks, however, are within 15% of the predicted relative cross sections which is excellent agreement. Fig. 4(c) gives the comparison of calculated and observed intensities of Fig. 3. The strongest predicted line is the  $\Delta J=0$ ,  $R_2(7.5)$  transition with nearly twice the intensity as

the  $\Delta J=+1$ ,  $R_1(8.5)$  line which should have the next largest predicted cross section. The figure shows that  $R_2(7.5)$  is indeed the strongest line, but the next most intense line is not  $R_1(8.5)$ . For this particular case where a strong line occurs as predicted, the weaker lines are not in as good agreement as the above cases.

In general, probe laser scans of collision induced transitions from rotational levels having the same e or f label in a particular spin component of the  $A^2_{11/2}$  state have similar intensity patterns. Thus, the comparisons given above are representative of the degree of agreement between our experimental results and the relative cross sections based on the work of Alexander and Corey<sup>2</sup>. Considering the assumptions that had to be made concerning the base cross sections in order to calculate the relative cross sections from Eqs. (4) and (5), we find our results to be in general qualitative agreement with the predicted intensities. There is still need, however, for more theoretical as well as experimental work before these collision induced electronic transition processes can be understood. It is still not clear how these electronic transfers can occur over a large energy gap ( $\sim 1760 \text{ cm}^{-1}$ ) with the efficiency necessary to reveal propensity rules.

At present, work on determining the form of the interaction potential is continuing.

## V. Recommendations

Obviously, the work started in this research has yet to be completed. As has been seen in the previous sections, the differences between theory and experiment are still great. A simple quantum mechanical formulation such as that of Alexander and Corey, though intuitive and complete, still lacks the ability to quantitatively predict the relative cross sections for the transitions observed in our experiment.

The inclusion of the interaction potential into these calculations seems to be essential. Further work by others has shown that pursuing the close coupling formulation without specifying the potential leads to no better results than that obtained in considering only the first order approximation of the theory.

Thus far, we have not been able to arrive at theoretical results which will support our experimental findings, but research continues in this area. Other improvements in the theory are possible that may alter the existing predictions. One example would be to examine a more involved trajectory of the scattering partner in the course of one of these collisions. Up until the present, a straight-line approximation has been used to make the calculations time-dependent and thereby include the effects of the energy gap; however such an assumption is by no means realistic.

ACKNOWLEDGEMENTS

I would like to gratefully acknowledge the guidance of Dr. Daniel H. Katayama, the LIU Division of AFGL for its support and the sponsorship of the Air Force Geophysics Laboratory, United States Air Force.

## References

1. For example, Herzberg, Gerhard, Spectra of Diatomic Molecules, Van Nostrand Publishers, (1950).
2. Alexander, M.H. and Corey, G.C., *J. Chem. Phys.* 84, 100 (1986).
3. Alexander, M.H., *J. Chem. Phys.* 76, 3637 (1982).
4. Alexander, M.H., *J. Chem. Phys.* 76, 5974 (1982).
5. Alexander, M.H. and Pouilly, B., *J. Chem. Phys.* 79, 1545 (1983).
6. Katayama, D.H. and Dentamaro, A.V., *J. Chem. Phys.* 85, 2595 (1986).
7. Katayama, D.H., *J. Chem. Phys.* 81, 3495 (1984).
8. Katayama, D.H., *Phys. Rev. Lett.* 54, 657 (1985)
9. Klynning, L. and Pages, P., *Phys. Scr.* 25, 543 (1982).
10. Gottscho, R.A., Field, R.W., Dick, K.A., and Benesch, W., *J. Mol. Spectrosc.* 74, 435 (1979).
11. Alexander, M.H., Davis, S.L., and Dagdigian, P.J., *J. Chem. Phys.* 83, 556 (1985).
12. Edmonds, A.R., Angular Momentum in Quantum Mechanics, Princeton University Press, Princeton, New Jersey, 1957.
13. Lofthus, A. and Krupenie, P.H., *J. Phys. Chem. Ref. Data* 6, 113 (1977).
14. Greene, C.H. and Zare, R.N., *J. Chem. Phys.* 78, 6741 (1983).
15. Brown, J.M., Hougen, J.T., Huber, K.P., Johns, J.W.C., Kopp, I., Lefebvre-Brion, H., Merer, A.J., Ramsay, D.A., Rostas, J. and Zare, R.N., *J. Mol. Spectrosc.* 55, 500 (1975).

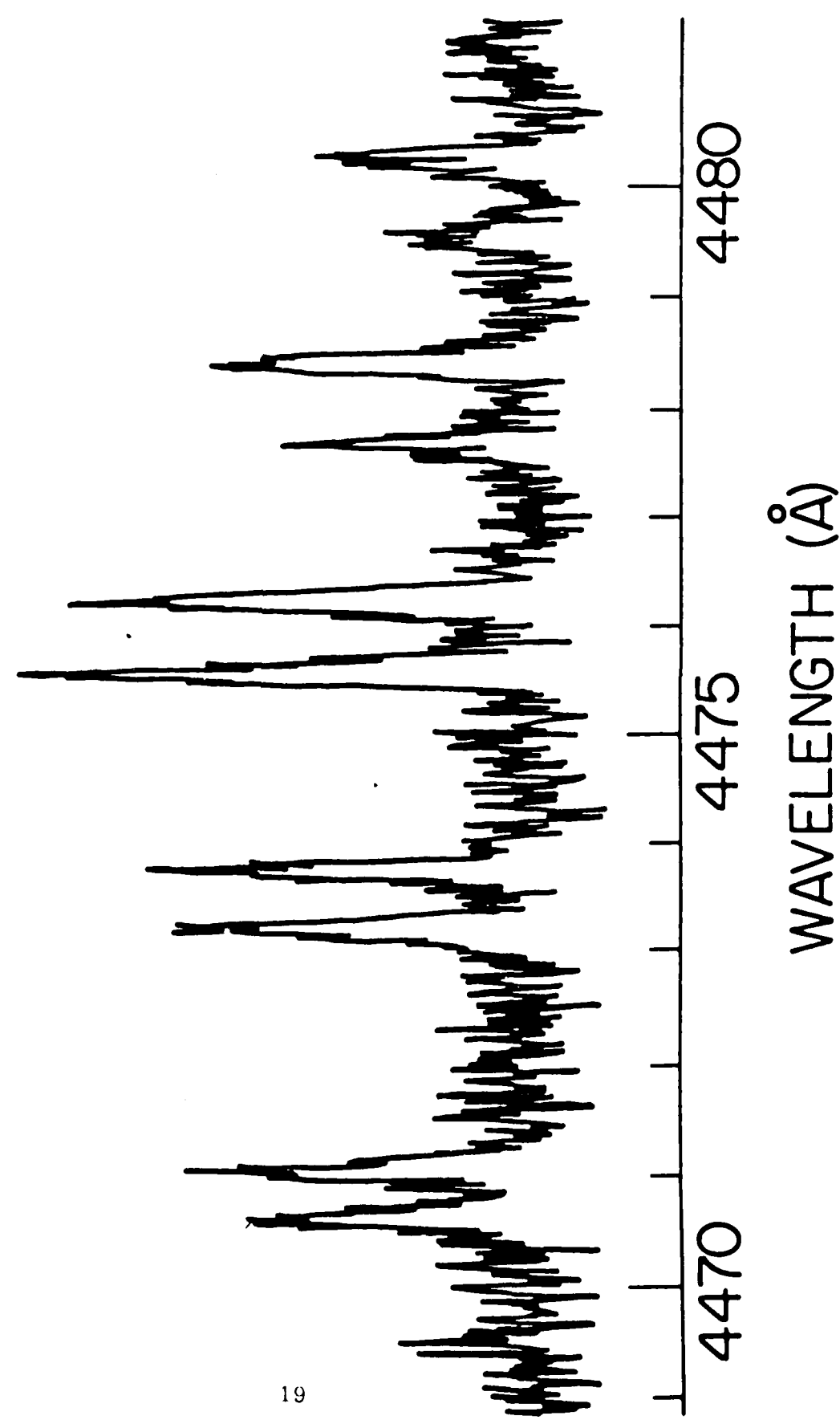
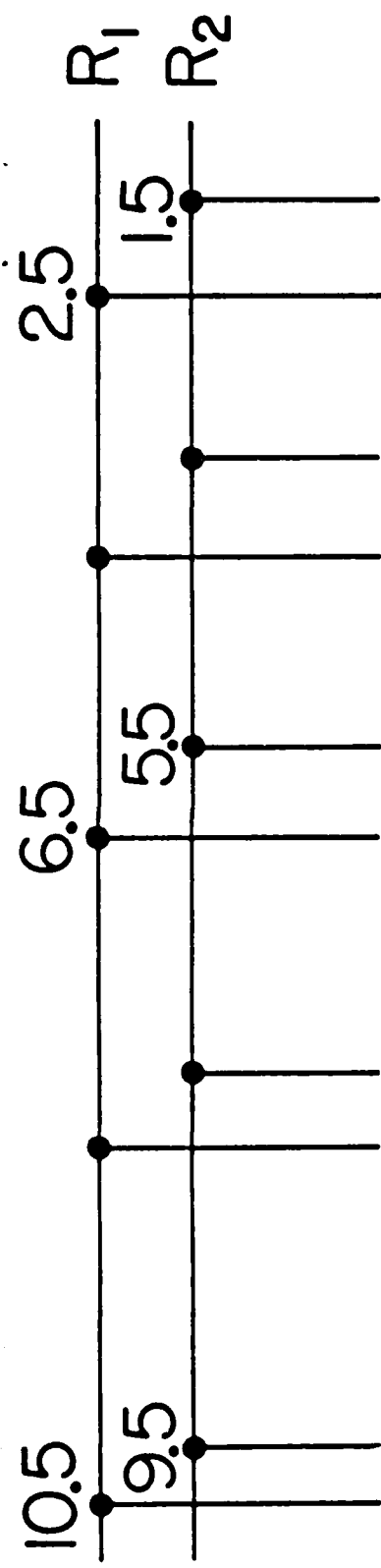
### Figure Captions

Fig. 1 OODR spectrum of the  $B^2\Sigma_u^+ - X^2\Sigma_g^+$  (5,7) band of  $N_2^+$ . The numbers of the  $R_1$  and  $R_2$  branches refer to the  $J''$  levels of this band. The probe laser scans this band with the pump laser tuned to the  $Q_1(N''=6, J''=6.5)$  line of the A-X (4,0) band so that the  $A^2\Pi_{u3/2}(v=4, J=6.5, f, s, -)$  level is selectively populated.

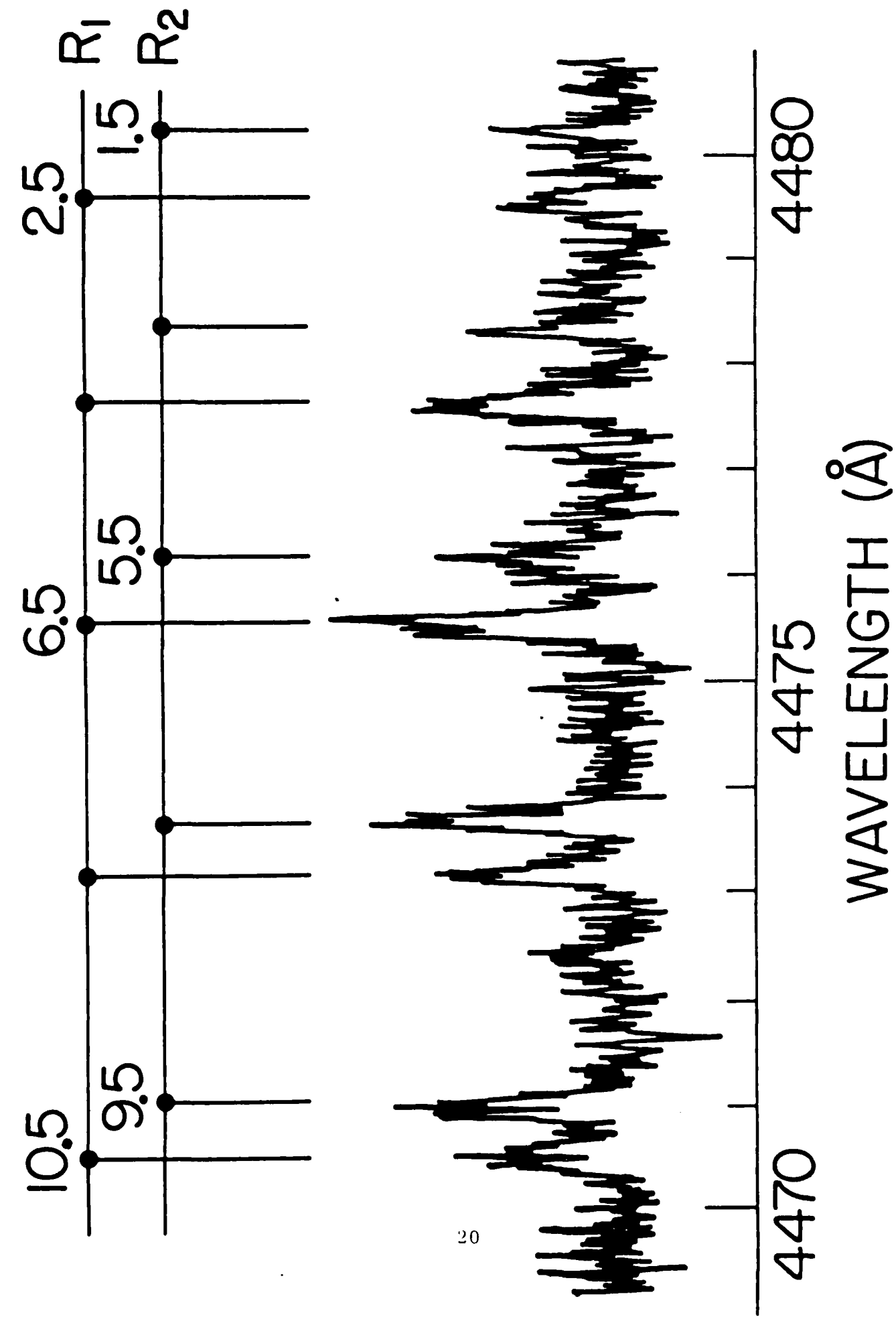
Fig. 2 OODR spectrum of the B-X (5,7) band with the pump laser tuned to the  $P_1(N''=8, J''=8.5)$  line of the A-X (4,0) band. The  $A^2\Pi_{u3/2}(v=4, J=7.5, e, s, -)$  level is initially populated for this scan.

Fig. 3. OODR spectrum of the B-X (5,7) band with the  $A^2\Pi_{u1/2}(v=4, J=7.5, e, s, -)$  level being selectively populated by the pump laser tuned to the  $Q_2(N''=8, J''=7.5)$  line of the A-X (4,0) band.

Fig. 4. Comparison of theoretical to experimental intensities obtained with the pump laser tuned to (a)  $Q_1(6)$ , (b)  $P_1(8)$ , and (c)  $Q_2(8)$  lines of the  $A^2\Pi_u - X^2\Sigma_g^+$  (4,0) band. The corresponding probe laser scans which show these experimental intensities are in Figs. 1, 2, and 3, respectively. For each  $R(N'')$  spin doublet,  $R_1(J''=N''+1/2)$  lies to the left of the  $R_2(J''=N''-1/2)$  component.



(FIGURE 1)



(FIGURE 2)

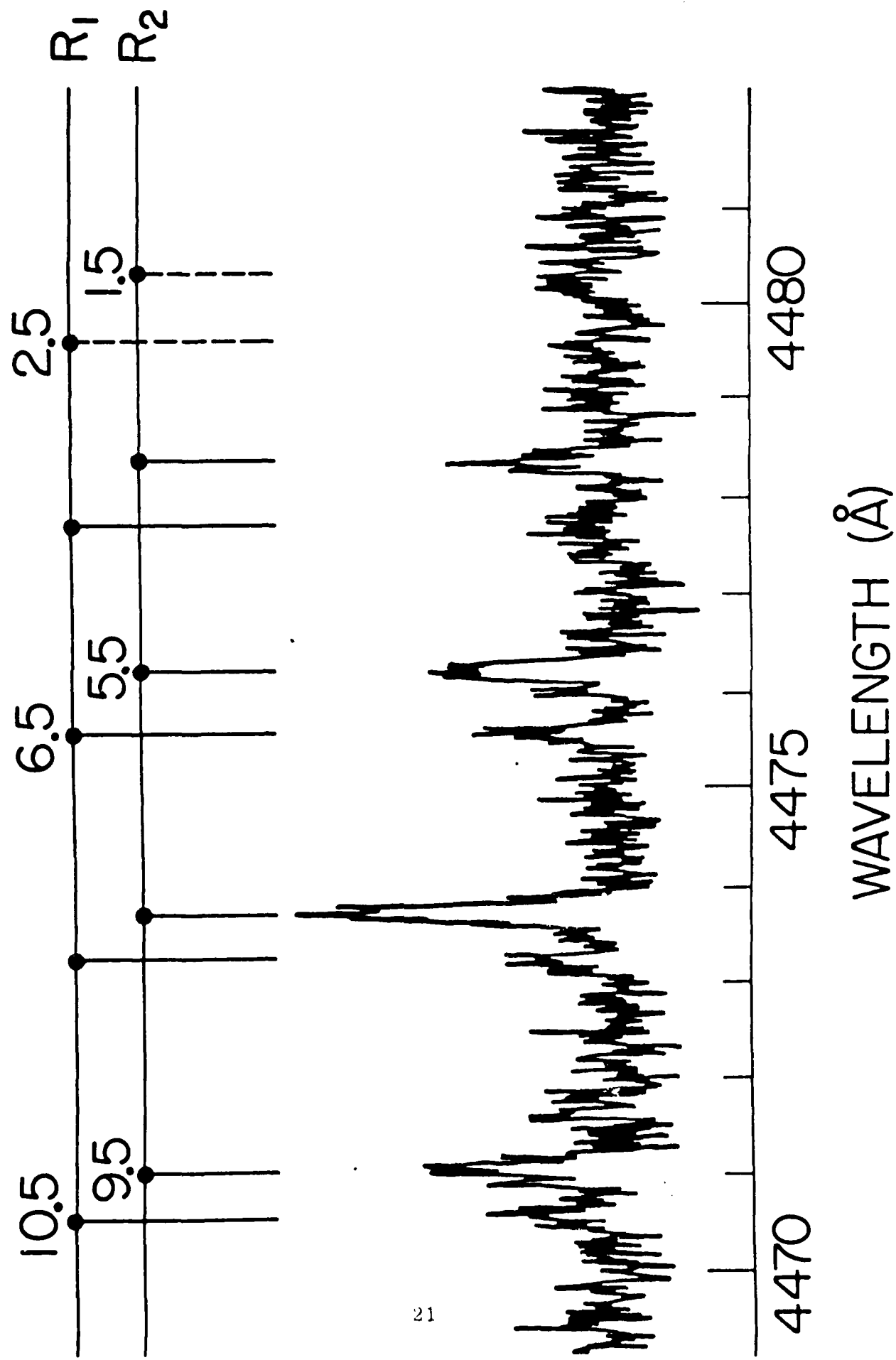
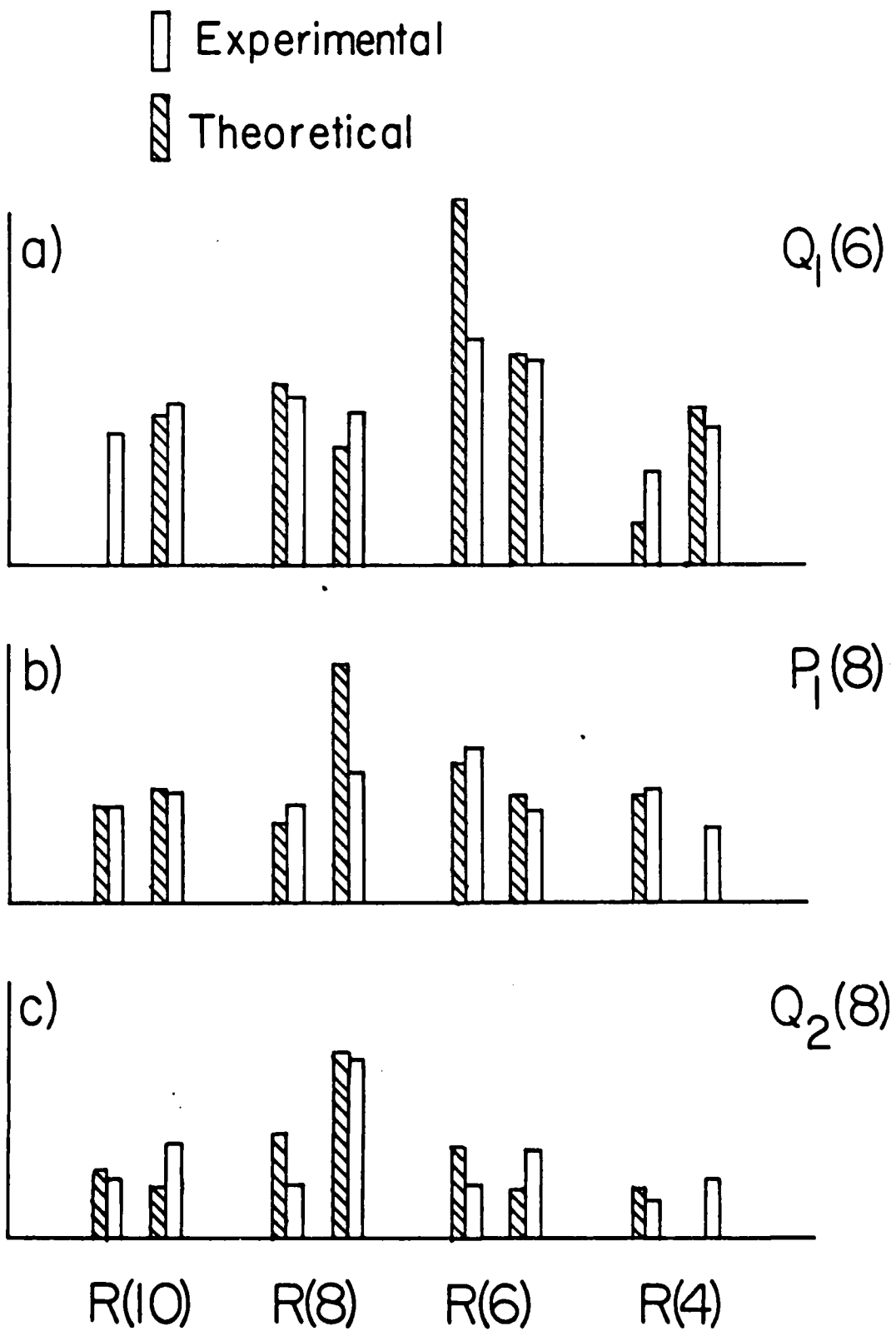


(FIGURE 3)

(FIGURE 4)



1985-1986 AFGL-SCEEE GEOPHYSICS SCHOLAR PROGRAM

Sponsored by the

AIR FORCE GEOPHYSICS LABORATORY

Conducted by the

SOUTHEASTERN CENTER FOR ELECTRICAL ENGINEERING EDUCATION

FINAL REPORT (Addendum)

Prepared by: Anthony V. Dentamaro

Research Location: Air Force Geophysics Laboratory  
LIU Division

AFGL Research Contact: Daniel H. Katayama

Date: 29 August 1986

In the one month period following the completion of my first year of research, the advances have been completely in the theoretical modelling of our collision-induced electronic transition experiment. As was previously reported, Dr. Daniel H. Katayama and I have completed an optical-optical double resonance experiment in which we were able to observe transitions between specific rovibrational manifolds in the electronic transition  $A^2\Pi_u - X^2\Sigma_g^+$  in collisions of  $N_2^+$  with atomic helium. No previously suggested model has been able to reproduce our data, and so we have begun trying to model the interaction ourselves.

Assuming a Morse-type interaction potential similar to that currently used in describing vibrational predissociation of diatomic molecules, we have developed an electronic analogue to compare to our experimental findings. With this particular model, we will be able to study the sensitivity of our proposed interaction to collision angle, relative orbital angular momentum before and after collision and energy gap traversed in transition.

1985-1986 AFGL-SCEEE GEOPHYSICAL SCHOLAR PROGRAM

Sponsored by the

AIR FORCE GEOPHYSICS LABORATORY

Conducted by the

SOUTHEASTERN CENTER FOR ELECTRICAL ENGINEERING EDUCATION

FINAL REPORT

NEUTRAL REACTIONS IN THE PRESENCE OF ALKALI IONS

Prepared by: Carol A. Deakyne

Research Location: Air Force Geophysics Laboratory  
Ionospheric Interactions Division

AFGL Research Contact: John F. Paulson

Date: September 18, 1986

Contract Number:

Acknowledgments

I would like to thank the Air Force Systems Command, the Air Force Office of Scientific Research and the Air Force Geophysics Laboratory for support during this year. I also want to thank Drs. John F. Paulson, A. A. Viggiano, and Michael J. Henchman for many helpful discussions.

# Neutral Reactions in the Presence of Alkali Ions

A.A. Viggiano<sup>1</sup>, Carol A. Deakyne<sup>2</sup>, F. Dale, and John F. Paulson  
AFGL/LID Hanscom AFB MA 01731-5000

## ABSTRACT

It has been shown that neutral ligands clustered to alkali ions can react with other neutrals. In fact, the presence of the alkali ion greatly enhances the rate of the corresponding neutral - neutral reaction. Several more reactions that exhibit this phenomenon have been identified experimentally, with rate enhancements ranging from 4 to 30 orders of magnitude. Three possible explanations for the rate enhancement have been explored. Ab initio calculations have been carried out to supplement the experimental measurements and to provide further insight into the mechanism. The calculations indicate that bonding the neutral to the alkali ion causes structural rearrangements that shift the geometry of the neutral molecule toward its transition state geometry, thereby lowering the activation energy of the reaction.

1. Under contract to AFGL from Systems Integration Engineering Inc., Lexington MA 02173.
2. Air Force Geophysics Scholar

## Introduction

Alkali ions are isoelectronic with the noble gases and therefore are unreactive species. However, they form cluster bonds to a wide variety of neutrals. These cluster bonds have been shown to be mainly electrostatic in nature.<sup>1</sup> Rowe, et al.<sup>2</sup> found that the ligands clustered to the alkali ions can react with other neutrals, and, in fact, the presence of the alkali ion greatly enhances the rate of the corresponding neutral - neutral reaction. For example, the rate constant for reaction (1) is 9 orders of magnitude larger in the presence of a  $\text{Li}^+$  ion than the corresponding neutral reaction.<sup>2</sup>



The rate enhancement for this reaction was found to depend strongly on the alkali to which the  $\text{N}_2\text{O}_5$  was clustered. The rate constant for reaction (2) was also significantly enhanced in the presence of alkali ions.



Rowe, et al.<sup>2</sup> postulated three reasons for these large rate enhancements. The first is that the electrostatic interaction energy of the alkali ion - neutral complex and reactant neutral is larger than the activation energy for the reaction between the neutral reactants in the absence of the ion. The second is that the potential energy surface is sufficiently altered in the presence of the ion to greatly increase the rate constant. Finally, the lifetime of the collision complex in the presence of the alkali ion is longer, yielding a greater reaction probability.

We have undertaken a study to determine the relative importance of the above causes of the rate enhancement. We have found several more reactions that exhibit this phenomena, with rate enhancements of as much as 30 orders of magnitude. In addition, ab initio calculations have been carried out in order to supplement the rate constant measurements and to provide further insight into the mechanism.

## Experimental and Theoretical Details

**A. Experimental Method.** The experimental measurements were made in a newly constructed combination flowing afterglow (FA) - selected ion flow tube (SIFT) apparatus. The apparatus is shown in Figure 1. The SIFT part of the instrument is similar to the previous instrument used in our laboratory. The FA was designed to operate at high pressures using a design similar to that of Fahey et al.<sup>3</sup> In the SIFT, ions are created in a high pressure (~1 torr) ion source. Upon exiting the ion source,

the ions are focused into a quadrupole mass filter and are injected through a venturi inlet into a flow tube 1 meter long. Introducing the ions through the venturi inlet aids the movement of ions from the low pressure quadrupole region to the high pressure flow tube. The ions are carried down the length of the flow tube by the buffer gas. The neutral reactant is added downstream. Reactant and product ions are sampled through a 0.2 mm hole in a blunt nose cone and detected by a second quadrupole and channel electron multiplier.

The FA differs only in that the ions are created directly in the carrier gas. For these studies the ion source region was separated from the flow tube by a diaphragm 5 mm in diameter. Under these conditions the ion source region was maintained at a pressure of 10-20 torr and the flow tube was operated at approximately 0.5 torr.

The alkali ions were produced by thermionic emission from a rhenium filament coated with the appropriate alkali nitrate, silicon dioxide and aluminum oxide. After a few hours of conditioning, heating the filament produced an essentially pure signal of the alkali of interest. The filament was electrically biased by a few volts with respect to the flow tube walls in order to help the ions enter the flow. Three filaments were put in the tube to enable us to change alkali ions rapidly. The cluster ions were made by adding the clustering neutral to the ion source region slightly downstream of the filament. For the most part, clustering occurred in the ion source region due to the high pressure there. In this way, we were frequently able to add much less of the clustering gas than would have been needed to obtain the same amount of clustering in the absence of the diaphragm. In order to obtain the best signal for the cluster ion of interest without interference from other ions (i.e. larger cluster ions), the temperature, pressure, and buffer gas were varied. Three buffers were used, He, N<sub>2</sub>, and Ar.

The gases used in the experiments were standard commercial gases. The CO and NO were purified by passing them through an ascarite filter. Atomic oxygen was produced by passing a mixture of He and O<sub>2</sub> through a microwave discharge. The amount of O formed was monitored by the reaction of CH<sub>5</sub><sup>+</sup> (generated in the SIFT) with O.<sup>4</sup> Typically the percent dissociation was in the 30-40% range. This method is not as accurate as measuring the O atom concentration directly but is sufficient for the present purposes. Rate constants are believed to be accurate to within a factor of two.

B. Theoretical Method. The calculations were carried out ab initio on a VAX 11/780 computer. The Gaussian 82 series of programs were utilized to perform the calculations.<sup>5</sup> The optimum structures of CO<sub>2</sub>, NO<sub>2</sub>, NO, Li<sup>+</sup>(CO<sub>2</sub>), Li<sup>+</sup>(NO<sub>2</sub>), Li<sup>+</sup>(NO), and LiO<sup>+</sup> were obtained at the HF/6-31G\* basis set level<sup>6</sup> via the force relaxation method.<sup>7</sup> All the additional calculations were carried out at the optimized 6-31G\* geometries. Electronic lithium ion affinities  $\Delta E$ 's were computed with the 6-31G\* and 6-31+G\* basis sets.<sup>8</sup> The effect of electron correlation on the  $\Delta E$  values was

determined by means of Møller - Plesset perturbation theory to third (MP3) order.<sup>9</sup>

From her investigation of the lithium ion affinities of several oxygen and nitrogen bases, Del Bene<sup>10</sup> has shown that relative affinities at these levels of calculation are quite good. However, the  $\Delta E$  values tend to be overestimated (particularly the 6-31G\*  $\Delta E$ 's) compared to the values obtained at higher levels of theory.

The electronic lithium ion affinities were calculated using equation (3). Here  $E_T$  is the total electronic energy and A is O, NO, CO, NO<sub>2</sub>, or CO<sub>2</sub>. In order to compare the  $\Delta E$ 's to experimental gas - phase lithium ion affinities, zero - point vibrational energy changes and temperature effects<sup>11</sup> have been estimated based on Del Bene's<sup>10</sup> results.

$$(3) \quad \Delta E = - [E_T (LiA^+) - E_T (Li^+) - E_T (A)]$$

### Results and Discussion

A. Trends in the Experimental Rate Enhancements. The results of this study as well as those of Rowe et al.<sup>2</sup> are listed in Table I. In addition to the reactions given in the table Rowe et al.<sup>2</sup> studied two other reactions that showed no rate enhancement. None of the rate constants were found to vary significantly with temperature. The column in Table I headed rate enhancement refers to the ratio of the rate constant in the presence of the alkali ion to that of the corresponding neutral reaction at the coldest temperature studied. Since none of the rate constants reported in Table I have been found to vary with temperature and all of the neutral rate constants have positive activation energies, this definition represents the largest value of the rate enhancement for each reaction. The rate enhancement varies from 4 orders of magnitude to 30 orders of magnitude.

As a result of several different experimental difficulties we were unable to measure any of these reactions on K<sup>+</sup>. In general, bond strengths of neutrals to alkali ions decrease as the molecular weight of the alkali ion increases, due to the increasing size of the alkali.<sup>12</sup> Therefore, one must decrease the temperature of the flow tube in order to get workable signals of the K<sup>+</sup> clusters. In the case of K<sup>+</sup>(NO<sub>2</sub>) the NO<sub>2</sub> froze in the inlet line before we could obtain usable signals of K<sup>+</sup>(NO<sub>2</sub>).

We could not do any experiments that involved K<sup>+</sup> and O due to the following unusual problem. Some unknown neutral KX emitted from the K filament reacted with O to form ion pairs.



We could detect the formation of both  $K^+$  and  $X(O)^-$ . Negative ion masses were observed at  $79 \pm 0$  and  $246 \pm 2$  amu in the ratio of 1 to 10. We have not been able to identify these ions although the ion at mass 79 has no major isotopes. Reaction (4) has a rate constant of  $2 \times 10^{-10} \text{ cm}^3 \text{ s}^{-1}$  and unfortunately produces much more  $K^+$  than is emitted directly from the filament. We had also hoped to study several reactions involving  $F_2$  but neutrals emitted from all three alkali filaments created ion pairs upon addition of  $F_2$ . These chemionization reactions, although not understood, represent the majority of the ground state chemionization reactions known.<sup>13</sup> Moreover, they are the only chemionization reactions that form negative ions directly rather than forming electrons.<sup>13</sup>

Several trends in the data are readily observable. Neutrals clustered to  $Li^+$  react either at the same rate or faster than those clustered to  $Na^+$ , which in turn react faster than those clustered to  $K^+$  (Table I). The most dramatic example is the case of  $N_2O_5$  reacting with NO, where the reaction in the presence of  $Li^+$  is about two orders of magnitude faster than it is in the presence of  $Na^+$ . No detectable reaction was observed in the presence of  $K^+$ . The rate constant observed for the reaction of  $NO_2$  with CO in the presence of  $Li^+$  is a factor of seven slower than it is in the presence of  $Na^+$ . For the  $O_3$  reaction with NO the rates in the presence of  $Li^+$  and  $Na^+$  are the same, while the  $K^+$  reaction is over an order of magnitude slower. All the reactions involving O atoms are fast (within a factor of 5 of the collision rate) with the exception of the reaction of  $N_2O$  with O.

In some cases the two neutral products both separate from the alkali as, for example, in the  $O_3$  reaction with NO. This reaction is highly exothermic which provides sufficient energy to dissociate both neutrals and, indeed, both do dissociate. The reaction of  $NO_2$  with CO is also sufficiently exothermic to dissociate both ligands; however, in this case the  $CO_2$  ligand stays attached to the alkali ion. In the reaction of  $N_2O_5$  with NO the reaction is exothermic only if one of the products remains attached to the alkali ion, and this is what is observed.

For several of the reactions it was also possible to determine what occurs when a second ligand is bonded to the alkali ion - neutral complex (Table I). The rate constant was found to be approximately the same whether one or two ligands were bonded to the alkali ion, although the product of the two reactions sometimes varied. For example, when  $H_2S$  reacts with O the main products are  $Li^+(HSO)$  [or  $Na^+(HSO)$ ] + H when one ligand is attached and  $Li^+(H_2SO)$  [or  $Na^+(H_2SO)$ ] +  $H_2S$  when two ligands are attached. The reaction involving two ligands may be thought of as an addition reaction in which the third body (the second  $H_2S$ ) is built into the reactants.

**B. Trends in the Calculated Electronic Lithium Ion Affinities.** Table II tabulates the total energies of  $Li^+$ , O, NO,  $NO_2$ ,  $CO_2$ ,  $LiO^+$ ,  $Li^+(NO)$ ,  $Li^+(NO_2)$ , and  $Li^+(CO_2)$  at

the various basis set levels. Table III gives the lithium ion affinities of O, NO, CO,<sup>10</sup> NO<sub>2</sub>, and CO<sub>2</sub>. LiO<sup>+</sup> is essentially not bound at any level of theory. The relative affinities of the other species are CO<sub>2</sub> > NO<sub>2</sub> > CO > NO.

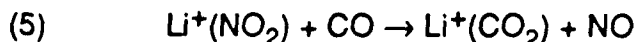
The addition of diffuse functions to the basis set (6-31+G\* vs. 6-31G, Table III) decreases  $\Delta E$  by about 1 - 1.5 kcal mol<sup>-1</sup>. Taking electron correlation effects into account at the MP2 level also decreases  $\Delta E$  by about 2 - 3.5 kcal mol<sup>-1</sup>. In contrast, the third order Møller-Plesset calculation increases the lithium ion affinity to a value in between the Hartree - Fock (HF) and MP2 values. These patterns are identical to those observed by Del Bene.<sup>10</sup>

The MP3/6-31+G\* electronic affinities obtained by Del Bene<sup>10</sup> are 1 - 1.5 kcal mol<sup>-1</sup> larger than those obtained with the highest level of theory she considered, i.e., the MP4SDQ/6-311+G(2d,2p) level. In addition, correcting for zero - point energy changes and temperature effects (i.e., converting a  $\Delta E$  to a  $\Delta H$ )<sup>11</sup> lowers Del Bene's calculated  $\Delta E$ 's by 0.5 - 1.5 kcal mol<sup>-1</sup>. If the lithium ion affinities of the molecules studied in this work follow the same trends as those observed by Del Bene,<sup>10</sup> then increasing the size of the basis set, taking the Møller - Plesset calculations to higher order, and correcting for zero - point energy changes and temperature effects will decrease the values reported in Table II by 1 - 3 kcal mol<sup>-1</sup>. Corrected lithium ion affinities computed with the MP4SDQ/6-311+G(2d,2p) basis set are generally about 2 kcal mol<sup>-1</sup> smaller than the experimental gas - phase values.<sup>14</sup>

Although changing the basis set does change the magnitudes of the  $\Delta E$ 's, the trends in the  $\Delta E$ 's vary very little with respect to basis set (Table III). The order of the electronic lithium ion affinities is the same at each basis set level, and the  $\delta\Delta E$ 's are quite similar at each basis set level.

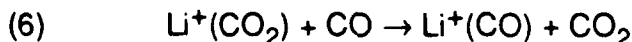
C. Reaction Products vs. Buffer. One interesting observation not included in Table I is that the products of the NO<sub>2</sub> reaction with CO in the presence of Li<sup>+</sup> vary depending on which buffer is used. In a He buffer the major product ion is Li<sup>+</sup>(CO); the minor product ion is Li<sup>+</sup>(CO<sub>2</sub>). In a N<sub>2</sub> buffer only the Li<sup>+</sup>(CO<sub>2</sub>) product is obtained. About equal amounts of the two products are formed in an Ar buffer.

The following explanation is consistent with the above observations, although we have no firm evidence that excludes other explanations. Reaction (5)



is highly exothermic;  $\Delta H$  is estimated to be -73 kcal mol<sup>-1</sup> from the HF/6-31G\* data in Table II [ $E_T(\text{CO}) = -112.73691$  kcal mol<sup>-1</sup><sup>15</sup>]. This suggests that the initial products contain a considerable amount of internal energy. Helium is not a very good quencher of vibrational energy in ions; therefore, one would expect the Li<sup>+</sup>(CO<sub>2</sub>) product to

remain vibrationally excited.<sup>16</sup> In contrast, one would expect that any vibrational excitation would be quenched in a N<sub>2</sub> buffer and that an Ar buffer would quench some but not all of the excitation.<sup>16</sup> The switching reaction



is endothermic.  $\Delta H$  is estimated to be 3 - 5 kcal mol<sup>-1</sup> based on the data in Table III and the analysis given above for converting  $\Delta E$  to  $\Delta H$ . However, if the reactant ion has vibrational energy in excess of the endothermicity, the reaction may proceed. In light of the above discussion on quenching rates in different buffers, one would expect the amount of Li<sup>+</sup>(CO) formed to vary in the manner observed.

D. Reasons for the Rate Enhancement. One would like to obtain some understanding of the reasons for the rate enhancement. Only a detailed theoretical study can answer this interesting problem but some simple qualitative arguments may shed some light on it. Three explanations have been postulated for why the reaction rate constants are significantly faster in the presence of the alkali ions.<sup>2</sup> The first is that the interaction energy between the cluster ion and neutral is significantly larger than that for two neutrals. Secondly, the molecular potential energy surface is significantly altered by the presence of the ion. Finally, the lifetime of an ion - neutral collision complex is significantly longer than that for a neutral - neutral encounter. In reality these are not separable quantities but it is of interest to look at the information we have on each one individually.

The interaction energies between the ionic and neutral reactants are not known. Two simple methods are available to estimate the order of these energies. The first method is to take the interaction energy between a positive charge and a polarizable dipole at the radius of the alkali ion. Assuming purely electrostatic interactions this would overestimate the interaction energy, since the clustered alkali has a larger distance of closest approach than the unclustered alkali. The other method is to use information on the bond strengths of other ligand - alkali ion complexes to obtain some estimate of the bond strengths of the species in question. The first method<sup>17</sup> gives interaction energies of 45 - 129 kcal mol<sup>-1</sup> for Li<sup>+</sup>, 7 - 26 kcal mol<sup>-1</sup> for Na<sup>+</sup> and 2 - 9 kcal mol<sup>-1</sup> for K<sup>+</sup> with the neutrals used in this study. The lower number refers to O atoms and the higher to CO. Not much information is available on bond strengths of neutrals to alkali ions. Typical bond strengths of Li<sup>+</sup> to polar neutrals are on the order of 35 kcal mol<sup>-1</sup>.<sup>12</sup> Na<sup>+</sup> clusters have bond strengths between 12 (CO) and 24 (H<sub>2</sub>O) kcal mol<sup>-1</sup>.<sup>12</sup> K<sup>+</sup> bond strengths range from 8.5 (CO<sub>2</sub>) to 17 (H<sub>2</sub>O) kcal mol<sup>-1</sup>.<sup>12</sup>

A first estimate of whether the neutral reaction can take place in the presence of the alkali ions is whether the above electrostatic interaction energies are larger than

the neutral activation energies  $E_a$ . In fact, this was the method used to determine which reactions might be catalyzed by the presence of the alkali ions. Previously, no such method was employed and most of the reactions tried were not catalyzed.

The activation energy<sup>18</sup> for the reaction between  $N_2O_5$  and NO is 22 kcal mol<sup>-1</sup>. The estimated  $Alk^+(N_2O_5)$  - NO interaction energies are  $\geq 35$  kcal mol<sup>-1</sup> for  $Li^+$ , 15-25 kcal mol<sup>-1</sup> for  $Na^+$  and  $\leq 10$  kcal mol<sup>-1</sup> for  $K^+$ . These estimates are in line with the observed trends.  $Li^+$  enhances the rate the most, and the  $Li^+$  interaction energy is much larger than the activation energy. The rate constant in the presence of  $Na^+$  is two orders of magnitude lower than it is in the presence of  $Li^+$ , and the interaction energy and activation energy are comparable for  $Na^+$ . The rate is not affected in any measurable manner when  $K^+(N_2O_5)$  rather than  $N_2O_5$  reacts with NO. In this case the interaction energy is significantly lower than the activation energy.

The rate constants for the reactions of  $Na^+(O_3)$  and  $Li^+(O_3)$  with NO are similar in magnitude (Table I), while that for the reaction of  $K^+(O_3)$  with NO is an order of magnitude smaller. The activation energy<sup>19</sup> for the neutral reaction between  $O_3$  and NO is 2.9 kcal mol<sup>-1</sup>. The electrostatic interaction energies are significantly larger than  $E_a$  for  $Li^+$  and  $Na^+$ . In contrast,  $E_a$  and the  $K^+(O_3)$  - NO interaction energy are similar (see analysis above). For the O reactions (except for  $N_2O + O$ ), all of which are fast, the interaction energies are significantly greater than the activation energies of 3 - 4 kcal mol<sup>-1</sup>.<sup>20</sup> The reaction of  $NO_2$  with CO has the largest activation energy of any reaction for which we observed a rate enhancement. Here  $E_a$  is less than the  $Alk^+(NO_2)$  interaction energy expected for  $Li^+$  but is slightly larger than that expected for  $Na^+$ . We also looked at the reaction of  $H_2O + CO$  which has an activation energy of 53 kcal mol<sup>-1</sup> and saw no reaction in the presence of  $Li^+$ . Rowe et al.<sup>2</sup> also studied several reactions with large activation energies and saw no reaction.

**E. Reactant Surfaces.** The above results may best be explained by a change in the reactant surface when the neutrals are bound to an alkali ion (Figure 2). The top drawing in Figure 2 is a schematic representation of the reaction coordinate for the purely neutral reaction. Reactants A and B proceed over an activation barrier of magnitude  $E_a$  yielding reactants C and D. The simplest model for the reaction in the presence of the alkali ion is the two basin potential proposed by Brauman and co-workers<sup>21</sup> to explain many ion-molecule reactions (bottom drawing, Figure 2). The reactants are neutral A clustered to an alkali ion  $Alk^+(A)$  and B. As the reaction proceeds along the reaction coordinate the reactants fall into an attractive well due to the electrostatic attraction between the cation cluster and neutral. After the first attractive well,  $Alk^+(A)(B)$  encounters a barrier whose height can be either above or below the initial energy of the reactants. A second well follows corresponding to the cluster  $Alk^+(C)(D)$ . Finally one or both of the neutral products dissociates from the

alkali ion.

Based on the above schematic the criterion for reaction is the height of the activation barrier between the two wells. If the barrier exceeds the initial energy of the reactants (case A) then the reaction will still have a positive activation energy and will not be measurable in our apparatus. The reaction may still be significantly faster in the presence of the ion but we cannot measure the difference in rates. If the barrier is considerably lower than the initial energy of the reactants (case B) the reaction rate should be rapid. As the barrier height changes from above to below the initial energy of the reactants (case C) the rate constant should become increasingly larger. In nucleophilic displacement reactions involving gas phase ions the effect of the barrier becomes negligible only when it is approximately 5-10 kcal mol<sup>-1</sup> below the zero of energy.<sup>21</sup>

How does the present data fit into this scheme? All the reactions in the presence of Li<sup>+</sup> would be represented by case B, i.e., the barrier has little or no effect since the well depth is substantial. The reactions in the presence of Na<sup>+</sup> for which the rate constant is comparable to that for the reaction in the presence of Li<sup>+</sup> are also type B reactions. Those for which the rate is substantially slower than the rate when a Li<sup>+</sup> complex is a reactant would be case C reactions. The barrier height has just begun to be important when the two rate constants vary by less than an order of magnitude. The reactions of N<sub>2</sub>O<sub>5</sub> and O<sub>3</sub> with NO in the presence of K<sup>+</sup> fall into categories A and B, respectively. As stated previously experimental difficulties prevented us from studying any of the new reactions in the presence of K<sup>+</sup>. This is unfortunate since it would have been a useful test of this scheme.

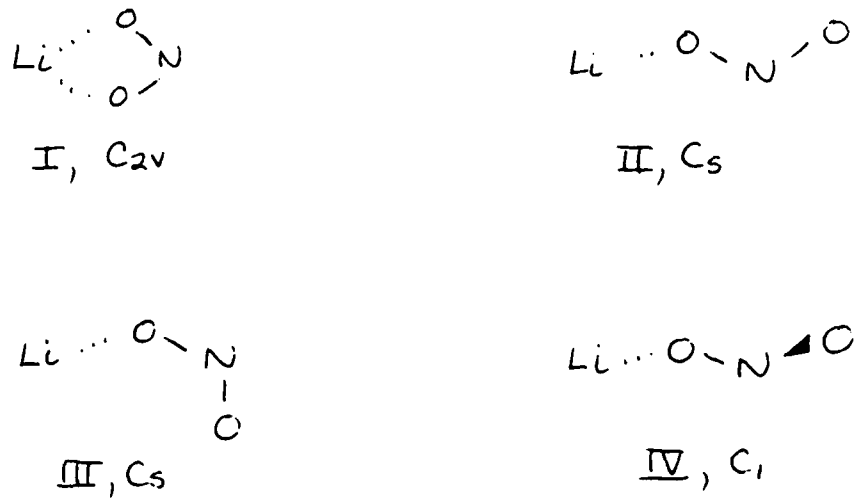
The temperature dependences of reactions in the three categories would be as follows. Case A reactions would have a positive temperature dependence, case B reactions would show no temperature dependence, and case C reactions would have a negative temperature dependence. The magnitude of the negative temperature dependence would be fairly small ranging between approximately T<sup>-1/2</sup> (small molecules only) and T<sup>0</sup>, where I is the total number of rotational degrees of freedom.<sup>22</sup> No temperature dependences were seen for any of the reactions, although a small temperature dependence would have been missed due to the larger than normal uncertainty in the data. This is in qualitative agreement with the above picture.

E<sub>a</sub> vs. E<sub>a'</sub>: Next we explore the interesting problem of the relative magnitudes of the barrier heights E<sub>a</sub> and E<sub>a'</sub>. The discussion above correlating the observed rate constant to the electrostatic interaction energy and the neutral activation energy suggests that E<sub>a</sub> and E<sub>a'</sub> are similar but not identical in magnitude.

Ab Initio Structures: In order to gain some insight into how the activation barrier is affected by the presence of the ion consider the ab initio calculations on the structure

and energetics of the complexes. The  $\text{Li}^+(\text{NO})$  structure was optimized in the  $C_s$  point group and remained bent with  $\angle \text{Li} \cdots \text{O} - \text{N} = 175.2^\circ$ . The  $\text{Li} \cdots \text{O}$  distance is 1.965 Å and the  $\text{O} - \text{N}$  distance is 1.137 Å. The latter distance can be compared with the bond length of 1.127 Å in neutral NO.  $\text{Li}^+(\text{CO}_2)$  was optimized in the  $C_s$  and  $C_{2v}$  point groups. The bent  $C_s$  structure is not a local minimum; it changes to the linear  $C_{2v}$  structure upon optimization.

Four possible conformations of  $\text{Li}^+(\text{NO}_2)$  were examined and are shown in the diagram below. Their point groups are also given in the diagram. The most stable structure is II. The equilibrium geometries of  $\text{CO}_2$ ,<sup>23</sup>  $\text{NO}_2$ ,  $\text{Li}^+(\text{CO}_2)$ , and form II of  $\text{Li}^+(\text{NO}_2)$  are presented in Figure 3. Notice that there is a correlation between the electronic lithium ion affinities and the  $\text{Li} \cdots \text{O}$  bond lengths. As the  $\text{Li} \cdots \text{O}$  bond length decreases,  $\Delta E$  increases (Table III and Figure 3).



Compare the structures of  $\text{NO}_2$  and  $\text{Li}^+(\text{NO}_2)$  in Figure 3. In order to facilitate the reaction  $\text{NO}_2 + \text{CO} \rightarrow \text{CO}_2 + \text{NO}$ , it is desirable to lengthen (i.e., weaken) one of the  $\text{NO}$  bonds and to shorten the other. That is precisely what occurs in the presence of the  $\text{Li}^+$  ion. In fact, the same type of structural rearrangement occurs in the  $\text{Li}^+(\text{CO}_2)$  cluster (Figure 3) and in other lithium clusters, also.<sup>24,25</sup> This suggests that forming the  $\text{Alk}^+(\text{A})$  complex enhances the reaction between A and B by shifting the structure of A toward what it is expected to be in the transition state for the neutral reaction. For the above reaction that is toward  $\text{O} + \text{NO}$ .

Bond Strength vs. Bond Distance. We are not presently able to estimate how much the activation energy is lowered due to the above bond lengthenings and shortenings but we can estimate how much the N - O bond dissociation energy is reduced. Figure 4 is a plot of the logarithm of bond strength vs. bond distance for the N - O bonds in several molecules. The experimental bond lengths in NO, NO<sub>2</sub>, and

$\text{NO}_3$  are plotted as circles, pluses, and squares, respectively. These values fall on a reasonably straight line which is used for calibration. The calculated values for the N - O distances in  $\text{Li}^+(\text{NO}_2)$  and  $\text{NO}_2$  are indicated by the arrows. The estimated difference in the bond dissociation energy of the long N - O bond in  $\text{Li}^+(\text{NO}_2)$  and the bond dissociation energy of  $\text{NO}_2$  is then approximately 43 kcal mol<sup>-1</sup>. The increase in bond strength for the other N - O bond in  $\text{Li}^+(\text{NO}_2)$  is about the same. Therefore, the total bond strength of  $\text{NO}_2$  is approximately constant in  $\text{Li}^+(\text{NO}_2)$  and  $\text{NO}_2$ . Thus, the increase in bond length translates into ca. a 1/3 reduction in bond strength. This must surely translate into a lowering of the activation barrier as well, i.e.,  $E_a' < E_a$ .

**G. Components of the Lithium Cation Affinities.** The lithium cation affinity can be separated into four main attractive components - electrostatic, polarization, charge transfer, and dispersion.<sup>26</sup> For first row bases the electrostatic term is dominant; for second row bases both the electrostatic and polarization terms are important.<sup>24</sup> Since the maximum electrostatic interaction occurs along the dipole axis of a molecule,<sup>27</sup> most  $\text{Li}^+$  complexes have  $\text{Li} \cdots \text{X} - \text{Y}$  angles of 180°.<sup>10,24,25</sup> This is what is observed for  $\text{Li}^+(\text{CO}_2)$  (Figure 3). However,  $\angle \text{Li} \cdots \text{O} - \text{N}$  in  $\text{Li}^+(\text{NO})$  is not 180°, although the deviation from linearity is small at ca. 5°. Moreover,  $\text{NO}_2$  is not aligned along its symmetry axis in  $\text{Li}^+(\text{NO}_2)$  (Figure 3). The latter results suggest that polarization effects are more important in  $\text{Li}^+(\text{NO})$  and  $\text{Li}^+(\text{NO}_2)$  than they are in other  $\text{Li}^+$  complexes. In fact, the magnitudes of many of the parameters used to measure the size of the polarization contribution are larger for  $\text{Li}^+(\text{NO}_2)$  than they are for  $\text{Li}^+(\text{CO}_2)$ . For example, forming the cluster changes the O - X (X = N, C) bond lengths more in  $\text{Li}^+(\text{NO}_2)$  than in  $\text{Li}^+(\text{CO}_2)$  (Figure 3). Furthermore, the increase in electron density on the oxygen bonded to lithium and the decrease in electron density on the other oxygen are both greater for  $\text{NO}_2$  (0.182 e and 0.186 e, respectively) than they are for  $\text{CO}_2$  (0.137 e and 0.132 e, respectively, Figure 3) when the complexes are formed. In contrast, the electrostatic contribution to the lithium cation affinity is larger for  $\text{Li}^+(\text{CO}_2)$  than it is for  $\text{Li}^+(\text{NO}_2)$ . The  $\text{Li} \cdots \text{O}$  distance is slightly smaller (Figure 3), the 1s orbital energy of the  $\text{Li}^+$  accepting oxygen  $\epsilon_{1s}(\text{O})$  is less stable (-20.65782 au vs. -20.69138 au), and the charge on the oxygen in the isolated base is more negative (Figure 3) for  $\text{CO}_2$ . The compromise between the two components accounts for the similar magnitudes of the electronic lithium cation affinities of the two bases.

### Acknowledgment

The authors thank Dr. Michael J. Henchman for many helpful discussions. The support of the Air Force Geophysics Laboratory Information Resources Center is gratefully acknowledged.

## References

1. K. G. Spears, *J. Chem. Phys.* 57, 1842, 1850 (1972).
2. B. R. Rowe, A. A. Viggiano, F. C. Fehsenfeld, D. W. Fahey, and E. E. Ferguson, *J. Chem. Phys.* 76, 742 (1982).
3. D. W. Fahey, H. Böhringer, F. C. Fehsenfeld, and E. E. Ferguson, *J. Chem. Phys.* 76, 1799 (1982).
4. A. A. Viggiano, F. Howorka, D. L. Albritton, F. C. Fehsenfeld, N. G. Adams, and D. Smith, *Ap. J.* 236, 492 (1980).
5. Gaussian 82, release H, J. S. Binkley, M. Frisch, R. Krishnan, D. J. DeFrees, H. B. Schlegel, R. A. Whiteside, E. M. Fluder, R. Seeger, and J. A. Pople, c.1982, Carnegie-Mellon University.
6. P. C. Hariharan and J. A. Pople, *Mol. Phys.* 27, 209 (1974).
7. a) P. Pulay, *Molec. Phys.* 17, 197 (1969). b) H. B. Schlegel, S. Wolfe, F. Bernardi, *J. Chem. Phys.* 63, 3632 (1975).
8. G. W. Spitznagel, T. Clark, J. Chandrasekhar, P. v. R. Schleyer, *J. Comp. Chem.* 3, 363 (1983).
9. a) C. Møller, M. S. Plesset, *Phys. Rev.* 46, 618 (1934). b) J. A. Pople, J. S. Binkley, R. Seeger, *Int. J. Quantum Chem. Symp.* 10, 1 (1976).
10. J. E. Del Bene, *J. Comp. Chem.* 7, 259 (1986).
11. J. E. Del Bene, H. D. Mettee, M. J. Frisch, B. T. Luke, J. A. Pople, *J. Chem. Phys.* 87, 3279 (1983).
12. R. G. Keesee and A. W. Castleman, Jr., *J. Phys. Chem. Ref. Data*, in press.
13. Gas - Phase Chemiluminescence and Chemi - Ionization, ed. A. Fontijn, Elsevier Science, 1985.
14. R. L. Wooden and J. L. Beauchamp, *J. Am. Chem. Soc.* 100, 501 (1978).
15. D. J. DeFrees and A. D. McLean, *J. Comp. Chem.* 7, 321 (1986).
16. E. E. Ferguson in "Swarms of Electrons and Ions in Gases", ed. W. Lindinger, T. D. Mark, and F. Howorka, Springer Verlag, Vienna (1984).
17. These are derived from ion - induced dipole and ion - locked dipole potentials. The polarizabilities and dipole moments are from "Theory of Molecular Fluids. Vol. 1. Fundamentals," C. G. Gray and K. E. Gubbins, Clarendon Press, Oxford, 1984.
18. A. A. Viggiano, J. A. Davidson, F. C. Fehsenfeld, and E. E. Ferguson, *J. Chem. Phys.* 74, 6113 (1981).
19. J. W. Birks, B. Shoemaker, T. J. Leck, and D. M. Hinton, *J. Chem. Phys.* 65, 5181 (1976).
20. Handbook of Bimolecular and Termolecular Gas Reactions, ed. J.A. Kerr and S.J. Moss, CRC Press Inc., Boca Raton, Florida (1981).

21. A. T. Barfknecht, J. A. Dodd, K. E. Salomom, W. Tumas, and J. I. Brauman, *Pure & Appl. Chem.* 56, 1809 (1984) and references therein.
22. The maximum temperature dependence is that of the complex lifetime. The temperature dependence of the complex lifetime can be estimated by the procedures given in: a) D. R. Bates, *J. Chem. Phys.* 81, 298 (1984); b) E. Herbst, *J. Chem. Phys.* 82, 4017 (1982); c) A. A. Viggiano, *J. Chem. Phys.* 84, 244 (1986) and references therein.
23. R. A. Whiteside, M. J. Frisch, J. S. Binkley, D. J. DeFrees, H. B. Schlegel, K. Raghavachari, J. A. Pople, "Carnegie-Mellon Quantum Chemistry Archive," Department of Chemistry, Carnegie-Mellon University, Pittsburgh, PA 15123.
24. S. F. Smith, J. Chandrasekhar, and W. L Jorgensen, *J. Am. Chem. Soc.* 86, 3308 (1982).
25. E. Kaufmann, B. Tidor, and P. v. R. Schleyer, *J. Comp. Chem.* 7, 334 (1986).
26. K. Morokuma, *Acc. Chem. Res.* 10, 294 (1977).
27. a) P. J. Kollman, *J. Am. Chem. Soc.* 94, 1837 (1972). b) P. Kollman and S. Rothenberg, *J. Am. Chem. Soc.* 99, 1333 (1977).

Table I. Rates of Ion Enhanced Reactions

Reaction	Rate Constant (cm <sup>3</sup> s <sup>-1</sup> )	Temp(K)	Rate Enhancement <sup>c</sup>	E <sub>a</sub> kcal mol <sup>-1</sup>
$\text{Li}^+(\text{NO}_2) + \text{CO} \rightarrow \text{Li}^+(\text{CO}_2) + \text{NO}^{\text{a}}$	7(-12) <sup>b</sup>	213-294	$10^{30}$ <sup>e</sup>	28 <sup>h</sup>
$\text{Na}^+(\text{NO}_2) + \text{CO} \rightarrow \text{Na}^+(\text{CO}_2) + \text{NO}$	1(-12)	213-289	$10^{29}$ <sup>e</sup>	28 <sup>h</sup>
$\text{Li}^+(\text{NO}_2) + \text{H}_2 \rightarrow \text{products}$	<1(-14)	219	-	18 <sup>h</sup>
$\text{Li}^+(\text{HBr}) + \text{O} \rightarrow \text{Li}^+ + \text{HBrO}$	2(-10)	178-219	$10^5$ <sup>e</sup>	3.1 <sup>h</sup>
$\rightarrow \text{Li}^+ + \text{Br} + \text{OH}$				
$\text{Li}^+(\text{HBr})_2 + \text{O} \rightarrow \text{Li}^+ + \text{HBrO} + \text{HBr}$	2(-10)	178	$10^5$ <sup>e</sup>	3.1 <sup>h</sup>
$\text{Na}^+(\text{HBr}) + \text{O} \rightarrow \text{Na}^+ + \text{HBrO}$	1(-10)	219	$2 \times 10^4$ <sup>e</sup>	3.1 <sup>h</sup>
$\rightarrow \text{Na}^+ + \text{Br} + \text{OH}$				
$\text{Li}^+(\text{H}_2\text{S}) + \text{O} \rightarrow \text{Li}^+(\text{HSO}) + \text{H}^{\text{a}}$	2(-10)	219	$5 \times 10^4$ <sup>e</sup>	4.3 <sup>h</sup>
$\rightarrow \text{Li}^+ + \text{H}_2\text{SO}$				
$\text{Li}^+(\text{H}_2\text{S})_2 + \text{O} \rightarrow \text{Li}^+(\text{H}_2\text{SO}) + \text{H}_2\text{S}^{\text{a}}$	2(-10)	219	$5 \times 10^4$ <sup>e</sup>	4.3 <sup>h</sup>
$\rightarrow \text{Li}^+ + \text{H}_2\text{SO} + \text{H}_2\text{S}$				
$\text{Na}^+(\text{H}_2\text{S}) + \text{O} \rightarrow \text{Na}^+(\text{HSO}) + \text{H}^{\text{a}}$	1(-10)	178-219	$1.5 \times 10^5$ <sup>e</sup>	4.3 <sup>h</sup>
$\rightarrow \text{Na}^+ + \text{H}_2\text{SO}^{\text{h}}$				
$\text{Na}^+(\text{H}_2\text{S})_2 + \text{O} \rightarrow \text{Na}^+(\text{H}_2\text{SO}) + \text{H}_2\text{S}^{\text{a}}$	2(-10)	178	$3 \times 10^5$ <sup>e</sup>	4.3 <sup>h</sup>
$\rightarrow \text{Na}^+ + \text{H}_2\text{SO} + \text{H}_2\text{S}$				
$\text{Li}^+(\text{N}_2\text{O}) + \text{O} \rightarrow \text{Li}^+ + \text{N}_2 + \text{O}_2$	5(-13)	219	$10^{25}$ <sup>e</sup>	28 <sup>h</sup>
$\text{Li}^+(\text{N}_2\text{O}_5) + \text{NO} \rightarrow \text{Li}^+(\text{N}_2\text{O}_4) + \text{NO}_2$	1.2(-11) <sup>d</sup>	247-303	$\geq 10^9$ <sup>f</sup>	22 <sup>f</sup>
$\text{Na}^+(\text{N}_2\text{O}_5) + \text{NO} \rightarrow \text{Na}^+(\text{N}_2\text{O}_4) + \text{NO}_2$	3(-13) <sup>d</sup>	303	$\geq 4 \times 10^6$ <sup>f</sup>	22 <sup>f</sup>
$\text{K}^+(\text{N}_2\text{O}_5) + \text{NO} \rightarrow \text{K}^+(\text{N}_2\text{O}_4) + \text{NO}_2$	$\leq 5$ (-14) <sup>d</sup>	218	-	22 <sup>f</sup>
$\text{Li}^+(\text{O}_3) + \text{NO} \rightarrow \text{Li}^+ + \text{O}_2 + \text{NO}_2$	6(-11) <sup>d</sup>	220-280	$2 \times 10^4$ <sup>g</sup>	2.9 <sup>g</sup>
$\text{Na}^+(\text{O}_3) + \text{NO} \rightarrow \text{Na}^+ + \text{O}_2 + \text{NO}_2$	6.5(-11) <sup>d</sup>	163-243	$2 \times 10^5$ <sup>g</sup>	2.9 <sup>g</sup>
$\text{K}^+(\text{O}_3) + \text{NO} \rightarrow \text{K}^+ + \text{O}_2 + \text{NO}_2$	4.5(-12) <sup>d</sup>	125-163	$2 \times 10^5$ <sup>g</sup>	2.9 <sup>g</sup>

<sup>a</sup>For detailed information on the products see text. <sup>b</sup>7(-12) means  $7 \times 10^{-12}$ . <sup>c</sup>The rate constant in the presence of the alkali ion divided by the rate constant for the corresponding neutral reaction at the coldest temperature listed. <sup>d</sup>Data from Rowe et al.<sup>2</sup> <sup>e</sup>Neutral rate constant calculated from the tabulation of Kerr and Moss.<sup>20</sup> <sup>f</sup>A limit to the neutral reaction rate constant can be obtained from the thermal decomposition of  $\text{N}_2\text{O}_5$  in the presence of NO. The data of Viggiano et al.<sup>18</sup> are used here. <sup>g</sup>Neutral rate constant from Birks et al.<sup>19</sup>

Table II. Calculated Total Energies ( $E_T$ ) in hartrees.

Molecule	Point group	Basis	HF	MP2	MP3
Li <sup>+</sup>		6-31G*	-7.23554 <sup>a</sup>		
		6-31+G*	-7.23554 <sup>b</sup>	-7.23554 <sup>b</sup>	-7.23554 <sup>b</sup>
O		6-31G*	-74.78393 <sup>a</sup>		
		6-31+G*	-74.78676	-74.88529	-74.89852
NO	$C_{\infty v}$	6-31G*	-129.24788		
		6-31+G*	-129.25165	-129.56539	-129.56347
CO <sub>2</sub>	$D_{\infty h}$	6-31G*	-187.63418		
		6-31+G*	-187.63879	-188.11216	-188.09832
NO <sub>2</sub>	$C_{2v}$	6-31G*	-204.03149		
		6-31+G*	-204.03833	-204.56557	-204.54433
LiO <sup>+</sup>	$C_{\infty v}$	6-31G*	-82.02031		
		6-31+G*	-82.02164	-82.12072	-82.13396
Li <sup>+</sup> (NO)	$C_s$	6-31G*	-136.50479		
		6-31+G*	-136.50678	-136.81482	-136.81500
Li <sup>+</sup> (NO <sub>2</sub> ) (II)	$C_s$	6-31G*	-211.30064		
		6-31+G*	-211.30487	-211.82729	-211.80932
Li <sup>+</sup> (CO <sub>2</sub> )	$C_{\infty v}$	6-31G*	-194.90516		
		6-31+G*	-194.90799	-195.37855	-195.36635

<sup>a</sup>Reference 23. <sup>b</sup>Reference 25.

Table III. Computed Values of  $\Delta E$  in kcal/mol.<sup>a</sup>

Complex	Basis	HF	MP2	MP3
LiO <sup>+</sup>	6-31G*	0.53		
	6-31+G*	-0.41 <sup>b</sup>	-0.069 <sup>b</sup>	-0.063 <sup>b</sup>
Li <sup>+</sup> (NO)	6-31G*	13.41		
	6-31+G*	12.29	8.72	10.03
Li <sup>+</sup> (CO)	6-311+G(2d,2p)			14.5 <sup>c</sup>
Li <sup>+</sup> (NO <sub>2</sub> )	6-31G*	21.09		
(II)	6-31+G*	19.45	16.43	18.48
Li <sup>+</sup> (CO <sub>2</sub> )	6-31G*	22.24		
	6-31+G*	21.12	19.36	20.39

<sup>a</sup>6-31G\* equilibrium structures were utilized at each calculational level. <sup>b</sup>The negative sign indicates that LiO<sup>+</sup> is not bound at this level of calculation. <sup>c</sup>Bonded through the carbon. This is the MP4SDQ/6-311+G(2d,2p)//HF/6-31G\*  $\Delta E$  corrected for zero-point energy changes and temperature effects.<sup>10</sup>

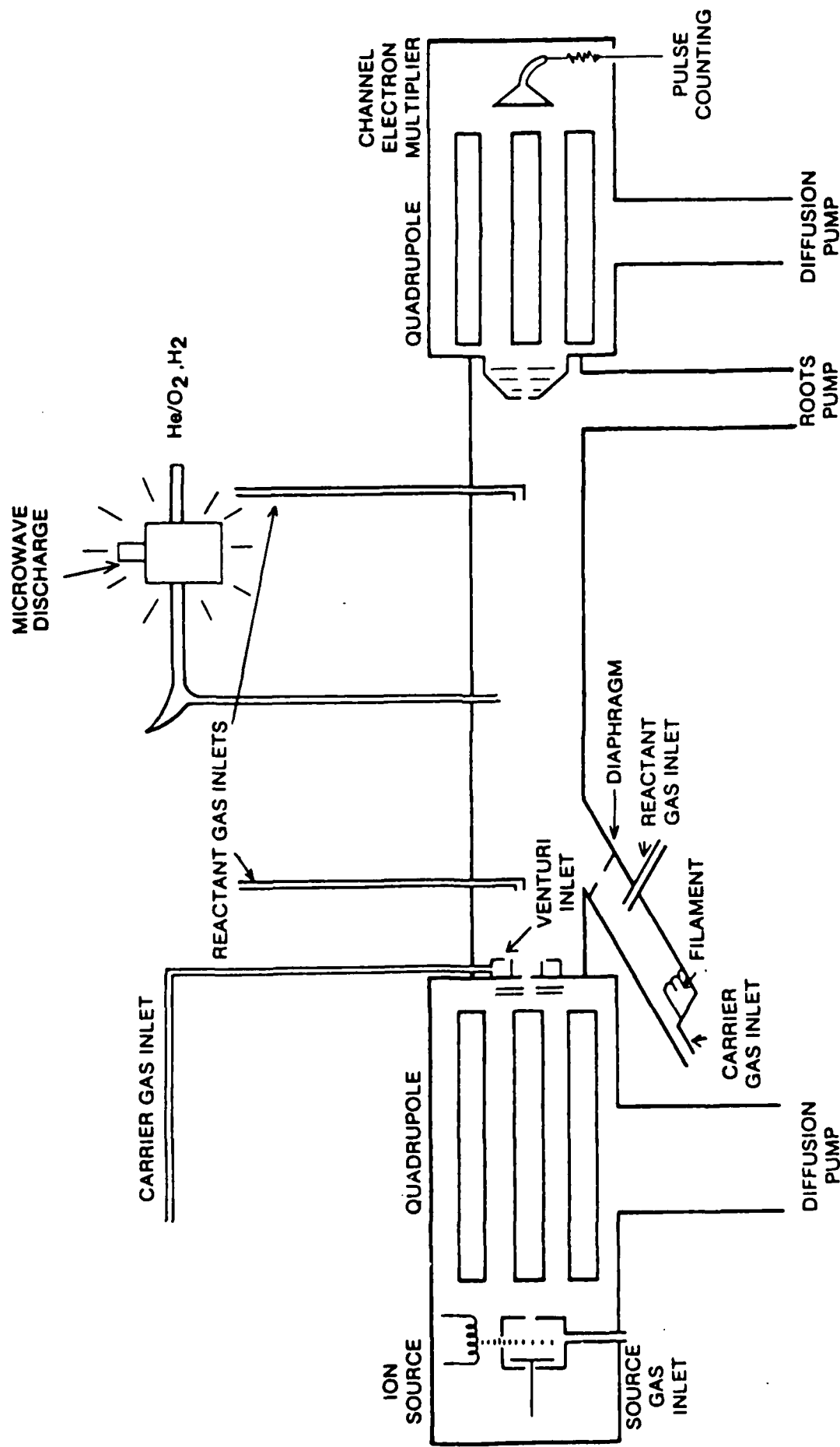


Figure 1. Diagram of the newly constructed flowing afterglow - selected ion flow tube apparatus used in this work.

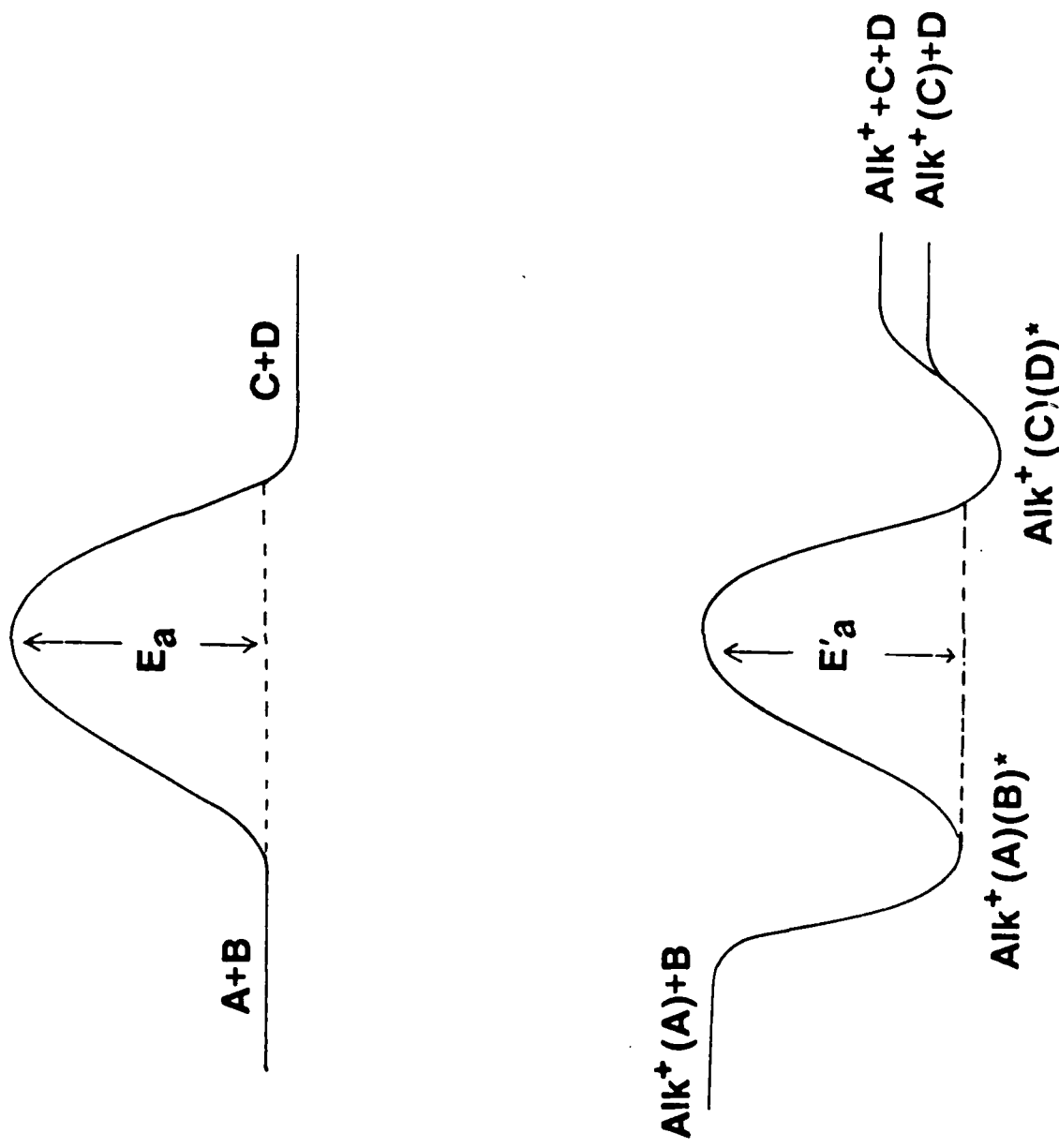


Figure 2. The top drawing is a schematic of the reaction coordinate for a reaction between two neutrals A and B. The bottom drawing is a schematic of the reaction coordinate for a reaction between an alkali ion - neutral A complex  $\text{Alk}^+(\text{A})$  and neutral B.

## 6-31G\* OPTIMIZATION

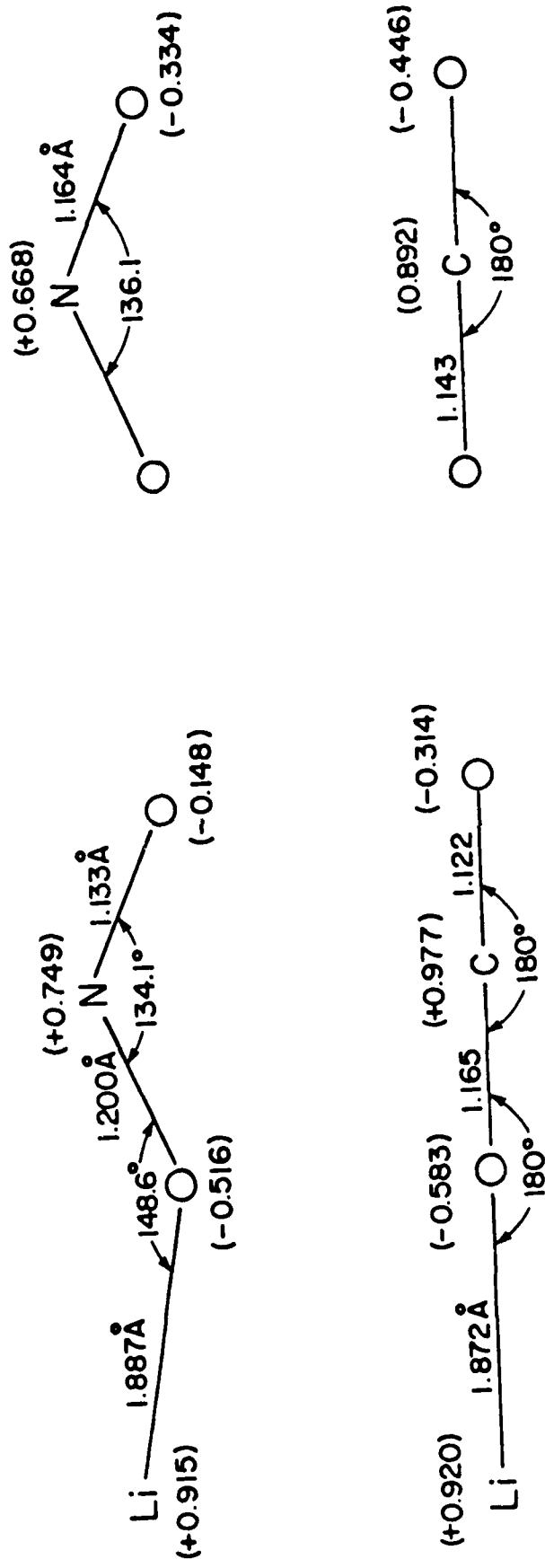


Figure 3. 6-31G\* equilibrium geometries of  $\text{NO}_2$ ,  $\text{CO}_2$ ,  $\text{Li}^+(\text{NO}_2)_2$ , and  $\text{Li}^+(\text{CO}_2)_2$ . The structure for  $\text{CO}_2$  is from reference 23.

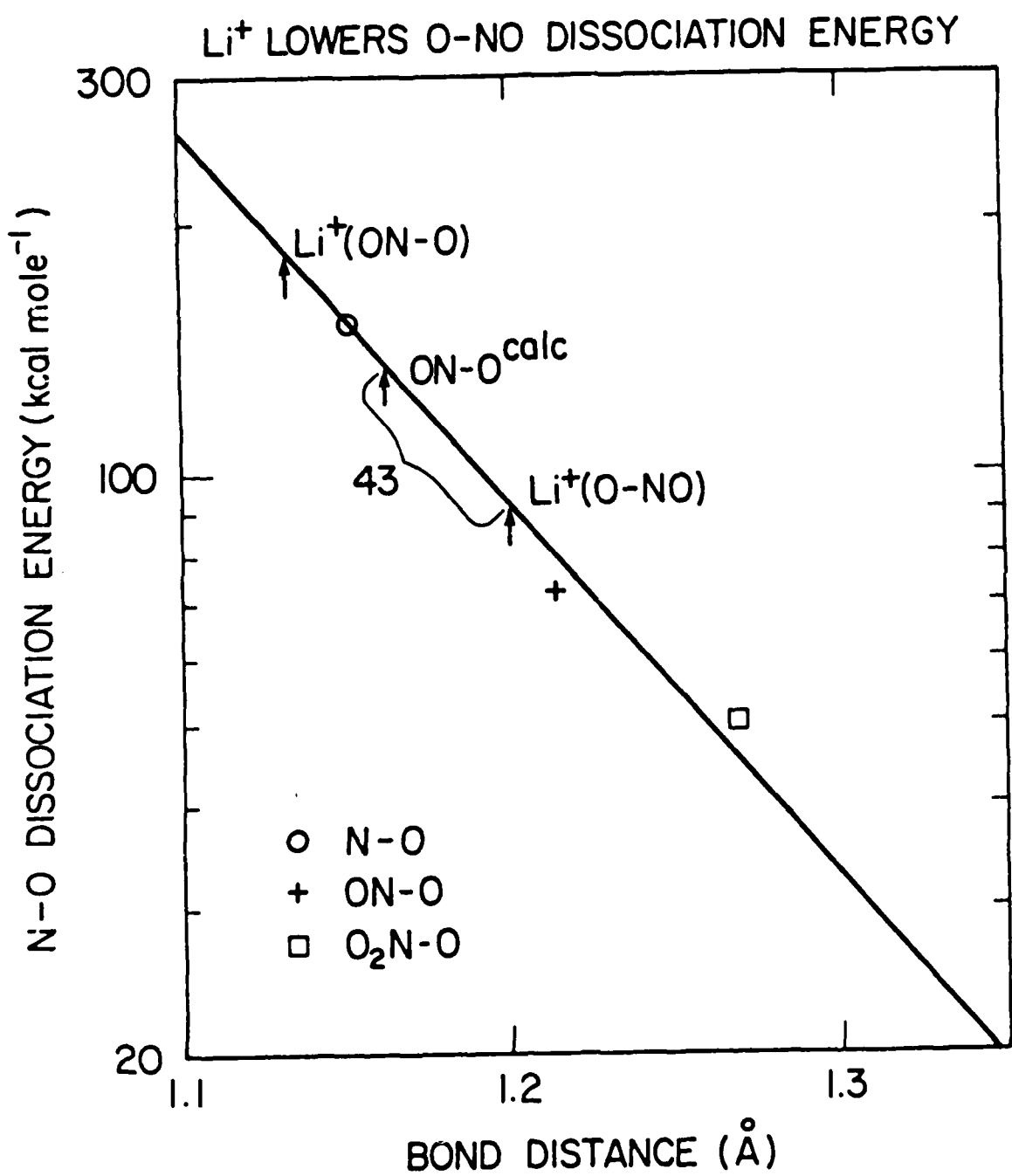


Figure 4. N - O bond dissociation energies in kcal mol<sup>-1</sup> vs N - O bond distances in Å.

### Recommendations

It would be useful to carry out theoretical calculations on some of the  $\text{Na}^+$  clusters and more of the  $\text{Li}^+$  clusters studied experimentally in this work to determine: 1) additional lithium and sodium cation affinities, which are not known experimentally, 2) whether the structural rearrangements found on complex formation are a universal phenomenon, and 3) whether the relative rates of the lithium and sodium reactions correlate with the observed structural rearrangements.

1985-1986 AFGL-SCEEE GEOPHYSICAL SCHOLAR PROGRAM

Sponsored by the

AIR FORCE GEOPHYSICS LABORATORY

Conducted by the

SOUTHEASTERN CENTER FOR ELECTRICAL ENGINEERING EDUCATION

FINAL REPORT

COLLISIONAL QUENCHING OF VIBRATIONALLY EXCITED  
NH IN N<sub>2</sub>/H<sub>2</sub>

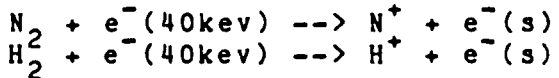
Prepared By: Dorothy J. Flanagan

Research Location: Air Force Geophysics Laboratory

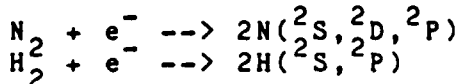
Date: September 10, 1986

Collisional quenching of NH generated from N<sub>2</sub>/H<sub>2</sub> mixtures by high energy electron impact dissociation.  
Summary Report.

A study of collisional quenching of the NH chemiluminescence generated by the high energy electron bombardment of mixtures of H<sub>2</sub> and excess N<sub>2</sub> has been undertaken. A model mechanism has been formulated for the quenching process. The pathway of imidogen formation involves several steps: primary ion formation via electron stripping reactions



generating secondary electrons which interact more strongly with the initial species leading to dissociation.



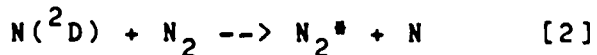
Of the dissociation species, only N<sup>2</sup>D has the energetic and mechanistic characteristics necessary to generate NH(v<4).

On beam termination three processes dominate the kinetics:

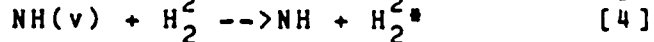
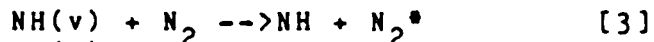
production of vibrationally excited NH



quenching of N<sup>2</sup>D by molecular nitrogen



collisional quenching of imidogen



If the assumptions are made that N<sup>2</sup>D production is a consequence of electron irradiation and that the population of excited imidogen is proportional to that of N<sup>2</sup>D during bombardment, the quenching rates of imidogen can be deduced.

The rate expression for imidogen decay for this model can be formulated as:

$$[NH(v)]/[NH(v)]_0 = \{-Ae^{-Bt} + Be^{-At}\}/(B-A)$$

where A=k<sub>1</sub>[H<sub>2</sub>] + k<sub>2</sub>[N<sub>2</sub>] and B=k<sub>3</sub>[N<sub>2</sub>] + k<sub>4</sub>[H<sub>2</sub>].

The concentrations of N<sub>2</sub> and H<sub>2</sub> are experimental parameters and the rate constants k<sub>1</sub> and k<sub>2</sub> have been have been previously determined[1], thus the quenching rates k<sub>3</sub> and k<sub>4</sub> may be obtain through curve fitting the experimentally determined ratio [NH(v)]/[NH(v)]<sub>0</sub>.

To this end a series of experiments have been at the Air Force Geophysics Laboratory conducted using the "hot" LABCEDE apparatus which has been described in detail elsewhere.[2] Continuous flows of  $N_2$  and  $H_2$  admixtures at controlled pressures were subjected to the bombardment of a pulse collimated 37 kev electron beam running in an 11% duty cycle. Fluorescence was monitored by means of an off axis Michelson interferometer with a  $LN_2$  cooled InSb detector. Interferograms were recorded for mixtures of 0.05, 0.10, and 0.20 torr  $H_2$  with  $N_2$  at pressures of 7.5, 10, 15, 20, 25, 30, 35, and 40 torr. Fast Fourier transformation was performed on each of these interferograms and the resultant spectra obtained. The desired ratios  $[NH(v)]/[NH(v)]_0$  was then determined by integration of the relevant region of the spectra.

Curve fitting routines have been devised to fit the ratio to the model rate equations. Various schemes have been tested including simultaneous two parameter fits, single parameter fits using literature values for the appropriate rate constants, and fits with a variety of noise treatments. Thus far only whole band analysis has been considered where the total population of NH independent of vibrational state has been measured. From these preliminary treatments the quenching rate constants have been estimated. The rate of quenching of NH by  $N_2$ ,  $k_3$ , has been found to be of the order of  $1 \times 10^{-12} \text{ cm}^3/\text{sec}^2$  while the quenching rate by  $H_2$ ,  $k_4$ , is of the order of  $3 \times 10^{-11} \text{ cm}^3/\text{sec}$ . It must be stressed that these finding are preliminary estimates especially for  $k_4$  and may be revised as a more thorough analysis is completed. It may prove desirable to take interferograms at additional  $H_2$  pressures to improve the fit of  $k_4$ . A better accounting of the system time constants would also be highly desirable perhaps through fits to an RC filtered rate equation and state dependent analysis remains to be performed.

#### References

1. D. Husain, S. K. Mitra, and A. N. Young, J. Chem. Soc. Faraday Trans. 2, 70, 1721 [1974].
2. G. E. Caledonia, B. D. Green, and R. E. Murphy, J. Chem. Phys., 71, 4369 [1979].

1985-1986 AFGL-SCEEE GEOPHYSICAL SCHOLAR PROGRAM

Sponsored by the  
AIR FORCE GEOPHYSICS LABORATORY

Conducted by the  
SOUTHEASTERN CENTER FOR ELECTRICAL ENGINEERING EDUCATION

FINAL REPORT

LINE COUPLING IN THE FUNDAMENTAL  
Q BRANCH OF CO<sub>2</sub> AT 667 CM-1

Prepared by: Michael Hoke

Research Location: Air Force Geophysics Laboratory

AFGL Research Contact: Shepard A. Clough

Date: 31 August 1986

#### ACKNOWLEDGEMENTS

I would like to thank the Air Force Geophysical Laboratory and the Southeastern Center for Electrical Engineering Education for the opportunity to study and work at the AFGL laboratory.

I would like also to thank Tony Clough for his help, encouragement and support during this study.

Finally, I would like to acknowledge the very interesting and useful conversations with Tony Clough and Frank Kneizys.

LINE COUPLING IN THE FUNDAMENTAL Q BRANCH OF CO<sub>2</sub>

AT 667 CM-1

MICHAEL HOKE

ABSTRACT

Line coupling has been studied in the fundamental Q branch of CO<sub>2</sub> at 667 CM-1. Transmittance data has been collected using the high resolution BOMEM Fourier transform interferometer at the National Bureau of Standards Laboratory in Washington D.C. In the simplified analysis line coupling coefficients  $y$  are included in the line shape by adding a term for each line proportional to  $y$  and asymmetric about the line position. The coupling coefficients are given in terms of the off diagonal elements of the relaxation matrix  $w(j,k)$ . These elements were determined from the collision broadened half widths using a three parameter fitting law expression. The agreement between the observed and calculated data at the pressures for which data was recorded (640, 380 and 190 Torr) was good.

## I) INTRODUCTION AND OBJECTIVES

Line coupling is an effect which is increasingly being recognized as important in the interpretation of molecular spectra. Also referred to as line interference or rotational relaxation the effect is well known in the spectrum of O<sub>2</sub> in the microwave(1,2,3). The effect has also been observed in Raman spectra of N<sub>2</sub> and CO(4) and NO(5) and more recently in laser diode absorption spectra of CO<sub>2</sub>(6). Line coupling has been discussed theoretically in the literature(7,8,9,10), and there has been increasing interest in developing computationally efficient and accurate schemes to model the effect(1,4,6,11,12). We have applied a simple scheme, after Smith(3), similar to Rosasco(4) and Strow(6) to the fundamental Q branch of CO<sub>2</sub>. This Q branch is of particular interest because the lines are close together and the coupling large but also because of its use in remote sensing of the atmosphere. Recently Armstrong(13) and Braun(14) have demonstrated through calculations that line coupling is a significant effect in this Q branch. What follows is a brief description of the modeling scheme and some preliminary results.

## II) THEORY, EXPERIMENTAL DETAILS AND DATA ANALYSIS

The expression for the absorption coefficient K(v) can be written formally in terms of the spectral density function  $\phi$  as(3)

$$k(v) = \frac{4\pi^2}{3hc} n \{1 - e^{-\beta hc v}\} v \text{Im}\{I(v)\} \quad \text{Eq.1}$$

with

$$I(v) = \frac{1}{\pi} \sum_{jk}^N d_j \langle j | \{ (v - v^0) - i\Gamma_w \}^{-1} | k \rangle d_k \rho_k \quad \text{Eq.2}$$

Here  $\langle j | v | k \rangle = v^* I$  where  $v$  is the frequency and  $I$  the identity matrix.  $\langle j | v_0 | k \rangle = v(j) * \delta(j, k)$  a diagonal matrix of transition frequencies. If the matrix  $\langle j | w | k \rangle = w(j, k)$ , referred to as the rate or relaxation matrix, were diagonal the impact line shape would be obtained. The Liouville space states(8)  $\langle j |$  and  $| k \rangle$  are products of the upper and lower Schrodinger states for line  $j$  and line  $k$ . The diagonal elements  $w(j, j)$  of the rate matrix are the impact(Lorentzian) half-widths. The off diagonal elements  $w(j, k)$  connect line  $j$  to line  $k$ . Also, in Eq.1  $n$  is the column count [molecules/cm\*\*2]; in Eq.2 the  $d$ 's are reduced(3) dipole moment matrix elements and  $\rho(k)$  is the Boltzmann factor for the lower state of line  $k$ .

In general a large number of lines are usually coupled and to avoid calculating the inverse  $\{v - v_0 - iPw\}^{-1}$  at each frequency  $v$  Smith(3) and Rosenkranz(1) have applied a perturbation technique to the matrix  $\{v_0 + iPw\}$ . Writing the eigenvalues and eigenvectors as power series with pressure as the expansion parameter Eq.3 is obtained, for the infrared, to first order in pressure.

$$I(v) \rightarrow \frac{1}{\pi} \sum_k^N d_k^2 \rho_k \left[ \frac{Pw_{kk}}{(v - v_k)^2 + (Pw_{kk})^2} + \frac{P(v - v_k) Y_k}{(v - v_k)^2 + (Pw_{kk})^2} \right] \quad \text{Eq.3}$$

The first term is the impact line shape. In the second term, asymmetric with respect to transition frequency  $v(k)$ , the quantities  $y(k)$

$$Y_k = 2 \sum_{j \neq k}^N (d_j/d_k) w_{jk} / (v_k - v_j) \quad \text{Eq.4}$$

contain the contributions from line coupling, one  $y$  for each line.

The quantities (  $\rho(k)*d(k)**2$  ) and (  $d(j)/d(k)$  ) can be related to the line intensities which are included in the AFGL Atmospheric Absorption Line Parameter Compilation(15).

The elements of the relaxation matrix  $w(j,k)$  are given as sums of matrix elements of the S or collision matrix, each averaged over all impact parameters and velocities(2,3,14). Each element contains contributions from elastic reorientational and inelastic rotational transitions. If it is assumed that the inelastic transition contributions dominate, then a simple representation of the rate matrix employing "fitting laws"(12) has previously been used to model molecular spectra(4,5). We have used a fitting law expression (12):

$$w_{jk} = \frac{1}{2}(w_{jk}(l) + w_{jk}(u)) \quad \text{Eq.5}$$

with

$$w_{jk} = A_1 \left[ \frac{|\Delta E|}{B_0} \right]^{-A_2} \exp \left[ -A_3 \frac{|\Delta E|}{kT} \right] \quad \text{Eq.6}$$

The first factor in  $w(j,k)$  is referred to as the "power gap law" and the second as the "exponential gap law"(12). The energy gaps  $\Delta E(l)$ ,  $\Delta E(u)$  are the energy differences between the lower(l), upper(u) states of the coupled lines j and k. A1, A2 and A3 are adjustable parameters. If  $w(j,k)$  is the rate from line k to j, then the rate from line j to k is given by satisfying detailed balance,

$$w_{jk}\rho_k = w_{kj}\rho_j \rightarrow w_{kj} = w_{jk} \frac{\rho_k}{\rho_j} \quad \text{Eq.7}$$

In addition if only inelastic transition rates are considered the sum over the rows of the rate matrix of a given column is zero,

$$\sum_j^N w_{jk} = 0 \quad \text{Eq.8}$$

This expression allows the off diagonal elements of a column to be related to the diagonal element, which is the Lorentz width

$$w_{kk} = \alpha_k^0 = - \sum_{j \neq k} w_{jk} \quad k = 1, N \quad \text{Eq.9}$$

Eq.9 (with Eqs.5,6) is used to estimate A1, A2 and A3 which are adjusted until the sums ( $k=1, \dots, N$ ) best approximate the Lorentz widths, in the sense of least squares. Since the model  $w(j,k)$  Eq.6 is non-linear in the parameters A2 and A3 an iterative fitting routine was necessary.

### III) RESULTS AND DISCUSSION

Eq.9 has been fit to the recently measured N2-broadened CO2 widths of Arie et al(16). These are the widths which will be incorporated into the new 1986 version of the AFGL Line Parameter Compilation(17). As Fig.1 shows the difference between the one atmosphere observed and calculated half-widths is less than 5% over most of the range of M. The estimated parameter values were:  $\langle A1 \rangle = 0.01211$ ,  $\langle A2 \rangle = 0.3272$ ,  $\langle A3 \rangle = 1.079$ . With A1, A2 and A3 determined the rate matrix  $w(j,k)$  can be calculated and from it the  $y(k)$ 's, which are shown in Fig.2 and listed in Table 1 for the fundamental Q branch. With the  $y$ 's determined the spectrum can be calculated in a straightforward way from Eqs.1,3. It can be noted that in Eq.3 each asymmetric term varies with  $v$  as  $\pm 1/v$  (depending

on the sign of  $y$ ) far from the line center. The sum of these terms can grow with  $v$  unless(7):

$$\sum_k^N d_k^2 \rho_k Y_k = 0 \quad \text{Eq.10}$$

which will be true only if the rate matrix elements satisfy detailed balance, Eq.7.

One calculation for the fundamental Q branch is shown in Fig.3 corresponding to the specified sample conditions listed there. The upper curve includes line coupling. The lower curve has no coupling; the absorption coefficient is the superposition of impact(Lorentzian) line shapes. Included in both calculations are the contributions from the many other (mostly weak) lines in the spectral region which are not coupled to the Q branch lines but do contribute to the observed absorptance. The line parameters for these lines were taken from the 1986 AFGL Line Parameter Compilation(17) as were the line positions and strengths for the Q branch lines.

Also included in Fig.3 is an observed spectrum corresponding to the sample conditions listed there. It was obtained with the BOMEM Fourier transform interferometer at the National Bureau of Standards(NBS) Laboratory in Washington D.C. The sample was an NBS standard reference gas mixture of  $0.9640 \pm 0.0005\%$  CO<sub>2</sub> in dry nitrogen contained in a 10 cm. cell with KBr windows. The optical path was evacuated or purged with nitrogen. The signal was collected with a liquid nitrogen cooled Mercury Cadmium Telluride detector; three hundred high resolution interferograms were

coadded over a twelve hour period before transformation to yield a signal to noise ratio of approximately 65 to 1. The resolution is 0.012 CM-1 using a Hamming apodization function. Low resolution (0.05 CM-1), high signal to noise ratio (1000 to 1) empty cell background spectra were also collected before and after the high resolution data. They were in very good agreement and were used to produce the Transmittance spectrum shown in Fig.3. To check for instrumental distortions in the data several small spectral regions including relatively isolated low J fundamental P and R branch lines were compared with calculations. Over a fairly large ( $\approx 25$  CM-1) spectral range including the fundamental Q branch the background was found to be shifted by an almost constant amount of four percent. This shift is included in the calculations in Fig.3. Also, a constant frequency shift of approximately 0.015 CM-1 was eliminated by adjusting the positions of several P and R branch lines, including P<sub>2</sub>, P<sub>4</sub>, R<sub>2</sub> and R<sub>4</sub> in Fig.3. Otherwise the agreement between observed and calculated P and R branch lines was found to be very good.

Considering the Q branch, the difference between the observed and calculated spectra (obs.-cal.) in Fig.3 shows that the agreement is good. Some difference is found near the base line where the absorption coefficient is large and changing rapidly with frequency. Since the elements  $w(j,k)$  are given in terms of the collision half-widths, Eq.9, they would be expected to scale as the half-widths do with pressure (see also Ben-Reuven(8)). Other room temperature spectra were collected with similar experimental

conditions but N<sub>2</sub> broadening pressures of 380 and 190 Torr. The observed and calculated data were in good agreement. One atmosphere air broadened line coupling coefficients were determined from the values in Table 1 by assuming O<sub>2</sub> broadening to be 85% of N<sub>2</sub> broadening, based on the O<sub>2</sub> broadened CO<sub>2</sub> widths of Arie et al(16) and Bulanin et al(18). These values have been included in the 1986 version of the line parameter listing and are about 97% of those in Table 1.

Straw and Gentry(6) have also studied line coupling in CO<sub>2</sub>, in the 11102-00001 band of the principal isotope located at 1932.47 CM-1. These authors fit the N<sub>2</sub> broadened widths of Yamaoto et al(19) to determine A<sub>1</sub>, A<sub>2</sub>, A<sub>3</sub> and their values (and consequently their w(j,k)'s) are slightly different than ours. We also tried using these same widths but found the widths of Arie et al(16) gave a better calculated fit to the observed fundamental P and R branch lines, including those shown in Fig.3.

Cousin et al have proposed that line coupling is a significant effect in the v<sub>3</sub> fundamental R branch near the band head and have employed a symmetrized two parameter fitting law model including only the exponential gap law. For comparison we applied their model to the widths of Arie et al(16). The estimated A<sub>1</sub>, A<sub>2</sub> and A<sub>3</sub> ( and w(j,k) ) values were different than those given above, but the y's calculated from them were very close to those reported in Table 1.

No data is available from which the temperature dependence of the rate matrix elements and y's can be determined. This will be a topic of future study.

## REFERENCES

- (1) PHILIP W. ROSENKRANZ, IEEE TRANSACTIONS on ANTENNAS and PROPAGATION, AP-23, 498(1975).
- (2) KAI S. LAM, JQSRT, 17, 351(1977).
- (3) EARL W. SMITH, J. CHEM. PHYS., 74, 6658(1981).
- (4) G.J. ROSASCO, W. LEMPERT, W.S. HURST and A. FEIN, CHEM. PHYS. LETTERS, 97, 435(1983).
- (5) W. LEMPERT, G.J. ROSASCO and W.S. HURST, J. CHEM. PHYS., 81, 4241(1984).
- (6) L. LARRABEE STROW and BRUCE M. GENTRY, J. CHEM. PHYS., 84, 1149(1986).
- (7) MICHEL BARANGER, PHYSICAL REVIEW, 111, 494(1958).
- (8) A. BEN-REUVEN, PHYSICAL REVIEW, 145 7(1966).
- (9) U FANO, PHYSICAL REVIEW, 131, 259(1963).
- (10) A.C. KOLB, and H. GRIEM, PHYSICAL REVIEW, 111, 514(1958).
- (11) ANDREW E. DePRISTO and HERSCHEL RABITZ, J. CHEM. PHYS., 68, 1981(1978).
- (12) TIMOTHY A. BRUNNER and DAVID PRITCHARD, DYNAMICS of the EXCITED STATE, ADVANCES in CHEMICAL PHYSICS VOL. L, JOHN WILEY and SONS, 1982.
- (13) R.L. ARMSTRONG, APPL. OPTS., 21, 2141(1982).
- (14) CHARLES BRAUN, J. MOL. SPEC., 93, 1(1982).
- (15) L.S. ROTHMAN, R.R. GAMACHE, A. BARBE, A. GOLDMAN, J.R. GILLIS, L.R. BROWN, R.A. TOTH, J.M. FLAUD and C. CAMY-PEYRET, APPL. OPTS., 22, 2247(1983).
- (16) E. ARIE, N. LACOME, PL. ARCAS and A. LEVY, APPL. OPTS., in press.
- (17) LAURENCE S. ROTHMAN, APPL. OPTS., 25, 1795(1986).
- (18) M.O. BULANIN, V.P. BULYCHEV and E.B. KHODOS, OPT. SPECTROSC., 48, 403(1980).
- (19) G. YAMAMOTO, M. TANAKA and T. AOKI, JQSRT, 9, 371(1969).

TABLE I  
NITROGEN BROADENED LINE COUPLING COEFFICIENTS  $y(M)$

<u>M</u>	<u>y(M)</u>	<u>M</u>	<u>y(M)</u>
2	2.09	44	-0.0562
4	0.411	46	-0.0544
6	0.110	48	-0.0527
8	0.00737	50	-0.0512
10	-0.0387	52	-0.0494
12	-0.0602	54	-0.0480
14	-0.0709	56	-0.0465
16	-0.0763	58	-0.0452
18	-0.0781	60	-0.0439
20	-0.0786	62	-0.0427
22	-0.0776	64	-0.0415
24	-0.0760	66	-0.0403
26	-0.0744	68	-0.0392
28	-0.0725	70	-0.0382
30	-0.0704	72	-0.0371
32	-0.0681	74	-0.0362
34	-0.0659	76	-0.0353
36	-0.0639	78	-0.0345
38	-0.0619	80	-0.0336
40	-0.0599	82	-0.0328
42	-0.0580	84	-0.0322

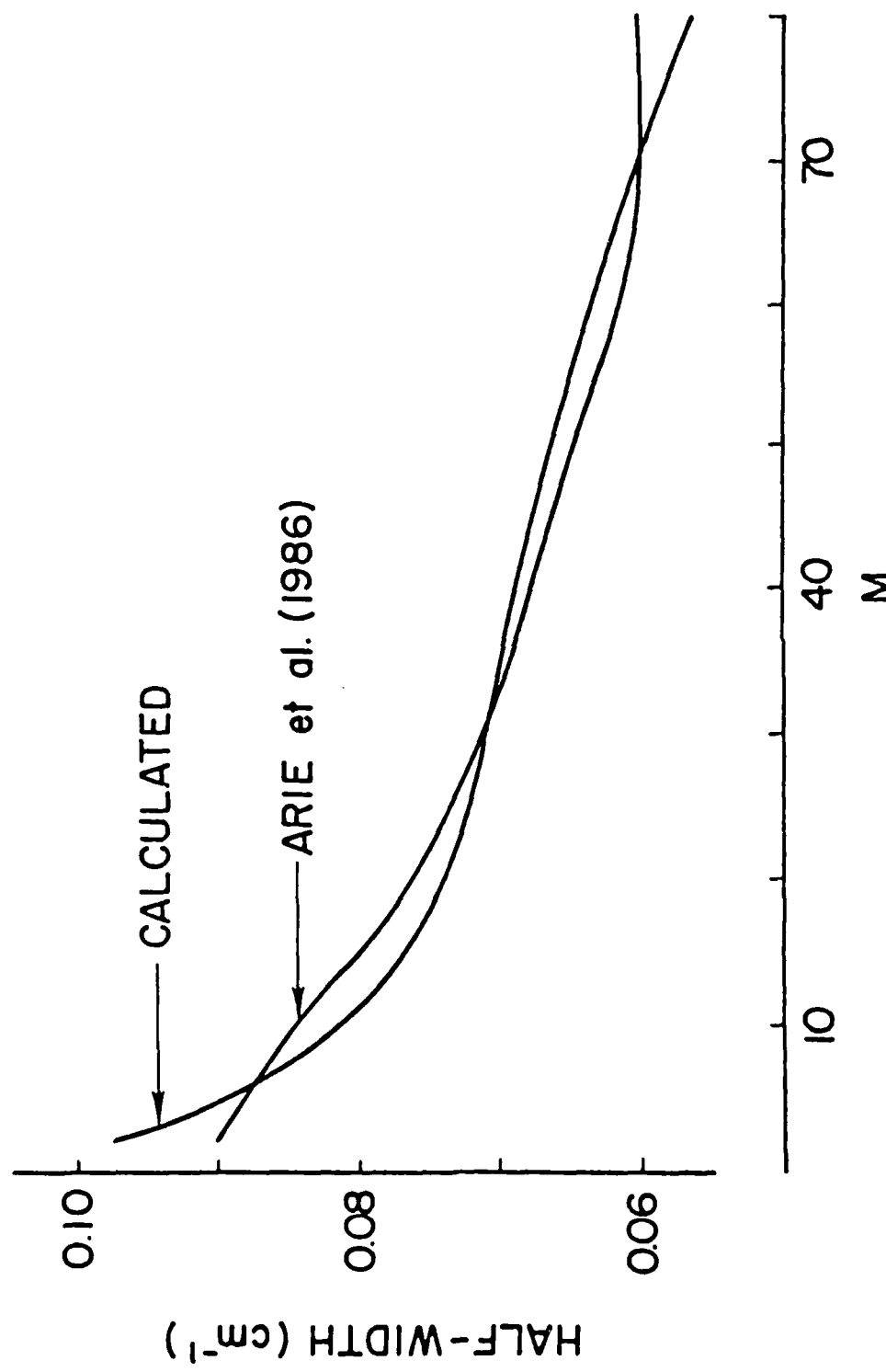


FIGURE 1: Comparison of observed one atmosphere N<sub>2</sub> broadened CO<sub>2</sub> halfwidths of Arie et al.(16) and those fit to the observed using the model described in the text.

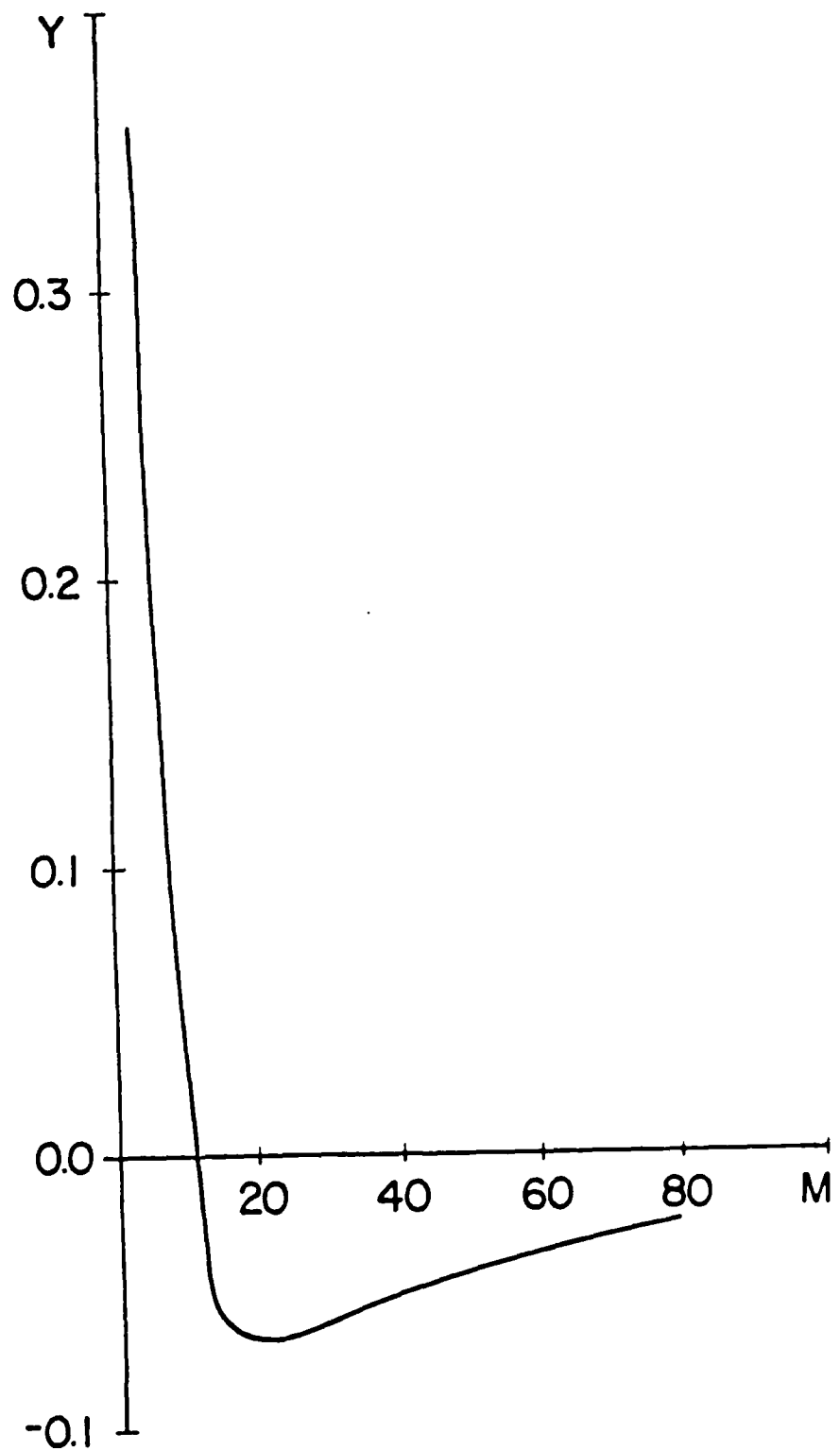
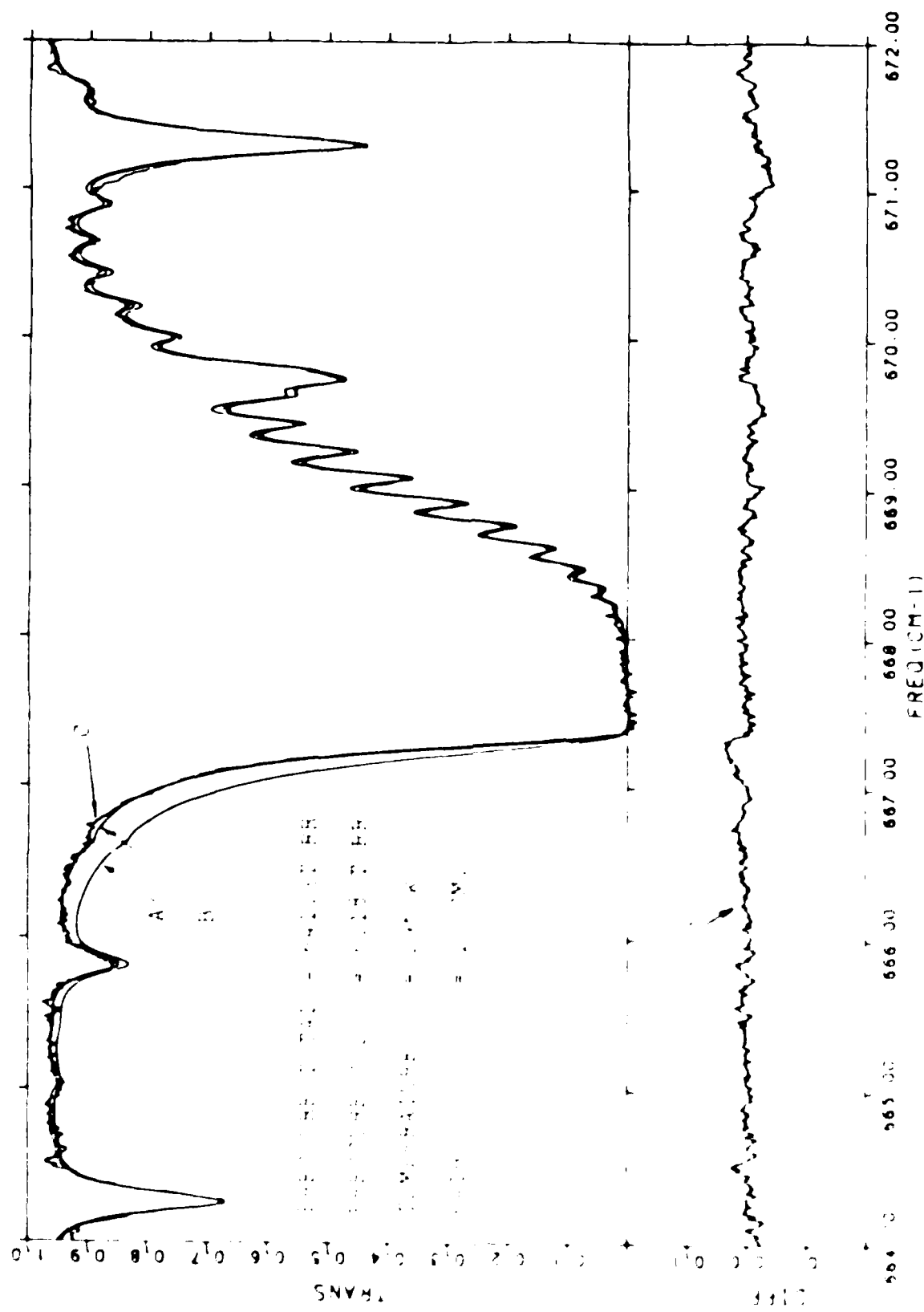


FIGURE 2: One atmosphere line coupling coefficients  $y$  versus  $M$  for N<sub>2</sub> broadening of CO<sub>2</sub> calculated from Eqs. 4, 5 and  $\langle A_1 \rangle = 0.01211$ ,  $\langle A_2 \rangle = 0.3272$ ,  $\langle A_3 \rangle = 1.079$ .



1985-1986 AFGL-SCEEPE GEOPHYSICAL SCHOLAR PROGRAM

Sponsored by the

AIR FORCE GEOPHYSICS LABORATORY

Conducted by the

SOUTHEASTERN CENTER FOR ELECTRICAL ENGINEERING EDUCATION

FINAL REPORT

IMPROVING THE RESOLUTION OF INFRARED SPECTRAL LINES  
FROM FOURIER TRANSFORM SPECTROSCOPY (FTS)

Prepared By: Samuel J. Howard

Research Scientist - Air Force Geophysics Laboratory

Date: August 29, 1986

FINAL REPORT  
for the Geophysics Scholar program supported by SCEEE  
under contract ending Aug. 31, 1986

The primary focus of the research at the Air Force Geophysics Laboratory has been on improving the resolution of infrared spectral lines from Fourier transform spectroscopy (FTS).

The theory is based on the minimum-negativity constraint. The theoretical calculations based on this constraint were carried out earlier by the author<sup>1</sup>. The attempt was made to minimize in a least-squares sense the negative values of a discrete bandlimited function by the fitting of a discrete function formed from the high Fourier frequencies only. This resulted in a set of nonlinear equations in the coefficients of these high Fourier frequencies which have to be solved for each individual set of data treated.

The work at AFGL has been devoted principally to finding numerical solutions to these nonlinear equations that reduce both computer memory requirements and computational time. The only known means of solution for these equations at present are iterative. The Newton-Raphson iterative procedure may be used to obtain a rapidly converging solution the nonlinear equations. However, the memory of the computer is heavily taxed for the large data sets due to the large number of matrix elements involved. Other matrix have proven impractical for the same reason. Incidentally, one of the major problems with the maximum entropy methods (MEM) is the large number of matrix elements required for the larger data sets. The methods of solution for these equations that have proved most successful with present computers are the various relaxation schemes such as the point successive and point simultaneous methods of successive substitutions.

The point successive method of successive substitution was adopted by the author in earlier work<sup>1</sup> as the equations almost always converged and converged more rapidly than the point simultaneous method. However, the excessive amount of cpu time needed for computing the larger data sets motivated the search for faster methods.

The point simultaneous methods are being explored in the current research being done at AFGL because of important advantages found to have been possessed by them. One of the most important of these is that the fast Fourier transform (FFT) computational algorithm may be used to calculate the summed sinusoidal products in the equations and, of course, to perform them much faster than may be computed directly. Another important advantage discovered during the course of the research here was that there are approximations that may be employed to considerably reduce the overall number of calculations performed<sup>2</sup>.

A first approximation may be obtained by assuming initial values of zero for all the unknowns in the equations except the one whose coefficient is the sum over the squared sinusoid, which makes this coefficient the largest one. The remaining term in each equation is easily seen to be a component of the discrete Fourier transform (DFT) of the negative values of the discrete function ( this discrete function given by Fourier transforming the interferogram). Thus, the approximations to the unknowns may be expressed very simply by factors (which are not constant, but vary with each unknown) multiplying the FFT of the negative values given on an iteration. A reasonable approximation to the interferogram is usually produced by this operation and convergence is brought about for many data.

For more recalcitrant data, however, better approximations are needed. A second step was added to this approximation by substituting the unknowns approximated by the above procedure back into the equations in place of those unknowns previously assumed to be zero. This brought about almost complete convergence for all data considered. However, a very important discovery made in the course of this work was that not all of the terms are needed to produce convergence. Only a subset may be needed. The subset consisting of the largest values of the terms seemed to be most effective in inducing convergence. Yet total cpu time was not reduced when choosing the largest values directly. This is because the decision-making capabilities of the computer, such as expressed by FORTRAN "IF" statements, require more cpu time than do multiplications and other arithmetic operations. These subsets must necessarily be chosen by less direct means. Much time and effort has been expended in this research in exploring and testing the various ways of choosing these subsets from the total number of terms in the nonlinear equations. This work is still ongoing.

To summarize the progress at this point, the new method based on the point simultaneous solution to the equations reduces computer memory requirements to approximately half of that needed by the earlier method used by the author, and reduces cpu time to about one fifth of that of the earlier method, for reasonably accurate restorations from the experimental data.

For future development, user interaction should be minimized such that the average technician could run the computer programs and get reasonably good results. At present, much user interaction is needed to obtain an adequate restoration. Present techniques should be generalized and further developed to promote the smooth processing of increasingly larger data sets, for both one and two dimensions. Also, various other parameters and weights for the subsets and other terms are being adjusted within the algorithm in efforts to find the combination that results in the most complete convergence with the least cpu time. There still exists a problem with obtaining complete convergence with the experimental data when using the approximations. This needs to be addressed and worked out.

The data employed in this research were synthetic infrared OH and CO<sub>2</sub> spectra and experimental data of 16384 points in the near-infrared spectral range taken with a rocketborne field-widened interferometer.

1. S. J. Howard, J. Opt. Soc. Am. 71, 819 (1981).
2. S. J. Howard, Appl. Opt. 25, 1670 (1986).

Samuel J. Howard, Ph.D.

Samuel J. Howard, Ph.D.  
29 Aug. 1986

1985-1986 AFGL-SCEEE GEOPHYSICAL SCHOLAR PROGRAM

Sponsored by the

AIR FORCE GEOPHYSICS LABORATORY

Conducted by the

SOUTHEASTERN CENTER FOR ELECTRICAL ENGINEERING EDUCATION

FINAL REPORT

ON THE TECTONIC SIGNIFICANCE OF THE "DELAYED AFTERSHOCK"  
SEQUENCE ASSOCIATED WITH THE 1977 SUMBA EARTHQUAKE

Prepared By: Robert McCaffrey

Research Location: Air Force Geophysics Laboratory

Date: August 31, 1986

Preface

This final report to the Air Force Geophysics Scholar Program covers the period March 1, 1986 to August 31, 1986. It consists of two manuscripts that will be published in geophysics journals, pending clearance by AFGL and review by the journals editors.

ON THE TECTONIC SIGNIFICANCE OF THE "DELAYED AFTERSHOCK" SEQUENCE  
ASSOCIATED WITH THE 1977 SUMBA EARTHQUAKE

Robert McCaffrey

Air Force Geophysics Laboratory, Hanscom AFB, Bedford MA 01731  
and Department of Earth, Atmospheric, and Planetary Sciences,  
MIT, Cambridge, MA 02139

Abstract The "delayed aftershock" sequence of strike-slip earthquakes following the great Sumba earthquake of August 1977 at the Java trench is shown to have occurred within the overriding plate and to be similar in depth and source mechanism to several other large earthquakes in the region between 1968 and 1983. Historically, strike-slip earthquakes are the most energetic expression of plate convergence as underthrust events in the Sumba region are rare and relatively small. The October 1977 aftershock events are consistent with this pattern and thus a direct causal relationship between the mainshock and these strike-slip aftershocks is not indicated.

#### Introduction

The Sumba earthquake of 19 August 1977, with a seismic moment of approximately  $10^{21}$  Nm and a normal-fault mechanism, indicates that some modification of the subduction process is occurring at the Java trench (Cardwell et al., 1981, Hanks, 1979), but debate continues on whether this earthquake ruptured only the upper part of the lithosphere as a plate-bending event (Silver and Jordan, 1983, Silver et al., 1986) or ruptured its entire thickness (Given and Fanamori, 1980, Lynnes et al., 1985, Spence, 1986, Stewart, 1978). The August earthquake and its many aftershocks were followed by a "delayed aftershock" sequence, a group of earthquakes that occurred

approximately 200 km NW of and starting about 50 days (in early October, 1977) after the mainshock (with a combined total seismic moment of approximately  $10^{19}$  Nm). In contrast to the earthquakes beneath the trench, that had E-W striking normal-fault mechanisms and N-trending T axes, the October sequence had strike-slip fault plane solutions with N-trending P axes (Dziewonski et al., 1981; Fitch et al., 1981; Spence, 1986). Both direct (Spence, 1986) and indirect (Dziewonski et al., 1981; Fitch et al., 1981) relationships between the mainshock and the "delayed aftershocks" have been inferred.

The October "aftershock" sequence provides a rare opportunity to study the response of the lithosphere to a large earthquake, and, in this respect, a fundamental question is whether the earthquakes occurred within the upper or lower plate. Because these earthquakes occurred beneath the forearc where the top of the subducting plate is still less than 70 km deep and because the hypocentral depths reported by the International Seismological Centre (ISC) for this region can have uncertainties of several tens of kms (McCaffrey, 1986), this is not a trivial task. In a recent study, Spence (1986) constrained focal depths by picking pP-P times and relocated the events by the method of joint hypocenter determination. Using the relocated depths and a linear extrapolation of the top of the subducting plate starting at the trench, he inferred that the October earthquakes occurred within the subducting plate.

A source in the downgoing plate leads to the problem of explaining how the maximum deviatoric stress, originally tensile along the plate's dip direction, becomes compressional in the same direction. The explanation offered by Spence (1986) is that the large event at the trench caused an overshooting of the plate's equilibrium position and generated a strain pulse that propagated down the slab. If the Sumba earthquake did indeed relieve all tensile stress in the

slab, then its stress drop provides an upper bound on the magnitude of the ambient deviatoric stress in the subducting plate. It is notable in this regard that several workers (Fitch et al., 1981; Hanks, 1979; Silver and Jordan, 1983) have remarked that the Sumba earthquake may have had one of the largest stress drops calculated for a large earthquake, on the order of several hundred bars.

The purpose of this paper is to present evidence that the October strike-slip earthquake series occurred within the overriding plate and that it merely reflects the normal response of the upper plate to convergence in this region. The fault plane solutions and depths of the October 1977 earthquakes were similar to those of several large earthquakes in the region between 1968 and 1983 (Figure 1), whose combined seismic moment was approximately  $3 \times 10^{19}$  Nm. In particular, the largest of the October 1977 earthquakes is shown here to be similar in mechanism to, but smaller in seismic moment than one on 26 January 1968, an event not directly related to a normal-fault earthquake. Likewise, the other strike-slip earthquakes were not associated with large normal-fault earthquakes at the Java trench, nor did they occur within the subducting plate. While it is possible that the 1977 Sumba earthquake to some degree triggered the strike-slip earthquakes, in my view such faulting is caused by plate convergence and would occur eventually through normal strain accumulation. Thus a direct causal relationship between the normal-fault event and the "delayed aftershock" zone is not required. More importantly, the scenario, and its implications, proposed by Spence (1986), in which the great Sumba earthquake caused the previously stretched slab to go into downdip compression, is unsupported.

Earthquake of 7 October 1977 (12h10m) This earthquake accounted for nearly half of the seismic energy released during the strike-slip earthquakes in October 1977 (Dziewonski *et al.*, 1981). Vertical component, long-period P waves are shown in Figure 2 along with synthetic seismograms for centroid depths of 12 and 22 km below sea level. The source depth, strike, dip, rake, source time function, and seismic moment were determined by least-squares inversion of the amplitudes of the observed seismograms (Nabelek, 1984; McCaffrey, 1986). The synthetic seismograms were generated using a source structure constrained by a nearby seismic refraction profile (profile MSN 18 (Curray *et al.*, 1977), 200 km west of the October earthquakes) (Table 1).

The solution at 12 km depth (Figure 2a; Table 2) fits the data much better than that at 22 km (Figure 2b) both visually and statistically; the difference in variance for the two solutions is greater than a factor of 2. Using waveforms, Fitch *et al.* (1981) determined depths of 12 km (below the sea floor) both for this event and for the second largest event (16 October, 21h09m) in the sequence, and also found depths of 10 and 11 km for two other events by relative relocations. Adding the water depth ( $\approx 4$  km) to these values, the depths below sea level are 14 to 16 km.

Depth of the Plate Interface Thrust earthquakes with shallow, N-dipping nodal planes near Sumba Island, 150 km directly to the east of the October 1977 earthquakes, fall between 24 and 30 km depth (Figure 1). These events mark the thrust interface between the Indian Ocean and SE Asian plates. Chamalaun *et al.* (1982) infer that the thickness of the crust north of Sumba is approximately 24 km, based on preliminary analysis of a seismic refraction profile. The plate interface near Sumba must be at least this deep. Similarly, the Moho beneath refraction line MSN-18 (Table 1) is at approximately 19 km depth and, because sediments in the Lombok Basin are undeformed, the structure

revealed by MSN-18 is probably that of the upper plate. Therefore, the 1977 strike-slip event, being well above this interface, was certainly in the upper plate. I also point out that all of the events relocated by Spence (1986; his Figure 3) whose largest semimajor axis of the confidence ellipse is less than 10 km, are in the depth range of 14 to 22 km; i.e., also within the upper plate.

Earthquake of 26 January 1968 One of the arguments for a causal relationship between the great Sumba earthquake and the strike-slip aftershocks is the apparent historical quiescence of the region in which the aftershocks occurred (Dziewonski *et al.*, 1981; Fitch *et al.*, 1981). A major point of this paper, however, is that strike-slip earthquakes are common along the eastern Sunda arc and are explainable in terms of the regions tectonic development. Elsewhere (McCaffrey, 1986), I showed that strike-slip earthquakes are predominant in producing shortening within the forearc and interpreted this as a direct consequence of collision with the Australian continent. The best example of a strike-slip earthquake within the upper plate is the 26 January 1968 ( $m_b$ -6.0) earthquake, one of the 5 largest shallow events ( $M_o > 10^{19}$  Nm) to have occurred along the eastern Sunda arc in the past 25 years. According to ISC reports, it was preceded by a few hours by one  $m_b$ -5.0 foreshock and was followed by few aftershocks (only 7 earthquakes are reported in the following year within 100 km of this event). Fitch (1972) determined a strike-slip solution for this earthquake from P wave first-motions. Here I use the long-period P and SH waves from this event to constrain its source depth and seismic moment and to refine its fault plane solution.

A direct comparison of long-period P waves for the 1977 and 1968 earthquakes (Figure 3a) reveals great similarity in waveforms, implying similarity in

depths and source mechanisms. The pulses are broader for the 1968 event, most likely because of a greater source duration, but in most cases they correlate with similar pulses in the 1977 seismograms. The pulses for the 1968 event are delayed in time with respect to their counterparts in the 1977 seismograms, indicating a deeper source and/or a longer source duration. Note that several of the seismograms, particularly at ANP, MAT, NAI, and CHG, display a few cycles of high amplitude energy after the first cycle of the P wave. These arrivals probably originate from source structure because they appear at several stations and in both events, and appear to have the same apparent velocity as the P waves. Some differences in the seismograms are due to a difference in orientation of the fault plane solution; for example, SBA displays a dilatational first-motion for the 1977 but is nodal for the 1968 event and CHG is nodal for the 1977 but compressional for the 1968 event.

Seismograms and the best-fitting source mechanism for the 1968 earthquake (Table 2) are shown in Figure 3b; this solution is similar to that determined by Fitch (1972). The 1968 earthquake is similar in centroid depth (16 ± 4 km) to the October 1977 event (Table 2) and has a seismic moment ( $1.27 \pm 0.31 \times 10^{19}$  Nm) that is greater than or equal to that of the entire sequence of strike-slip earthquakes in 1977 (Dziewonski et al., 1981).

The 1968 earthquake occurred between Sumba and Flores Islands, very close to the line of active volcanoes (Figure 1). Because the slab here is probably nearly 100 km deep, there can be no doubt that this earthquake occurred in the upper plate. The large normal-fault earthquake at the Java trench that was closest in time and space to the 1968 event was 11 months earlier but 600 km to the WSW (30 March 1967; 11.1°S, 115.5°E;  $M_w = 7.5$ ; Fitch, 1972). Thus it is unlikely that the 1968 strike-slip earthquake was caused by a normal-fault event at the trench.

Other Strike-slip Earthquakes Strike-slip faulting within the upper plate is typical of the style of deformation for this part of the Sunda arc, evident in both large earthquakes (Figure 1) and in observed lineations in morphology (Silver et al., 1983). In addition to the 1968 earthquake, several other large shallow earthquakes between 1968 and 1983 (Figure 1 and Table 3) had fault plane solutions similar to those of the October 1977 sequence. The earthquake south of eastern Sumbawa (11 March 1982) had a seismic moment similar to that of the largest of the October 1977 events. These other strike-slip earthquakes were not associated with anomalously large slab events. Note in Table 3 that the combined seismic moment of the strike-slip earthquakes is several times that of the underthrust earthquakes.

The presence of strike-slip earthquakes beneath the forearc north of the Timor trough, where there have been no normal-fault events, indicates a lack of spatial correlation between normal-fault earthquakes at the trench and strike-slip earthquakes in the forearc. Thus the presence of a normal-fault event at the trench is not a necessary condition for strike-slip events to occur.

#### Interpretation of the October Earthquake Sequence

The October 1977 sequence of strike-slip earthquakes is shown here to have occurred in the upper plate. It was probably triggered by the large normal-fault earthquake at the Java trench; nevertheless the earthquakes are a direct consequence of plate convergence in the region.

In Figure 4 the geometry of the plate interface is shown and superimposed on it are the positions of the August normal-fault event at the trench and the October strike-slip events. The bathymetric profile is taken from the map of

Hamilton (1979) along 118°E and the slab is shown dipping northward beneath the forearc at an angle of 7°, the dip angle of the top of the plate observed at the trench. At this constant angle, the top of the slab reaches 24 km beneath the epicentral region of the October earthquake sequence. This depth probably represents a minimum for the plate interface as discussed above. Furthermore, because both slab geometry and lithospheric bending models indicate that the dip of subducting plates increase arcward, the linear extrapolation used in Figure 4 will also cause an under-estimation of the depth of the plate interface. Nevertheless, even this minimum depth is deeper than the source depths of the largest of the October 1977 earthquakes (Figure 2) and of the other large aftershocks (Fitch *et al.*, 1981).

There is little doubt that the Indian Ocean and SE Asian plates are converging and therefore that the large normal-fault event at the Java trench represents deformation within the Indian Ocean plate. If slip occurred along a 45° dipping surface (Given and Kanamori, 1980), then it consisted of nearly equal amounts of horizontal and vertical slip. However, because it was an intraplate event, it is unlikely that the August earthquake accommodated any net motion between the Indian Ocean plate (south of the Java trench) and the SE Asian plate (north of the trench). Thus points A and B in Figure 4 remained fixed relative to each other. Furthermore, as Spence (1986) points out, there is no evidence that a thrust fault was activated during or after the August earthquake sequence, an observation he uses to infer that the entire Indian Ocean plate is under horizontal tensile deviatoric stress. This lack of a thrust fault also means that the interplate thrust zone (Figure 4) was inactive throughout the normal-fault episode. However, because the normal fault produced divergence between points A and C, there was convergence across the part of the subducting slab downdip from the normal-fault

9

earthquake (point C) and the island arc (point B) that must be taken up by strain within the upper plate. The sense of this strain is the same as that caused by long-term plate convergence in the region (between points A and B) that normally manifests itself by strike-slip faults.

Triggering of normal-fault earthquakes at trenches by large underthrusting earthquakes has been observed; for instance, the 1965 Rat Island and 1960 Chile events (Stauder, 1968; 1973). It is reasonable to expect reciprocity in this process; that normal-fault earthquakes at the trench could trigger underthrusting events. Because the seismotectonic history of the Sunda arc shows that convergence proceeds predominantly by strike-slip faults, rather than by underthrusting, it is understandable that the great Sumba earthquake would cause strike-slip within the upper plate rather than interplate thrusting. The important point is that within the framework of our understanding of the tectonics of the Sunda arc collision zone, the October 1977 strike-slip earthquakes are explained in a simple and consistent manner

### Figure Captions

1. Lower hemisphere plots of fault plane solutions for earthquakes along the eastern Sunda arc. Compressional quadrants are stippled and the small numbers beside the focal spheres are the centroid depths in kilometers. Volcanoes are designated by filled triangles and thrust faults are shown with the barbs on the upper plate. The plot shows only earthquakes in the upper 40 km. The 1968 and 1977 earthquakes discussed here are labeled and designated by larger focal spheres. The smallest focal spheres show Harvard CMT solutions (the one at 23 km near the Java Trench represents the great Sumba earthquake of 19 August 1977) and the intermediate sized spheres are from McCaffrey (1986).

2. Observed long-period P wave seismograms (solid lines) for the largest of the October aftershocks and synthetic seismograms (dashed lines) calculated at centroid depths of 12 and 22 km below sea level. Calculated source time functions are shown on the time axes. Amplitudes (scale at right) of both observed and calculated seismograms are normalized to a common instrument magnification (>300) and epicentral distance (>40°). Source structure is given in Table 1. The small vertical tick marks on the seismograms enclose the part that was used in the inversion.

3. a. Observed long-period P wave seismograms for the 1968 and 1977 earthquakes. The number beside the station code is the ratio of plotted amplitudes (1968 over 1977) and the numbers following the seismograms are the averages of the epicentral distances and azimuths from the two earthquakes to the stations. Seismograms are aligned at their predicted arrival times. Note the similarity of the waveforms and the strong correlation between later, large amplitude arrivals. b. Seismograms and best fitting fault plane

solution for the 1968 earthquake. The format is the same as in Figure 2.

4. Preferred interpretation of the October earthquake sequence in relation to the great normal-fault event at the Java Trench. Vertical exaggeration is x2.

## References

Cardwell, R.K., E.S. Kappel, M.S. Lawrence, and B.L. Isacks (1981). Plate convergence along the Indonesian arc. *Eos Trans. AGU*, 62, 404.

Chamalaun, F.H., A.E. Grady, C.C. von der Borch, and H.M.S. Hartono (1982). Banda Arc tectonics: The significance of the Sumba Island (Indonesia) in Studies in Continental Margin Geology, edited by JS Watkins and CL Drake, *Am. Assoc. Pet. Geol. Memoir* 34.

Curray, J.R., G.G. Shor, R.W. Raith and M. Henry (1977). Seismic refraction and reflection studies of crustal structure of the eastern Sunda and western Banda arcs, *J. Geophys. Res.*, 82, 2479.

Dziewonski, A.M., T.-A. Chou, and J.H. Woodhouse (1981). Determination of earthquake source parameters from waveform data for studies of global and regional seismicity, *J. Geophys. Res.*, 86, 2825-2852.

Dziewonski, A.M., A. Friedman, D. Giardini, and J.H. Woodhouse (1983). Global seismicity of 1982: centroid-moment tensor solutions for 308 earthquakes, *Phys. Earth Planet. Int.*, 33, 76-90.

Fitch, T.J. (1972). Plate convergence, transcurrent faults and internal deformation adjacent to southeast Asia and the western Pacific, *J. Geophys. Res.*, 77, 4432-4460.

Fitch, T.J., R.G. North, and M.W. Shields (1981). Focal depths and moment tensor representations of shallow earthquakes associated with the great Sumba earthquake, *J. Geophys. Res.*, 86, 9357-9374.

Given, J.W., and H. Kanamori (1980). The depth extent of the 1977 Sumbawa, Indonesia earthquake, *Eos Trans. AGU*, 61, 1044.

Hamilton, W. (1979). Tectonics of the Indonesian region, *U.S. Geol. Surv. Prof. Paper* 1078, 345 pp.

Hanks, T. (1979). Deviatoric stresses and earthquake occurrence at the outer rise. *J. Geophys. Res.*, 84, 2363-2368.

Lynnes, C.S., T. Lay, and L.J. Ruff (1985). Rupture process of the 1977 Sumba earthquake. *Eos Trans. AGU*, 66, 957.

Nabelek, J. (1984). Determination of earthquake source parameters from inversion of body waves. Ph.D. thesis, Mass. Inst. of Tech.

Silver, P.G., D.R. Reed, R. McCaffrey, and Y.S. Joyodiwiryo (1983). Backarc thrusting in the eastern Sunda arc, Indonesia: a consequence of arc-continent collision. *J. Geophys. Res.*, 88, 7429-7448.

Silver, P.G., M.A. Riedesel, T.H. Jordan, and A.F. Sheehan (1986). Low frequency properties of the Sumbawa earthquake of 1977. *Eos Trans. AGU*, 67, 309.

Silver, P.G., and T.H. Jordan (1983). Total-moment spectra of fourteen large earthquakes. *J. Geophys. Res.*, 88, 3273-3293.

Spence, W. (1986). The 1977 Sumba earthquake series: Evidence for slab pull force acting at a subduction zone. *J. Geophys. Res.*, 91, 7225-7239.

Stewart, G.S. (1978). Implications for plate tectonics of the August 19, 1977 Indonesian decoupling normal fault earthquake. *Eos Trans. AGU*, 59, 326.

Stauder, W. (1968). Mechanism of the Rat Island earthquake sequence of February 4, 1965, with relation to island arcs and sea-floor spreading. *J. Geophys. Res.*, 73, 3847-3858.

Stauder, W. (1973). Mechanism and spatial distribution of Chilean earthquakes with relation to subduction of the oceanic plate. *J. Geophys. Res.*, 78, 5033-5061.

TABLE 1 Observed and assumed velocity structures

Results of MSN 18 at 10° 2'S 115° 3'E (Murray et al. 1977)

Thickness (km)	vp (km/s)
4.1	1.5
2.6	2.1
2.4	4.8
9.1	6.2
—	8.4

## Structure used for generation of synthetic seismograms

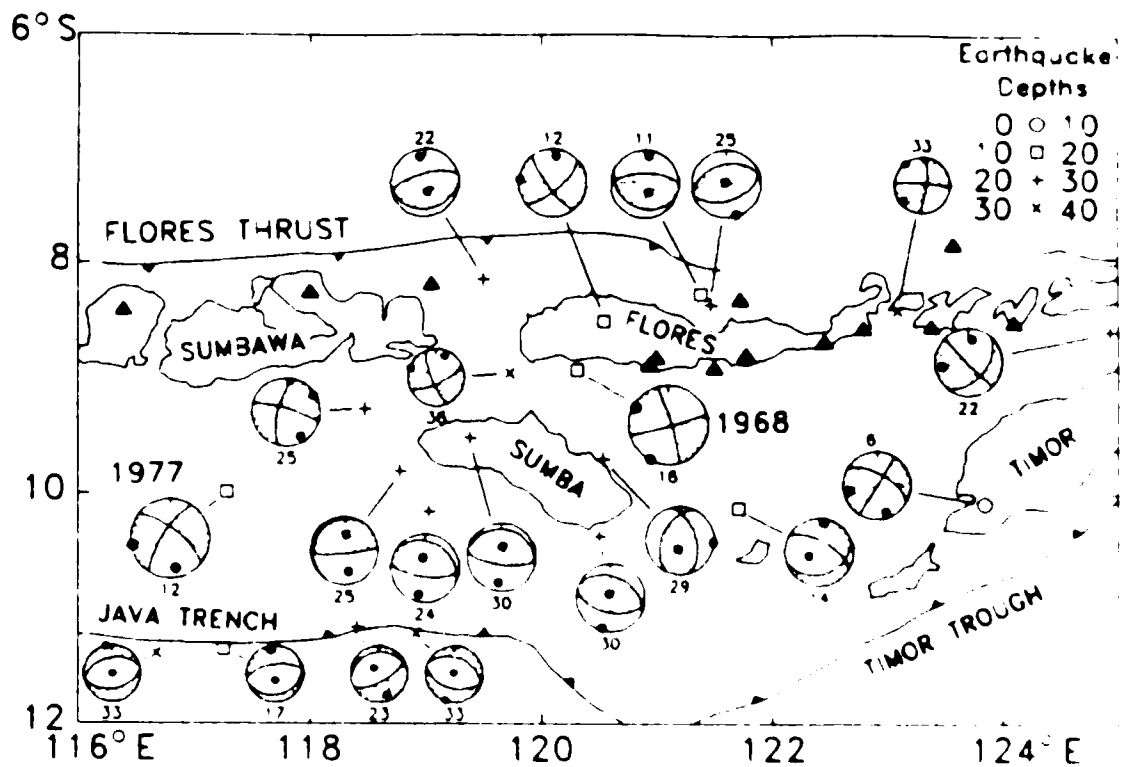
	Thickness (km)	vp (km/s)	vs (km/s)	Density (kg/m <sup>3</sup> )
1968 Earthquake	0.3	1.5	0.0	1030
	halfspace	6.2	3.5	2800
1977 Earthquake	4.3	1.5	0.0	1030
	5.0	2.9	1.6	2300
	9.0	6.2	3.5	2800
	halfspace	8.0	4.6	3300

## TABLE 1. Data for fault plane solutions of earthquakes

Date	Time	Lat	Long	Depth	Mo	Dur	Plane 1		Plane 2		P-axis		T-axis	
							Str	Dip	Str	Dip	Tr	Pl	Tr	Pl
							°S	°E	km	$10^{10}$ Nm	s	°	°	°
1968-08-28	1968 08 28 0445	8 93	120 32	16	12 7	20	343	83	74	86	208	2	299	8
1977-10-11	1977 10 11 0010	9 99	117 29	12	5 5	5	309	71	213	74	170	25	261	2

TABLE 3. Depths and seismic moments of strike-slip and underthrust earthquakes from the eastern Sunda arc.

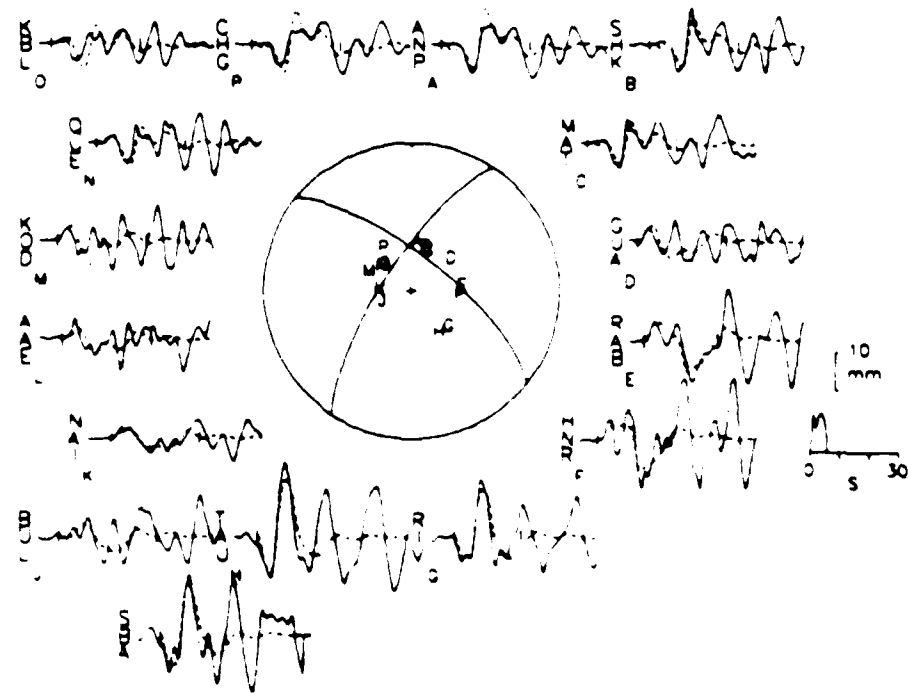
	Date	$M_o$	Depth	Reference
		$10^{16}$ Nm	(km)	
Strike-slip	26 Jan. 1968	1270	16	this paper
	18 Oct. 1972	80	22	McCaffrey (1986)
	30 July 1975	100	6	McCaffrey (1986)
	7-16 Oct. 1977	1000	12-16	Dziewonski et al. (1981)
	11 Mar. 1982	370	25	McCaffrey (1986)
	6 Aug. 1982	50	12	McCaffrey (1986)
	25 Dec. 1982	97	40	Dziewonski et al. (1983)
	18 Dec. 1983	64	36	Harvard CMT
Underthrust near Sumba	17 Oct. 1972	100	30	McCaffrey (1986)
	19 Dec. 1973	170	30	McCaffrey (1986)
	2 Jan. 1977	210	24	McCaffrey (1986)
	4 Oct. 1984	180	25	McCaffrey (1986)



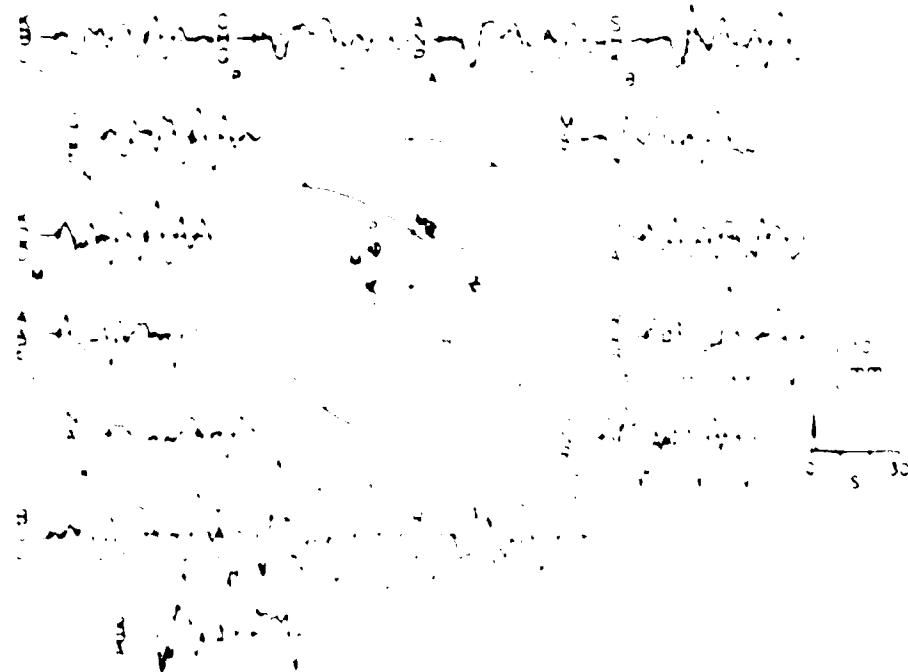
7 October 1977 (12h10m)

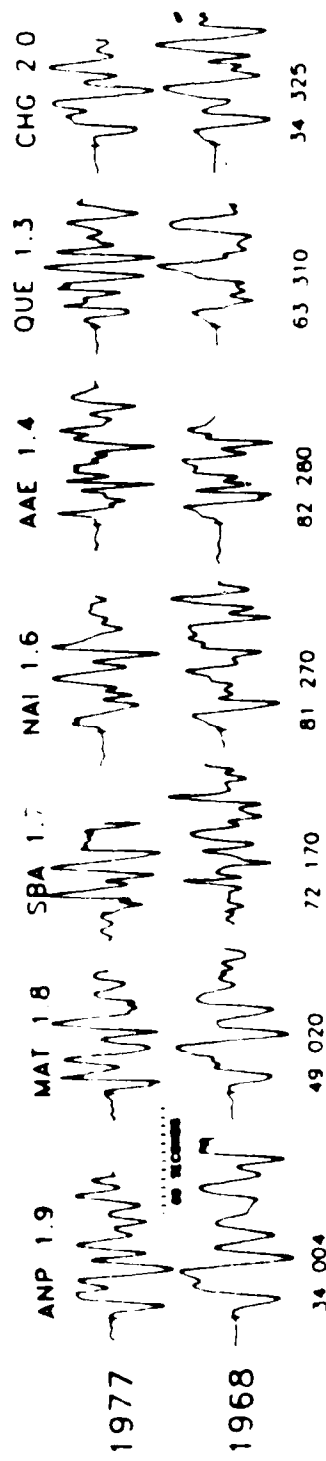
P Waves

Depth = 12 km



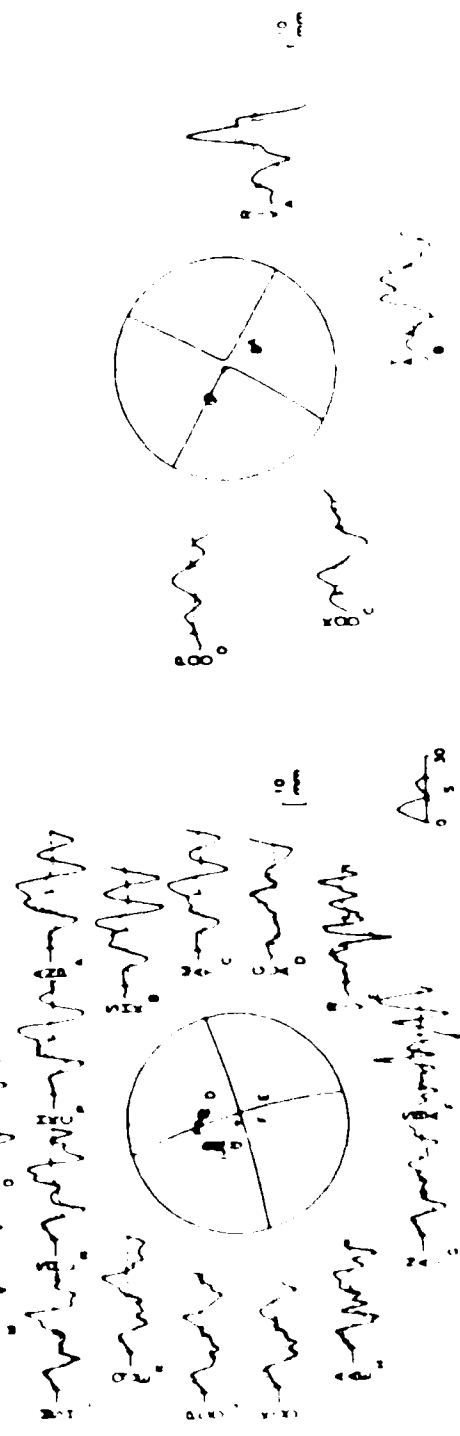
Depth = 22 km





26 January 1968

P Waves SH Waves



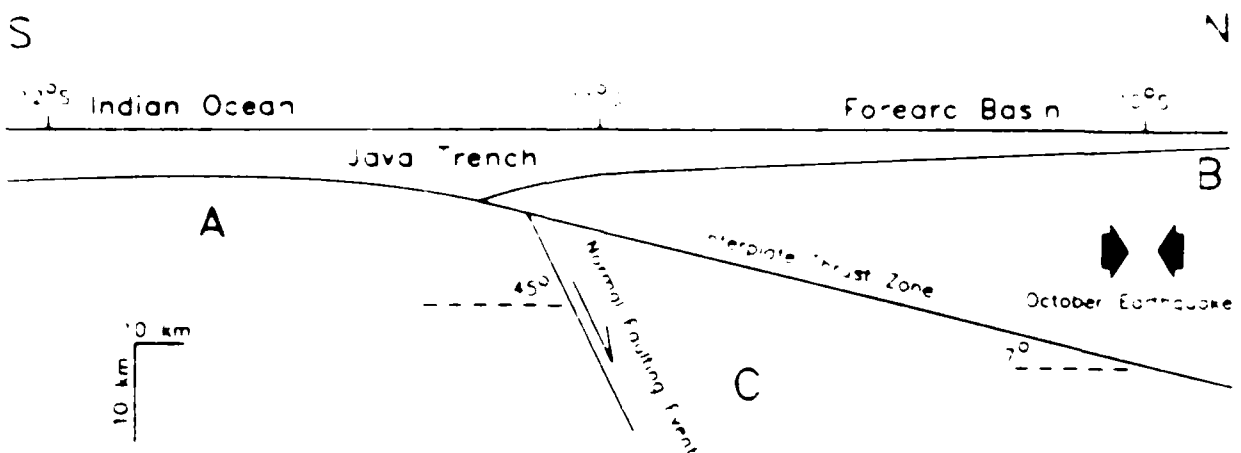


FIGURE 4

EARTHQUAKES, GRAVITY, AND THE ORIGIN OF THE BALI BASIN: AN EXAMPLE OF A  
NASCENT CONTINENTAL FOLD-AND-THRUST BELT

Robert McCaffrey<sup>1</sup> and John Nabelek<sup>2</sup>

Department of Earth, Atmospheric and Planetary Sciences  
Massachusetts Institute of Technology  
Cambridge, MA 02139

---

<sup>1</sup> Now also at Air Force Geophysics Laboratory, Hanscom AFB

<sup>2</sup> Now at Lamont-Doherty Geological Observatory

**Abstract.** We infer from the bathymetry and gravity field and from the source mechanisms and depths of the eight largest earthquakes in the Bali region that the Bali Basin is a downwarp in the crust of the Sunda Shelf produced and maintained by shallow thrusting along the Flores backarc zone. Earthquake source mechanisms and focal depths are inferred from the inversion of long-period P and SH waves and from short period seismicity of the events. Centroidal depths that give the best fits to the data range from 10 to 18 km but uncertainties in depth are 1 to 2 km. The P-wave nodal planes that dip south are generally roughly parallel to the volcanic arc and are consistent with the shallow Bali Basin beneath it. The positions of the shallow seismic crustal features inferred from the eight largest earthquakes occur in the basin.

RD-R180 197

USAF/SCEE (SOUTHERN CENTER FOR ELECTRICAL  
ENGINEERING EDUCATION) AIR. (U) SOUTHERN CENTER FOR  
ELECTRICAL ENGINEERING EDUCATION INC S. W D PEELE

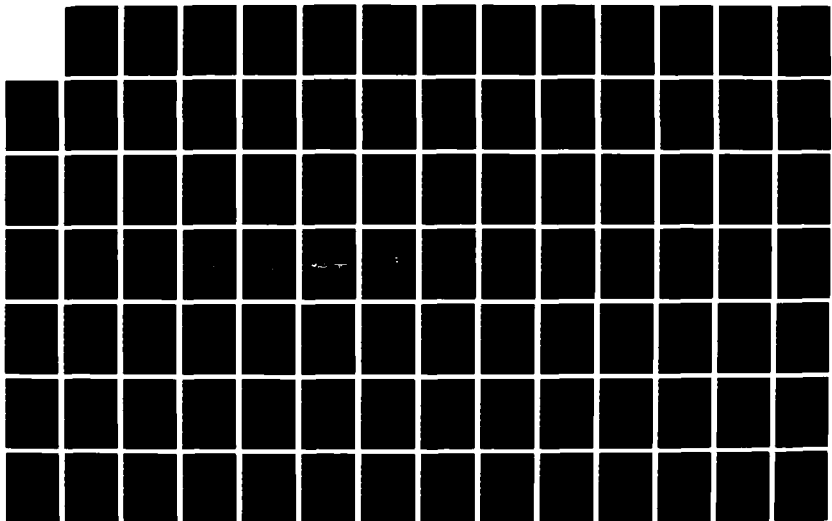
2/2

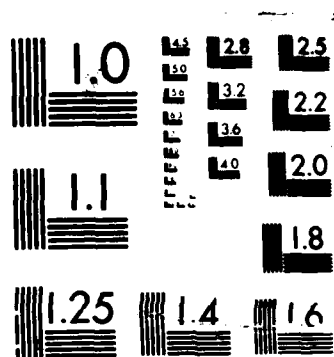
UNCLASSIFIED

NOV 86 AFGL-TR-87-0038 F19628-83-C-0097

F/G 7/4

ML





MICROCOPY RESOLUTION TEST CHART  
NATIONAL BUREAU OF STANDARDS 1964A

zone. Summation of seismic moments of earthquakes between 1960 and 1985 suggests a minimum rate of convergence across the thrust zone of  $4 \pm 2$  mm/a. The slip direction for the backarc thrust zone inferred from the orientation of the earthquake slip vectors indicates that the thrusting in the Bali Basin is probably part of the overall plate convergence as it roughly coincides with the convergence direction between the Sunda arc and the Indian Ocean plate. The presence of backarc thrusting suggests that some coupling between the Indian Ocean plate and the Sunda arc occurs but mechanisms such as continental collision or a shallow subduction of the Indian Ocean plate probably can be ruled out. The present tectonic setting and structure of the Bali Basin is comparable to the early forelands of the Andes or western North America in that a fold-and-thrust belt is forming on the continental side of an arc-trench system at which oceanic lithosphere is being subducted. The Bali Basin is flanked by the Tertiary Java Basin to the west and the oceanic Flores Basin to the east and thus provides an actualistic setting for the development of a fold-and-thrust belt in which structure and timing of deformation can change significantly along strike on the scale a few hundred kilometers.

### Introduction

The questions of how and under what conditions fold-and-thrust belts develop in the forelands of continental arcs have been approached largely by studies of well developed examples such as the Andes and western North America. In both examples, however, the along strike variations in the style of deformation are so great that general cause-and-effect relationships are difficult to infer. Moreover, in only one of the cases (the Andes) do we have first-hand knowledge of the dip angle of the subducting plate so that

inferences about the role of the underthrusting plate in driving the deformation in both examples remain equivocal. Accordingly, studies of other regions where backarc thrusting now occurs are crucial.

One of the clearest examples of present day backarc thrusting that spans both oceanic and continental settings is the long thrust zone north of the Sunda arc between Java and Wetar [Hamilton, 1979; McCaffrey and Nabelek, 1984, 1986; Silver et al., 1983, 1986a,b; Usna et al., 1979] (Fig. 1). The thrust zone is evident in two segments: the Flores thrust zone in the west and the Wetar thrust zone in the east. Both dip opposite to the sense of subduction of the Indian Ocean - Australia plate at the Java Trench and Timor Trough. The Flores thrust zone is the longer and more developed of the two and extends westward, disappearing beneath the Bali Basin [Silver et al., 1983]. Both thrust zones have gravity anomalies, accretionary prisms [Silver et al., 1983], and thrust earthquakes [McCaffrey and Nabelek, 1984, 1986] associated with them. So far, earthquakes studied that are clearly associated with the backarc thrust zone are shallower than 25 km [McCaffrey, 1986].

In this paper we focus on the western section of the Flores thrust zone west of Sumbawa and extending into the Bali Basin. Here, the volcanic arc is built on the thick crust of the southern edge of the Asian margin (Sunda Shelf) and thus forms a continental arc, or what is commonly called an "Andean" margin. The Flores thrust zone in this region accommodates the thrusting of the Sunda Shelf in the backarc beneath the volcanic arc and thus is analogous to intracontinental thrust zones such as those today east of the Andes and in western North America in the Cenozoic. To the east the Flores and Wetar backarc thrust zones involve oceanic crust of the Flores Basin and Banda Sea. We examine the depths and mechanisms of the eight largest earthquakes from the Bali Basin by inverting their long-period P and SH waves and, in some cases,

short-period P waves. In addition, we compile gravity and bathymetry data and present maps for the Bali Basin. We then discuss the constraints these data place on the structure and evolution of the Bali Basin and the causes of backarc thrusting, and discuss the implications for the early evolution of fold-and-thrust belts.

### The Bali Basin

Setting The Bali Basin is a narrow, easterly-elongated basin in the southeastern part of the Sunda Shelf, with water depth locally exceeding 1.5 km (Figs. 1 and 2). Its southern margin is formed by the active volcanic arc. Along strike to the west are the Tertiary Madura and Java sedimentary basins and to the east is the deeper Flores Sea, likely underlain by oceanic crust [Curray et al., 1979; McCaffrey and Nabelek, 1984].

The southeastern Sunda Shelf is covered by 1 to 2 km, and locally up to 5 km, of sediments and by an average of 200 m of water [Ben-Avraham, 1973; Ben-Avraham and Emery, 1973]. It locally emerges at the islands of Kangean and Madura in an E-W trending ridge. During most of the Pleistocene the portion of the shelf north of Java was a landmass that submerged only recently [van Bemmelen, 1949]. The easterly elongated Java Basin received sediments from both this northern landmass and the volcanic arc to the south [van Bemmelen, 1949; Weeda, 1958]. The eastern Java Basin is now approximately 150 km wide and filled with up to 6 km of Tertiary sediments; the lowest 4 km consist of deep water facies, while the upper 2 km show the transition to the present land conditions [Weeda, 1958]. We know of no direct measure of the thickness of sediments in the Bali Basin, but we suggest that there may be approximately 6 km, based on gravity data and the shapes of the seismograms from the

earthquakes (discussed below).

Basement rocks of the eastern Sunda Shelf range in ages from 58 to 140 ma (K-Ar) and consist of terrigenous and volcanioclastic metasediments, and volcanic and granitic rocks [Ben-Avraham, 1973; Hamilton, 1979]. The basal sediment layer appears to be of Eocene age. The sedimentary cover is thin or absent over basement ridges that trend either NE (the Pulau Laut and Meratus Ridges) or east (the Madura-Kangean Ridge). Ben-Avraham and Emery [1973] noted that the sedimentary layers on both sides of the Pulau Laut and Meratus Ridges have the same apparent dip as the ridge flanks and do not thicken away from the ridges. This geometry indicates that the ridges formed after deposition of the strata and the truncation of these ridges and the strata at the seafloor suggests that uplift has ceased. Conversely, the thickening of the sedimentary layers away from the Madura-Kangean Ridge indicates that it has been uplifted during deposition of the sediments, and its present exposure at the two islands suggests that uplift may be continuing. Ben-Avraham and Emery [1973] interpreted the Pulau Laut, Meratus, and Madura-Kangean Ridges as the roots of anticlines formed by NW-SE and N-S compression.

The islands of Java, Bali, Lombok, and Sumbawa presumably formed by the construction of volcanic arcs on the previously passive southern margin of the Sunda Shelf [Hamilton, 1979]. Along the southern coasts of the islands is a pre-Miocene volcanic arc, while the present volcanoes are situated closer to the northern coasts. Van Bemmelen [1949] noted a NW-SE alignment of volcanic features on Bali and a tendency for younger eruptions to be more basaltic. Between Flores and Pantar, the volcanic islands are built on oceanic crust, the volcanoes lie along the southern coasts, and the earlier arc is not evident.

Crustal Structure North of Lombok, the Flores thrust zone has the appearance of a typical oceanic subduction zone in seismic reflection profiles (Line 63; Fig. 3). The thick sedimentary section south of km 30 is broadly folded and the steeper limbs of the asymmetric folds are truncated along predominantly S-dipping thrust faults. The increasing dip with depth of planar reflectors beneath km 55 indicates that sedimentation and deformation have occurred concurrently. North of the Flores thrust zone (km 0 to 20) the reflectors seem to arch down into the thrust zone. A comparison with Line 67 (Fig. 3) shows that the style of deformation changes westward and that the Flores thrust zone loses its surface expression north of Bali. Nevertheless, the broad folding continues and involves the entire sedimentary section, indicating the presence of a decollement surface at depth beneath the sediments [Silver et al., 1983]. The gravity field is not appreciably less negative, indicating that the amount of crustal thickening is similar beneath both lines. Note again the arching of the otherwise undisturbed reflectors from the north into the deeper, southern part of the basin.

Hamilton [1979] suggested that the crust of the Bali Basin was transitional in thickness between oceanic and continental, based on water depth and the assumption that it was in isostatic equilibrium. Ben-Avraham and Emery [1973] inferred that oceanic crust was present beneath the Bali and Madura Basins because of their positions on line with the Flores Basin. Based on the following evidence, we infer that the crystalline crust beneath the Bali Basin is the same thickness as beneath the Sunda Shelf, and we further surmise that the two are genetically identical. First, the arching of the sediments and of the seafloor from the north into the basin (Figs. 3 and 4) indicate that the basin subsided after deposition of the sediments. The continuation of the arching into the deepest part of the basin indicates that all of the

bathymetric relief can be explained by downbowing of the crust. Second, the minimum in the gravity field over the Bali Basin is displaced 30-40 km south of the minimum in the bathymetry, indicating that isostatic equilibrium does not hold here. More likely, the basement of the Sunda Shelf dips to the south beneath the deformed sediments in the southern Bali Basin and the deepening of the top of the basement is not accompanied by thinning of the crust. As will be shown, the magnitude of the gravity anomalies is consistent with the idea that the gravity and bathymetric lows are due to downbowing of the crust of the Sunda Shelf. Finally, the bathymetric profile along Line 22 of Ben-Avraham [1973] (Line B22; Fig. 4) displays the characteristic shape of a flexed lithospheric plate. The estimated flexural rigidity for the Sunda Shelf of  $5$  to  $10 \times 10^{22}$  Nm is typical of some oceanic [Caldwell et al., 1976] and continental [Walcott, 1970] regions and corresponds to an effective elastic thickness of 18 to 23 km (Fig. 4).

Seismicity Earthquakes associated with subduction of the Indian Ocean plate define a zone that dips northward from the Java Trench to a depth greater than 600 km beneath the Java Sea (Fig. 5). We note, however, that in this region there are few large events that might indicate thrusting of the Indian Ocean plate beneath the forearc, whereas several normal faulting events have occurred beneath the Java Trench, including the  $M_s = 8.1$  earthquake of August 1977 near  $11^\circ\text{S}$ ,  $118^\circ\text{E}$ . The concentration of hypocenters at  $10^\circ\text{S}$ ,  $117^\circ\text{E}$  is due to shallow strike-slip faulting within the overriding plate during October 1977 [Fitch et al., 1981].

The earthquakes discussed in this paper occurred at shallow depth in the overriding plate beneath the active volcanic arc between Java and Lombok, and several were very destructive. Four caused damage and deaths in the Bali region, including the  $m_b = 6.1$  event of 14 July 1976 (our event number 3) that

reportedly killed 563 people. In the same region, earthquakes in 1815 and 1917 are reported to have killed 10,253 and 15,000 people, respectively [Ganse and Nelson, 1981].

The ambient level of seismicity in the epicentral regions of the large earthquakes studied here is very low. Since all events from the ISC bulletins are plotted in Fig. 5a, note also that very few foreshocks and aftershocks with magnitudes greater than 4.5 to 5.0 were associated with these earthquakes.

#### Analysis of Earthquakes

Data The source mechanisms and depths of the earthquakes listed in Table 1 have been determined by matching observed long-period P (vertical component) and SH waves of the World-Wide Standardized Seismograph Network (WWSSN) with synthetic seismograms (Fig. 6). Each earthquake is approximated by a point source having a double-couple mechanism. The source parameters are determined by an inversion of the observed data in a least-squares sense. The estimated parameters are the strike and dip of one P-wave nodal plane, the rake angle on the plane (using the convention of Aki and Richards [1980]), the centroidal (average) depth, seismic moment, and source time function (i.e., source time history). We will refer to each solution by the strike, dip, and rake of its N-dipping P-wave nodal plane because its strike and dip angles are the better-resolved in the inversion. This plane is probably the auxiliary plane. The method used here is described by McCaffrey [1986] and is a modification of that developed by Nabelek [1984, 1985].

Only seismograms recorded at stations at epicentral distances between 30° and 90° for P waves and 30° to 60° for SH waves are used. For each of the earthquakes presented here, between 12 and 29 seismograms are used in the inversion (Table 1). Data are the amplitudes of the observed seismograms, digitized at 0.25 s intervals, within a specified time window starting at the direct phase (P or S) and extending through the reflected (pP, sP and sS) and other converted phases. Attenuation is approximated by applying a causal attenuation operator [Futterman, 1962] with a ratio of travel-time to average Q of 1s for P waves, and of 4s for SH waves. The source region crustal structure assumed in generating the seismograms consists of a water layer, sediment layer ( $v_p = 3.2 \text{ km/s}$ ,  $v_s = 1.8 \text{ km/s}$ , density  $\rho = 2300 \text{ kg/m}^3$ ), and a halfspace ( $v_p = 6.5 \text{ km/s}$ ,  $v_s = 3.7 \text{ km/s}$ ,  $\rho = 2800 \text{ kg/m}^3$ ). The P wave velocities are based on nearby seismic refraction results reported by Ben-Avraham and Emery [1973], Curray et al. [1977] and Raitt [1967]. The thicknesses of the water and sediment layer (Table 1) were adjusted to match specific characteristics of the waveforms. The response of the source structure was calculated by summing a finite number of rays [McCaffrey, 1986]. Structure at each receiver was assumed to be a half-space ( $v_p = 6.0 \text{ km/s}$ ,  $v_s = 3.4 \text{ km/s}$ ,  $\rho = 2700 \text{ kg/m}^3$ ).

Fault Plane Solutions The best-fitting fault plane solutions and the observed and calculated seismograms are shown in Fig. 6. The solutions are also plotted in both map and cross-sectional views in Fig. 7. The uncertainties in the source parameters given in Table 1 are the statistical uncertainties and underestimate the true uncertainties. An evaluation of the actual uncertainties for individual events is presented in the appendix and the general results are: depth  $\pm 5 \text{ km}$ , seismic moment  $\pm 50\%$ , strike  $\pm 20^\circ$ , dip  $\pm 5^\circ$ , and rake  $\pm 20^\circ$ . The consistency of some parameters of the best-fitting solutions among the events, however, indicates that the uncertainties might be

less than those just cited.

Events 1 and 2 occurred near the NE coast of Bali in 1963. Event 1 caused more damage on Bali although it was deeper and smaller in seismic moment than event 2. These differences imply that event 1 was located beneath the island while event 2 was offshore (Fig. 7). The N-dipping nodal plane of event 2 is constrained to lie between stations AAE, SHI, and QUE in the west and to be near GUA in the east. The similarity of the seismograms (especially from QUE that lies very close to the nodal plane) for the two events suggests very similar mechanisms. Of the events studied here, these have the shallowest S-dipping nodal planes (15° and 14°).

Events 3 and 4 occurred near the north-central coast of Bali and were separated from the other six. Again, the N-dipping nodal plane for event 3 is constrained by the northern stations; note the change in the initial P pulse in proceeding azimuthally from CHG (up) to HKC and ANP (nodal) to SHK and MAT (up). Event 4 is small and occurred in the surface wave coda of event 3. The depths of these two events estimated from the short-period P seismograms (Table 1; Fig. 8) agree to within 2 km with the depth obtained from long-period data. This agreement is compelling evidence that the long-period waveforms do have sufficient information to constrain the depths of these earthquakes to within a few km.

Events 5, 6, 7, and 8 occurred in 1979 beneath the strait separating Bali and Lombok Islands. All four were damaging and events 6, 7, and 8 caused fatalities. Note the strong similarity of waveforms among the events with the significant exception of the initial half-cycle at stations in the vicinity of the N-dipping nodal plane on the focal sphere.

For many of the events, long-period seismograms at stations near the N-dipping P-wave nodal plane display a very sharp initial pulse and a W-shaped

trough (for example, see NDI, CHG, SHK, and MAT for event 3; Figs. 6 and 9). This shape is caused by the presence of two phases with negative polarity (consistent with the expected polarity of pP; sP is expected to be positive) and a few seconds separation; the first causes the sharp turnaround of the P and the second produces the second trough of the W. Note in Fig. 9 that both the long-period and short-period records at HKC are nodal (the correlation of later phases between HKC and SHK shows that HKC has no direct P wave) and that the first pulse observed is the first of these negative-polarity phases. The wave shape at the northern stations cannot be explained by adjusting the source depth, the source time function (Fig. 9a and b), or the thickness of the water layer within limits found in the epicentral region (Fig. 9c). A typical Moho interface cannot produce the observed amplitudes.

In order to match this feature of the observed waveforms, in addition to a water layer, a thick layer with low seismic velocities comparable to those of sediments was required in the source region (Fig. 9d, e, and f). In this case, the first negative pulse is a p-wave reflection from the bottom of the sediment layer, while the second is a combination of the p-wave reflections from the tops of the sediment and the water layer. The thickness of the sediment layer must be such that it would produce the time difference between the phases, while the impedance contrast at its base must be large enough to produce the observed amplitudes. The comparison of the synthetic seismograms produced for a range of structures (with their best-fitting solutions) indicates that about 6 km of sediments are required by both the long- and short-period P waves (Fig. 9). This thickness of sediments is probably only found beneath the Bali Basin and not beneath Bali Island or Lombok Strait, where the earthquakes are located using P-wave arrival times. Thus it is likely that the earthquakes occurred more to the north than their computed

locations indicate. Similar mislocations were inferred for the 1978 earthquake on the Flores thrust zone based on waveform data [McCaffrey and Nabelek, 1984], and for several large events near Timor based on locally recorded arrival time data [McCaffrey et al., 1985].

Fault plane solutions for events 1-4 were determined from P- and S-wave first motion polarity readings in previous studies (event 2 by Fitch [1970], and events 1, 3, and 4 by Kappel [1980]). The best fitting strikes of all new solutions fall within  $10^\circ$  of  $269^\circ$  (possibly indicating a smaller uncertainty in strike than the  $20^\circ$  estimated in the Appendix) whereas those of the earlier solutions ranged from  $276$  to  $290^\circ$ . All earlier solutions were characterized by rake directions of  $90^\circ$  (i.e., pure thrust), whereas the revised solutions indicate a systematic deviation from pure thrust (all best fit rake angles are within  $9^\circ$  of  $78^\circ$ ). The horizontal projections of the slip vectors (i.e., normal to the strike of the auxiliary plane) are all within  $10^\circ$  of N. The convergence direction in the Bali Basin indicated by the slip vectors is essentially identical to the Indian Ocean - Eurasia convergence direction determined by Cardwell et al. [1981] ( $0^\circ$ ) and is similar to that predicted by Minster and Jordan [1978] ( $20^\circ$ ).

Centroid Depths The best-fitting centroid depths determined by the waveform analyses range from 10 to 18 km but the uncertainties in depths allow a range of 7 to 24 km (Appendix). These depths are generally much shallower than those reported by the ISC, including those based on "pP" readings (Table 1), and further indicate the unreliability of the ISC depths for this region [McCaffrey, 1986]. The new source depths are unequivocal evidence that these earthquakes are related to deformation of the overriding plate and not to interplate or slab activity. The long-period data do not contain enough high-frequency information to distinguish between the N-dipping and S-dipping nodal

planes as the fault plane.

Stress Drops A striking feature of the westernmost events (3 and 4) is that their source time functions are very short when compared to any of the other events of similar seismic moment and that the moment of event 3 is 10 times larger than that of event 5 which has a similar duration (Table 1). In a (single asperity) circular crack model, the stress drop is proportional to  $M_0/t^3$  (e.g., Boatwright, 1980), where  $t$  is the source duration (Table 1). Because  $M_0/t^3$  is roughly an order of magnitude higher for events 3 and 4 than for the others, it is likely that these two events had a much higher stress drop. It is unlikely that the difference is due to error, as this would require a factor of 2 error in duration or a factor of 10 error in moment.

The higher stress drop for events 3 and 4 relative to those of the eastern events denotes some change in the properties of the fault zone. The geometry of the Flores thrust zone suggests that the amount of slip that has already occurred decreases westward. It is thus possible that events 3 and 4 occurred in crust that is less fractured and perhaps stronger than that to the east. The 1978 Flores and 1977 Timor earthquakes that occurred on the more developed part of the Flores thrust zone and on the Wetar thrust zone, respectively, are also of the low stress drop type [McCaffrey and Nabelek, 1984, 1986].

Estimate of the Minimum Slip Rate To calculate the minimum slip rate for the Bali Basin we use the relation  $\Sigma u = \Sigma M_0 / \mu A$  normalized by the time period [Brune, 1968];  $u$  is the average slip for one event, the rigidity  $\mu = \rho v_s^2$  ( $3.8 \times 10^{10} \text{ N/m}^2$ ) and  $A$  is the area of the fault surface on which the earthquakes occurred. The total moment  $\Sigma M_0$  released by the eight earthquakes was  $2 \pm 1 \times 10^{19} \text{ Nm}$  (the uncertainty of 50% is based on the analysis in the Appendix). The fault length along strike is estimated at 150 km (Fig. 7a) and its downdip length at 40 km (Fig. 7b), for an area of  $6 \times 10^9 \text{ m}^2$ . The time

period is 25 years (1960-1985). From the relation above, the total slip is  $0.09 \pm 0.04$  m, and the slip rate is  $4 \pm 2$  mm/a (rounded to the nearest mm/a). By a global fit of the plates, the expected convergence rate between the Indian Ocean and Asian plates near Bali is approximately 70 mm/a [Minster and Jordan, 1978]; thus the rate of slip across the Flores thrust zone in the Bali Basin, estimated from seismic energy release, is minor compared to the expected convergence rate between the major plates. We emphasize, however, that the lack of large thrust earthquakes beneath the Sunda forearc [Kelleher and McCann, 1976] indicates that the seismic slip rate here is also very low compared to the plate motion rate and note that the concentration of thrust earthquakes along the southern margin of the backarc basin is also characteristic of the Banda arc [McCaffrey and Nabelek, 1986].

Earthquake Locations The eight earthquakes were relocated using the P-tables of Herrin [1968], P-wave arrival times from ISC Bulletins and the best-fitting depths determined from the waveform analysis (Table 1). The relocated epicenters are shifted northward by about 5 km relative to the locations determined by the ISC but retain their original pattern of grouping.

Other evidence supports the relative locations determined with arrival time data and gives some insight into the absolute locations of the events. Event 3 produced much damage in western Bali and was felt on Java. Its location beneath the island is suggested by a microearthquake study [Hayat and Panjaitan, 1983] in which shallow seismic activity beneath western Bali was recorded; however, the level of activity offshore could not be monitored. The sequence of events 5 - 8 seems to have migrated from the vicinity of Lombok towards Bali. Events 5 and 6 caused major damage on Lombok but little damage on Bali. Event 7 caused considerable damage on both islands whereas the damage caused by event 8 was concentrated on Bali. Event 8 produced maximum Modified

Mercalli intensity of IX due east of Gunung Agung (the southern volcano on Bali) at Culik (8.3°S, 115.6°E) [Effendi et al., 1981], suggesting a nearby epicenter. This constraint on the epicenter of event 8 suggests that the epicentral positions shown in Fig. 7 be shifted approximately 10 km northward. A microearthquake study southeast of Gunung Agung [Wismaya, 1981] also revealed shallow seismic activity beneath Bali Island. Finally, the requirement of a thick sediment layer in the source structure to match the waveforms coupled with the constraints on structure from the gravity data discussed below, suggests that the earthquakes were farther north, beneath the basin where sediments are more likely to be the requisite thickness.

The alignment of the relocated hypocenters in a projection onto a vertical plane that is roughly parallel to the slip direction (Fig. 7b) suggests that the S-dipping plane is the fault plane. Because of uncertainties in both the epicenters and depths, and in the appropriate projection, this independent determination of the fault plane from the earthquake positions alone must be considered somewhat inconclusive. Nevertheless, the sense of displacement on the Flores thrust zone inferred from seismic reflection profiles and gravity data suggest a S-dipping plane, and the fault plane solutions suggest that this plane dips between 10° and 30°. No significant change in dip angle with depth is apparent.

### Gravity Interpretation

Data The gravity map (Fig. 2) and Line 1 (Fig. 10a) were constructed from gravity data compiled by C.O. Bowin (see Bowin et al. [1982]) and the gravity data from the RAMA 12 cruise in 1981 [Silver et al., 1983]. All gravity measurements were reduced to their free-air anomalies with respect to the GRS 67 formula [e.g., Woppard, 1979]. The gravity values on Bali Island were reduced to simple Bouguer anomalies using the infinite sheet approximation and a density of 2700 kg/m<sup>3</sup>. Gravity and bathymetry values were averaged over 5x5 km areas and contoured at 20 mGal ( $2 \times 10^{-4}$  m/s<sup>2</sup>) intervals (Fig. 2).

In order to obtain a long profile over the Sunda Shelf, Bali Basin and the Sunda island arc, Line 1 was constructed by collecting all measurements within 30 km of a line passing southward through 6°S, 116.41°E at an azimuth of 175° and by averaging at 5-km spacings. The gravity anomalies along Lines 63 and 67 (Fig. 3) were taken from the RAMA 12 data, but were not averaged. In the following figures all profiles are referenced to the same x-axis with x=0 at 6°S.

Gravity Map (Fig. 2) The Bali Basin is associated with a low in the free-air gravity field that follows the northern coasts of the volcanic islands. The low reaches below -60 mGal north of the straits between Bali and Lombok and between Lombok and Sumbawa. The low is truncated at 115°E by a high north of western Bali. Over the Madura-Kangean Ridge there is a gravity high of 40 to 60 mGal that is likely caused by the combination of a regional high and the proximity of higher density basement rocks to the seafloor [Ben-Avraham and Emery, 1973].

The latitudinal widths of both the gravity and bathymetric lows associated with the backarc thrust zone appear to increase westward from Sumbawa (Figs. 2

and 3). We note that throughout the length of the Flores thrust zone such variations in width are common [Silver et al., 1983], but to the east the regions of greater width are usually associated with more thrusting and folding than the narrower sections. Beneath the Bali Basin, however, the zone of deformation is wide but the amount of shortening in the sediments appears to be small. The broadening of the deformed zone probably signals a change in mechanical behavior, most likely in the sediments, once the thrust zone steps onto the Sunda Shelf.

Isostatically Balanced Model of Line 1 All gravity and bathymetric lines show a strong negative in the gravity anomaly field over the deep parts of the Bali Basin and then an increase in gravity over the island arc. In order to determine whether or not the crustal structure is in isostatic equilibrium, we generated an isostatically balanced model (including the estimated effect of the subducted Indian Ocean plate) for Line 1 and compared the calculated gravity to that observed. The resulting residual (the isostatic anomaly) is a measure of the amount of non-compensation for topographic features. The isostatically balanced crustal model and its gravity effect are shown in Fig. 10a.

To generate the balanced model, we assumed that the Sunda Shelf is in isostatic equilibrium. This is a safe assumption since enormous stresses would be required to keep such a great area out of equilibrium. For the shelf, we assumed a crustal thickness of 25 km ( $\rho_c = 2800 \text{ kg/m}^3$ ). The average water depth of 0.1 km ( $\rho_w = 1000 \text{ kg/m}^3$ ) and sediment thickness of 1 km ( $\rho_s = 2300 \text{ kg/m}^3$ ) are then balanced by a mantle layer thickness of 1.9 km ( $\rho_m = 3300 \text{ kg/m}^3$ ) using the relation  $h_w(\rho_w - \rho_o) + h_s(\rho_s - \rho_o) + h_m(\rho_m - \rho_o) = 0$  where  $h$  is the thickness of the layer whose initial is in the subscript. The depth of compensation ( $H$ ) is 28 km and the average density ( $\rho_o$ ) is  $2800 \text{ kg/m}^3$ . To compensate for the

changes in water depth the crustal thickness  $h_c$  is varied locally using the relation above, and the relation  $h_c = H - h_w - h_s - h_m$ . The sedimentary layer is included in order to employ a correct density for many of the bathymetric features but, because its thickness is kept constant, its inclusion has a negligible effect on the long-wavelength part of the computed anomaly.

In addition, we assumed a density model for the subducted slab of the Indian Ocean plate (Fig. 10a). Part of the motivation to include a slab structure was to account for the regional gravity high over the Sunda Shelf [Ben-Avraham, 1973]. The position and shape of the slab are based on earthquake locations (Fig. 3). A density contrast with respect to the mantle of  $40 \text{ kg/m}^3$  was chosen to match roughly the amplitude of the field over the Sunda Shelf and to be consistent with the observable gravity effect of slabs in other parts of the world [Grow and Bowin, 1975; Molnar, 1977; Watts and Talwani, 1975]. The gravity effect of the assumed slab structure (shown by a dashed line in Fig. 10a) is about  $+35 \text{ mGal}$  over the northern end of the profile, and increases to a maximum of  $+70 \text{ mGal}$  over the island arc. Note that the inclusion of the slab as shown also implies isostatic equilibrium for the volcanic islands; they would otherwise have a strongly negative isostatic anomaly.

The residual gravity of  $\approx -100 \text{ mGal}$  for the isostatically balanced model (isostatic anomaly) indicates that the low free-air anomaly observed over the Bali Basin is not an effect of the juxtaposition of crustal elements of different thicknesses (i.e., an edge effect). We conclude that the crust beneath the Bali Basin does not thin to accommodate the increase in water depth; instead it appears to be deflected downward, and the void is filled by water and sediments.

Crustal Structure Beneath Line 67 In order to estimate how much the crust beneath the Bali Basin is downwarped, an isostatically balanced, constant crustal thickness model of the Sunda Shelf was perturbed by varying the thickness of the sediment layer until agreement with the gravity data was obtained (Fig. 10b). The gravity profile for Line 67 (Fig. 3b) rather than Line 1 is used because this line is the closest to where the thrust earthquakes occurred. Again the densities and thicknesses noted above for the isostatically balanced Sunda Shelf were assumed for this profile and the slab structure was included.

To match the gravity data the following perturbations were necessary (Fig. 10b): (1) thickening the sedimentary layer to 4 km beneath km 240, (2) a sharp offset in basement at km 240, (3) a small ridge in basement beneath km 200, and (4) thinning the sediment layer beneath the southern end of the line. Thickening of the sediments beneath the Bali Basin was necessary to produce the large gravity negative. While the amount of sediment thickening depends on the assumed densities, the important point is that thickening by downbowing of the crust is required. If the crystalline crust was thinner beneath the basin, then even more downbowing is indicated. For the densities used here the dip angle of the basement between km 210 and 240 is about  $3^\circ$ . The dip angle of the major thrust surface of the Flores thrust zone between km 20 and 35 in Fig. 3a is slightly larger,  $6^\circ$ , probably because, as can be seen in Fig. 3a, the thrust plane splays from a probable decollement surface at depth up through the sedimentary section.

The sharp crustal offset at km 240 and the thinning of the sediments south of that point was demanded by the sharp gradient in gravity from km 240 to 250. Even with a nearly vertical offset in basement, the calculated gradient is less than that observed. While the observed gradient may indicate a greater

density contrast between the crust and sediments, the lack of correlation between the gravity field and bathymetry in the strait between Bali and Lombok (Fig. 2) suggests that it is more likely due to structures to the sides of the profile. Note that the contour lines of bathymetry are nearly tangential to the profile line at its southern end (Fig. 2) and thus the assumption of structural two-dimensionality is violated. Finally, since the crustal thickness is kept constant, deflection of the Moho is implied, but we point out that the gravity data are insensitive to such details of the shape of the Moho.

#### Discussion

Causes of Thrusting In the section of the Sunda arc from Java to Wetar, the convergent margin changes from subduction of old oceanic crust (Indian Ocean) beneath a continental margin (Sunda Shelf) in the west, to subduction of continental crust (Australia) beneath an island arc built on oceanic crust (Banda Arc) in the east. In the east, most of the deformation of the island arc can be attributed to collision with the Australian continent. In the Flores section, the deformation of the arc is probably caused by interaction between the subducting Australian margin and a thick crustal block (Sumba) within the forearc. At the western end, near Bali, however, there is no obvious local cause of the thrusting north of the volcanic arc.

One explanation for the presence of thrusting in the Bali Basin offered by Silver et al. [1983] is lateral propagation of the Flores thrust zone from the east. This mechanism requires that the arc structure act as a beam when it is indented. Because the arc itself is cut extensively by strike-slip faults and because the northward displacement of the volcanic islands north of Timor and

Sumba appears to occur only locally, we feel that lateral propagation of the backarc thrusting is inefficient and does not offer a viable explanation.

Hamilton [1979] suggested a mechanism for the thrusting that centered on the intrusion of magmatic material and required no external forces or net shortening across the arc. He observed that on Java "compressional structures in Neogene materials tend to arc concentrically around, and to be directed outward from, large volcanic edifices". He suggests that the downbowing that allowed the formation of sedimentary basins was due to loading of the crust by volcanoes and that subsequent deformation of the sediments was caused "partly by gravitational flow of the upper crust and its sedimentary cover in response to magmatic loading, and partly by spreading of the crust in the magmatic belt by intrusions within it".

The distinction between the mechanism advocated by Hamilton in which no net shortening across the volcanic arc structure occurs and one in which shortening does occur is basic to our understanding of island arcs, collisions, and whether or not island arcs can reverse subduction direction. While other circumstances may apply to arcs in general, we favor the presence of shortening across the Sunda island arc based on our studies here. First, the lower crustal depths and shallowly dipping nodal planes for the earthquakes beneath the Bali Basin are evidence that basement is actively involved in the thrust faulting. Second, the similarity of the fault plane solutions despite the different locations of the earthquakes relative to the active volcanoes suggests that the thrusting direction is not controlled by the positions of the volcanoes but is due to more uniform slip of the island arc over the backarc basin. Finally, the most critical evidence is the locations of these earthquakes and their relationship to the volcanoes on Bali and Lombok Islands. The locations based on arrival time data (Fig. 7) and the

intensity reports suggest that the thrust earthquakes and thus the thrust fault zone extend beneath the active volcanoes. If so, then mechanisms for the thrusting that rely on swelling of the arc by magmatic intrusion from beneath cannot apply and regional compression of the volcanic arc must be invoked. Silver et al. [1983] also rejected the magmatic intrusion mechanism because the backarc thrusting is observed where there are no volcanoes and because of the absence of obvious extensional features within the arc in places where backarc thrusting is well-developed and significant slip (i.e., tens of kms) has occurred (e.g., Flores). Fault plane solutions for shallow earthquakes within the arc and forearc are predominantly strike-slip and indicate that they are in fact being shortened in the N-S direction [McCaffrey, 1986].

What causes the N-S compression across the arc? The roughly parallel convergence directions between the Sunda Shelf and the island arc in the Bali Basin indicated by slip vectors and between the Indian Ocean plate and Asia [Cardwell et al., 1981; Minster and Jordan, 1978] suggest that plate motions are driving the backarc thrusting; probably through coupling of the plates beneath the forearc. Such coupling could be produced by shallow subduction of the Indian Ocean plate, but we cannot document this because the uncertainties in the earthquake hypocenters do not permit resolution of the subduction angle of the Indian Ocean plate at shallow depths beneath the forearc south of Bali and Lombok. There are other indications, however, that subduction may be steep here. The subducting oceanic crust is very old; both magnetic anomaly lineations [Larson, 1975] and upper Jurassic basal sediments in Deep Sea Drilling Project Hole 261 (at 13°S, 118°E) indicate an age of about late Jurassic to early Cretaceous. The Lombok Basin is the deepest section of the forearc basin (with the exception of the Weber Deep far to the east) and the Java Trench appears to be slightly deeper south of the Lombok Basin (Fig. 1).

There have been no large thrust earthquakes here [Kelleher and McCann, 1976], but there seems to be a tendency for normal faulting events at the trench (possibly related to sharp downbending of the oceanic plate) [Cardwell and Isacks, 1978], including the  $M_s$ -8.1 Sumba earthquake of 1977. The foregoing observations might argue for a steep subduction angle and very weakly coupled subduction. In fact, considerations of such factors as slab dip (at greater depths beneath the arc), convergence rate, lithospheric age, and maximum earthquake size, place the Java trench globally among subduction zones at which backarc spreading, and not backarc compression, occurs [Ruff and Kanamori, 1980; Uyeda and Kanamori, 1979].

Alternatively, as Silver et al. [1983] suggest, and we favor this view, the thrusting in the Bali Basin may be due to collision with the Roo Rise, a bathymetric high that intersects the Java trench between  $110^\circ$  and  $115^\circ$ E (Fig. 1) and probably extends to the NE beneath the forearc south of Bali. Kelleher and McCann [1976] inferred that the Roo Rise resists subduction because of its buoyancy and is responsible for the lack of great thrust earthquakes in the forearc south of Java. Details of the interaction of the Roo Rise with the forearc are lacking, but lateral changes in forearc structure appear to coincide with the Roo Rise (the forearc outer ridge is more elevated and the forearc basin is narrower here than to the east and the Java Trench appears to be slightly indented [Hamilton, 1979]), indicating that some modification of the subduction process is taking place.

Analogy with the Andes and western North America In the forelands of both the Andes and western North America two styles of deformation are dominant; (1) the thin-skinned style of the Canadian Rockies [Bally et al., 1966; Price, 1981; Price and Mountjoy, 1970], Sevier Desert [Armstrong, 1968], Bolivia, and Argentina [Jordan et al., 1983] and (2) block faulting, or thick-skinned,

style of the Laramide [Berg, 1962; Prucha et al., 1965; Smithson et al., 1979] and Pampeanas [Jordan et al., 1983] ranges. In the Andes, while the thin-skinned deformation occurs over both nearly horizontal and shallow dipping ( $\approx 30^\circ$ ) subducting slabs, the thick-skinned deformation is limited to regions where the slabs are nearly horizontal. In the western U.S. the development of the Laramide basement faults was accompanied by an eastward migration of the volcanic arc and this has led to the popular view that the slab was very shallowly dipping during the episode of Laramide deformation.

The style of deformation in the Bali Basin appears to be intermediate between that of the thin-skinned style east of the Andes and Rockies and the basement block-faulting of the Laramide or the Pampeanas. While the earthquakes examined in this report certainly occur within basement, and not along a decollement at the base of the sedimentary sequence, they are also of fairly low angle and the associated basement faults do not seem to extend into the sedimentary layer. The sediments respond to basement shortening by folding and are probably decoupled from basement along an aseismic shallow dipping plane that steepens into basement and becomes seismic only beneath the southern edge of the Bali Basin. The Madura-Kangean, Meratus, and Pulau Laut Ridges are basement uplifts that sit in the same tectonic position as the Laramide and Pampeanas basement uplifts and the available information indicates that they are the roots of anticlines formed by compression [Ben-Avraham and Emery, 1973].

The Java-Bali section of the Sunda Arc is a likely analog for the initial stages of thrusting on the east side of the Andes [Jordan et al., 1983]. Suarez et al. [1983] propose an evolutionary scenario for the Andes that begins with the Brazilian Shield thrusting westward beneath the volcanic chain, forming a small foreland basin and uplifting the mountain belt. As the

thrusting and uplift proceed, at some point it becomes easier to form a new thrust zone within the shield to the east than to continue uplifting the mountains. Suarez et al. [1983] envision that the lateral growth of the Andes proceeds by successive eastward jumps in the locus of thrusting and uplift. Such outward (eastward) migration of foreland thrusting may have also occurred in western North America [e.g., Armstrong and Oriel, 1965], though this view is not held by all [Mountjoy, 1966].

We suggest a scenario for the growth of the arc in the Java-Bali region of the Sunda arc that is similar to that proposed for the Andes by Suarez et al. [1983] but in its infancy. The Sunda arc example also suggests that discrete jumps in the locus of faulting proceed along strike as well as outward from the mountain belt. The evolutionary sequence along strike is exemplified here by the spatial and temporal development of the Java, Bali, and Flores Basins.

The greater widths of Java and Sumatra than those of the islands to the east are not due to voluminous magmatic activity but rather because of the exposure of the foreland basins. The Java Basin in the Tertiary was a shallow marine basin bordered on the north by the subaerial Sunda Shelf and to the south by an active volcanic arc [Weeda, 1958]. (A similar basin formed in Sumatra [Katili, 1974], but we limit our discussion to the Java Basin.) Prior to the development of the Java Basin, the Sunda Shelf probably extended to the present south coast of Java and, accordingly, the Java Basin formed as a downwarp in the Sunda Shelf. The 6-km-thick sedimentary sequence in the Java Basin reveals a marine transgression in the Oligocene, bathyal marine conditions in the Miocene, and land conditions by Pliocene [Hamilton, 1979; Weeda, 1958]. Folding in the west Java Basin began in the Miocene when bathyal conditions prevailed [Hamilton, 1979] and the intensity of folding decreased towards the Madura basin to the east and towards the volcanic arc to

the south [Weeda, 1958]. The end of sedimentation in the Java Basin is marked by emergence and a major orogenic phase in middle to late Pleistocene [Soetantri et al., 1973]. Today in the Madura and Java Basins, the younger sediments are less deformed than the older, but even upper Quaternary sediments are involved in the compressional deformation [Hamilton, 1979; Weeda, 1958]. The total amount and present rate of shortening in the Java Basin are unknown but the lack of earthquakes or gravity anomalies suggest that they are small, despite the evidence for continued deformation [Weeda, 1958].

Activity began in the Bali Basin as it waned in the Java Basin and we are probably witnessing a similar progression underway in the Bali Basin. However, we do not intend to infer a causal relationship between the onset of deformation in one basin and its demise in the other. The high variability in the character of backarc thrusting at present along the Sunda Arc indicates that the thrusting is strongly dependent on conditions in the forearc as well as the backarc [Silver et al., 1983]; hence the eastward migration of activity in the backarc from Java to Bali may reflect some forearc process (such as migration of the Roo Rise), as easily as a backarc process (for instance, the resistance of the buoyant Sunda Shelf to thrusting beneath the volcanic arc). The point is that at some time in the future, the Java and Bali Basins may appear as a linear zone of deformation but will be characterized by greatly different histories. Also structurally on line with the Bali and Java Basins will be the suture along which the Flores Basin closed. The Flores Basin, while undergoing closure concurrently with the Bali Basin, is morphologically distinct from the Bali Basin in that it is floored by oceanic crust and is much deeper. With the exceptions of subtle sedimentological facies differences and the possibility that its suture will be marked by ophiolites, the

structures resulting from closure of the Bali and Flores Basins may be indistinguishable. The picture will be complicated further if new fold and thrusts belts develop outboard (north) of the old, as in the scenario of Suarez et al. [1983].

#### Summary

The focal depths and fault plane solutions for 8 earthquakes from the Bali Basin have been determined by inversion of long-period P and SH waves and short-period P waves. The results indicate that thrusting occurs beneath the southern margin of the Bali Basin at depths that range from 10 to 18 km and on planes that dip to the south at angles between 13° to 35°. The events had seismic moments that range from  $4 \times 10^{17}$  to  $7 \times 10^{18}$  Nm, and several were quite destructive. Summation of seismic moments suggests a minimum closure rate of  $4 \pm 2$  mm/a over the past 25 years.

Characteristics of the waveforms and the earthquake locations with respect to crustal models constrained by gravity and seismic data suggest that they occurred primarily within the crystalline basement, beneath the sedimentary layer. The south dipping nodal planes that we infer to be the fault planes dip too steeply to be due to thrusting on a zone of decollement between the basement and the sediment layer but also too shallowly to be analogous to the steep faults along which thick basement blocks are uplifted, such as during the Laramide faulting of western North America or in the Pampeanas Ranges of the Andes. These earthquakes probably reveal some intermediate activity, such as basement shortening south of the foreland fold-and-thrust belt represented by the central part of the Bali Basin.

The similarity of the slip vectors of the 8 earthquakes to the convergence direction between the Asian and Indian Ocean plates suggests that the thrusting in the backarc region is related to plate convergence. Collision or strongly coupled subduction is indicated. However, because the arc is extensively cut by strike-slip faults, it is probably quite weak, and the thrusting here is not easily relatable to the collision between the Australian continent and eastern Sunda Arc that occurs several hundred kilometers to the east. Moreover, the Mesozoic age of the subducting lithosphere, the morphology of the forearc south of Bali, the lack of thrust events beneath the forearc, and a preponderance of large, shallow normal-faulting events at the Java trench suggest that the upper and lower plates are weakly coupled. The only likely scenario involving a collision is interaction with the Roo Rise, a broad feature with approximately 1 km of relief that rises above the Indian Ocean floor and intersects the Java Trench south of Java and Bali.

Finally, we propose a scenario for the development of the Bali, Java, and Flores Basins that has implications for the development of continental fold-and-thrust belts and for the growth of continental arcs such as the Andes and western North America. The island of Java has nearly doubled in width during the Tertiary by the addition of a wide and deep sedimentary basin to its backside. This basin likely formed in the Sunda Shelf and was filled by sediments from both the magmatic arc to the south and from the Sunda Shelf to the north. This process occurs now in the Bali Basin. Folding and thrusting within the Java Basin continue to the present, but has declined in intensity and the Java Basin is now exposed. The Bali Basin formed east of the Java Basin and is now in the process of being closed by thrusting. To the east of the Bali Basin, the Flores Basin, of oceanic origin, is actively closing by thrusting at its southern margin. This example suggests that individual thrust

episodes may migrate along strike as well as outward from mountain belts.

Acknowledgements. We thank P. Molnar for helpful discussions and E. A. Silver and R. K. Cardwell for reviews. This work was funded by NSF Grant EAR-8319250 and in part by the Air Force Geophysics Scholar Program.

## Appendix

The formal uncertainties in the earthquake source parameters determined by the inversion procedure underestimate the true uncertainties. Here, we briefly assess the realistic uncertainties, examine the possible trade-offs between parameters, and present our strategies for deciding on the best solution. The procedure followed is to fix the parameter being examined at values that bracket the best fitting value, and solve for the remaining parameters. In the figures that follow, only selected seismograms are shown but all calculations were done with all the available seismograms (Fig. 6).

Focal depths For the range of depths, source durations, and mechanisms presented in this paper, events 2, 6, and 8 are probably representative and are used to examine depth uncertainties. For event 2 (Fig. A1), the strong trade-off between the depth, source duration, and dip angle results in very little increase in variance between 5 and 13 km depth. At depths greater than 13 km the reflected phases are too late, resulting in phase mismatch and large variance. We feel that the diagnostic seismogram is at AAE, for which the shallower solutions give a poor fit to the P-wave because of the increase in the dip angle. From this, we infer that event 2 is no deeper than 16 km and no shallower than 8 km. Although the P-wave seismogram at AAE was not available for event 1, we suggest that the uncertainty in its depth is also  $\pm 5$  km, based on the similarity of the seismograms to those of event 2, and the proximity in time and space of the two events.

Event 6 (Fig. A2) shows much less of a trade-off between the depth and other parameters. Although the source duration increases, the dip angle is more stable than for event 2 and the variance increases with decreasing depth. This stability in the dip angle is due to the increase in the relative strength and

number of P-wave seismograms with P and pP phases of opposite polarity (such as AAE for event 2). For the shallower assumed sources, the initial cycle of the calculated seismogram for GUA becomes small because of the destructive interference between P and pP. The estimated uncertainty in depth of  $\pm 4$  km for this event probably also applies to events 3, 4, 5, and 7, because of the similarity in their mechanisms and station distributions.

Event 8 (Fig. A3) is similar in depth and orientation to event 1 but has a longer source duration. As for event 2, there is a trade-off between depth and source duration but over a greater range of depths; from 12 to 24 km. Above 9 km the variance decreases because of the change in dip but again this produces an unacceptable fit at AAE.

The uncertainty in source depths and the variations in seismic moment with depth introduces an uncertainty of approximately 50% in the estimated seismic moments (Figs. A1, A2, and A3). An additional systematic bias in the depth (not included in Table 1) is caused by the uncertainty in the velocity used to calculate seismograms. If the average velocities in the earth above the source range from 5.5 to 7.5 km/s, the bias in depth will be about  $\pm 20\%$  of the calculated depth.

Orientation The uncertainties in strike, dip, and rake are measured with respect to the N-dipping nodal planes. For event 2 (and by similarity, for events 1 and 8), the uncertainty in strike is between 10 and 20° (Fig. A4). For this mechanism the near nodal P and SH waves are most sensitive to strike but there is a trade-off with the rake angle. The uncertainty in strike for event 3 (and events 4-7) is greater ( $\pm 20$ -30°; Fig. A5) than that for event 2 despite the decrease in trade-off with the rake angle.

The dip angle of the N-dipping nodal plane is constrained within  $\pm 5^\circ$  (Fig. A6). The most obvious constraints are the polarities of the P-waves but the SH

wave amplitudes are also sensitive to the dip angle. Because the dip angle is determined largely by seismograms at the northern stations, it will vary directly with the take-off angles for rays to these stations. For a range in source velocities from 5.5 to 7.5 km/s, the take-off angles and thus dip angles will vary by  $\pm 5^\circ$  for a dip angle of  $60^\circ$  and by  $\pm 2^\circ$  for a dip angle of  $75^\circ$ .

The uncertainty in the rake angle for event 3 is approximately  $20^\circ$  (Fig. A7) and is probably similar for the other events. The rake angle is largely constrained by the SH waves but trades off strongly with the strike angle. Note that a difference in the rake angle of  $20^\circ$  on the N-dipping auxiliary plane corresponds to differences in the S-dipping (fault) plane of approximately  $30^\circ$  in strike and less than  $5^\circ$  in dip (compare in Fig. 6 events 3 and 5 whose rake angles differ by  $18^\circ$ ).

Throughout the tests of the orientation parameters, the depth ( $\pm 1$  km), source duration ( $\pm 1$  s), and seismic moment ( $\pm 10\%$ ) remain very stable.

## References

Aki, K., and P.G. Richards, Quantitative Seismology, Theory and Methods, W.H. Freeman and Co., San Francisco, 557 pp., 1980.

Armstrong, R.L., Sevier orogenic belt in Nevada and Utah, Bull. Geol. Soc. Am., 79, 429-458, 1968.

Armstrong, R.L., and S.S. Oriel, Tectonic development of Idaho-Wyoming thrust belt, Bull. Am. Assoc. Pet. Geol., 49, 1847-1866, 1965.

Baily, A.W., P.L. Gordy, and G.A. Stewart, Structure, seismic data, and orogenic evolution of the southern Canadian Rocky Mountains, Canadian Pet. Geol. Bull., 14, 337-381, 1966.

Ben-Avraham, Z., Structural framework of the Sunda Shelf and vicinity, Ph.D. thesis, Mass. Inst. of Tech. and Woods Hole Oceanog. Inst., 269 p., 1973.

Ben-Avraham, Z., and K.O. Emery, Structural framework of Sunda Shelf, Bull. Am. Assoc. Pet. Geol., 57, 2323-2366, 1973.

Berg, R.R., Mountain flank thrusting in Rocky Mountain foreland, Wyoming and Colorado, Bull. Am. Assoc. Pet. Geol., 46, 2029-2032, 1962.

Boatwright, J., A spectral theory for circular seismic sources; simple estimates of source dimensions, dynamic stress drop, and radiated seismic energy, Bull. Seismol. Soc. Am., 70, 1-27, 1980.

Bowin, C.O., W. Warsi, and J. Milligan, Free-air gravity anomaly atlas of the world, Geol. Soc. Am. Map and Chart Ser., MC-46, 1982.

Brune, J.N., Seismic moment, seismicity, and rate of slip along major fault zones, J. Geophys. Res., 73, 777-784, 1968.

Caldwell, W.F., W.F. Haxby, D.E. Karig, and D.L. Turcotte, On the applicability of a universal elastic trench profile, Earth Planet. Sci. Lett., 31, 239, 1976.

Cardwell, R.K., and B.L. Isacks, Geometry of the subducted lithosphere beneath the Banda Sea in eastern Indonesia from seismicity and fault plane solutions, J. Geophys. Res., 87, 2825-2838, 1978.

Cardwell, R.K., E.S. Kappel, M.S. Lawrence, and B.L. Isacks, Plate convergence along the Indonesian arc, (abstr.), Eos Trans. AGU, 62, 404, 1981.

Curry, J.R., G.G. Shor, R.W. Raith and M. Henry, Seismic refraction and reflection studies of crustal structure of the eastern Sunda and western Banda arcs, J. Geophys. Res., 82, 2479, 1977.

Effendi, I., T. Priantono, S. Tjokrosapoetro, and K. Budiono, Overview of disastrous tectonic earthquakes in the period between April 1979 - April 1980, Bull. Geol. Res. Dev. Centre, Indonesia, 4, 18-20, 1981.

Fitch, T.J., Earthquake mechanisms and island arc tectonics in the Indonesian-Philippine region, Bull. Seismol. Soc. Am., 60, 565-591, 1970.

Fitch, T.J., R.G. North, and M.W. Shields, Focal depths and moment tensor representations of shallow earthquakes associated with the great Sumba earthquake, J. Geophys. Res., 86, 9357-9374, 1981.

Futterman, W.I., Dispersive body waves, J. Geophys. Res., 67, 5279-5291, 1962.

Ganse, R.A., and J.B. Nelson, Catalog of Significant Earthquakes 2000 B.C. - 1979, Including quantatative casualties and damage, World Data Center A for Solid Earth Geophysics, 154 pp., 1981.

Grow, J.A., and C.O. Bowin, Evidence for high density crust and mantle beneath the Chile trench due to the descending lithosphere, J. Geophys. Res., 80, 1449-1458, 1975.

Hamilton, W., Tectonics of the Indonesian region, U.S. Geol. Surv. Prof. Paper 1078, 345 pp., 1979.

Hayat, D. Z., and S. Panjaitan, 1983, private communication.

Herrin, E., 1968 seismological tables for P phases, Bull. Seismol. Soc. Am., 58, 1193-1352, 1968.

Jordan, T.E., B.L. Isacks, R.W. Allmendinger, J.A. Brewer, V.A. Ramos and C.J. Ando, Andean tectonics related to geometry of subducted Nazca plate, Bull. Geol. Soc. Am., 94, 341-361, 1983.

Kappel, E.S., Plate convergence in the Sunda and Banda arcs, B.A. Thesis, Cornell University, 40 pp., 1980.

Katili, J.A., Sumatra, in A.M. Spencer (ed.), Mesozoic-Cenozoic Orogenic Belts, Data for Orogenic Studies, Geol. Soc. London, 317-331, 1974.

Kelleher, J., and W. McCann, Buoyant zones, great earthquakes, and unstable boundaries of subduction, J. Geophys. Res., 81, 4885-4896, 1976.

Larson, R.L., Late Jurassic sea-floor spreading in the eastern Indian Ocean, Geology, 3, 69-71, 1975.

McCaffrey, R., 1986, private communication.

McCaffrey, R., P. Molnar, S. Roecker and Y. Joyodiwiryo, Microearthquake seismicity and fault plane solutions related to arc-continent collision in the eastern Sunda arc, Indonesia, J. Geophys. Res., 90, 4511-4528, 1985.

McCaffrey, R., and J. Nabelek, The geometry of backarc thrusting along the eastern Sunda arc, Indonesia: constraints from earthquake and gravity data, J. Geophys. Res., 89, 6171-6179, 1984.

McCaffrey, R., and J. Nabelek, Seismological evidence for shallow thrusting north of the Timor trough, Geophys. J. Roy. Astr. Soc., 85, 365-381, 1986.

Minster, J.B., and T.H. Jordan, Present-day plate motions, J. Geophys. Res., 83, 5331-5354, 1978.

Molnar, P., Gravity anomalies and the origin of the Puerto Rico trench, Geophys. J. Roy. Astr. Soc., 51, 701-708, 1977.

Mountjoy, E.W., Time of thrusting in Idaho-Wyoming thrust belt - Discussion, Bull. Am. Assoc. Pet. Geol., 50, 2612-2614, 1966.

Nabelek, J., Determination of earthquake source parameters from inversion of body waves, Ph.D. thesis, Mass. Inst. of Tech., 1984.

Nabelek, J., Geometry and mechanism of faulting of the 1980 El Asnam, Algeria, earthquake from inversion of teleseismic body waves and comparison with field observations, J. Geophys. Res., 90, 12713-12728, 1985.

Price, R.A., The Cordilleran foreland thrust and fold belt in the southern Canadian Rocky Mountains, in Thrust and Nappe Tectonics, Geol. Soc. London Spec. Publ., vol. 9, K.R. McClay and N.J. Price, 427-448, Blackwell Scientific, London, 1981.

Price, R.A., and E.W. Mountjoy, Geologic structure of the Canadian Rocky Mountains between Bow and Athabasca Rivers - a progress report, Geol. Assoc. Canada, Spec. Pap. No. 6, p. 7-25, 1970.

Prucha, J.J., J.A. Graham, and R.P. Nickelson, Basement controlled deformation in Wyoming province of Rocky Mountain foreland, Bull. Am. Assoc. Pet. Geol., 49, 966-992, 1965.

Raitt, R.W., Marine seismic refraction studies of the Indonesian island arc, (abstr.), Eos Trans. AGU, 48, 217, 1967.

Ruff, L., and H. Kanamori, Seismicity and the subduction process, Phys. Earth Planet. Int., 23, 240-252, 1980.

Silver, E.A., D.R. Reed, R. McCaffrey, and Y.S. Joyodiwiryo, Backarc thrusting in the eastern Sunda arc, Indonesia: a consequence of arc-continent collision, J. Geophys. Res., 88, 7429-7448, 1983.

Silver, E.A., N.A. Breen, H. Prasetyo and D. Hussong, Multibeam study of the Flores backarc thrust belt, Indonesia, J. Geophys. Res., 91, 3489-3500, 1986.

Silver, E.A., S. Roof, N.A. Breen and D. Hussong, 1986, private communication.

Smithson, S.B., J.A. Brewer, S. Kaufman, J.E. Oliver, and C.A. Hurich, Structure of the Laramide Wind River uplift, Wyoming, from COCORP deep reflection data and from gravity data, J. Geophys. Res., 84, 5955-5972, 1979.

Soentantri, B., L. Samuel, and G.A.S. Nayoan, The geology of the oilfields in north east Java, Proc. Indonesian Pet. Assoc., 149-175, 1973.

Suarez, G., P. Molnar and C. Burchfiel, Seismicity, fault plane solutions, depth of faulting, and active tectonics of the Andes of Peru, Ecuador, and southern Colombia, J. Geophys. Res., 88, 10,403-10,428, 1983.

Usna, I., S. Tjokrosapoetro and S. Wiryo Sujono, Geological interpretation of a seismic reflection profile across the Banda Sea between Wetar and Buru islands, Bull. Geol. Res. Dev. Centre, Indonesia, 1, 7, 1979.

Uyeda, S., and H. Kanamori, Back-arc opening and the mode of subduction, J. Geophys. Res., 84, 1049-1061, 1979.

van Bemmelen, R.W., The Geology of Indonesia, v. 1A, 732 pp., Government Printing Office, The Hague, 1949.

Walcott, R.I., Flexural rigidity, thickness, and viscosity of the lithosphere, J. Geophys. Res., 75, 3941-3954, 1970.

Watts, A.B., and M. Talwani, Gravity anomalies seaward of deep-sea trenches and their tectonic implications, Geophys. J. Roy. Astr. Soc., 36, 57-90, 1974.

Watts, A.B., and M. Talwani, Gravity effect of downgoing lithospheric slabs beneath island arcs, Bull. Geol. Soc. Am., 86, 1-4, 1975.

Weeda, J., Oil basin of east Java, in L.G. Weeks (ed.), Habitat of Oil, Am.

Assoc. Pet. Geol., 1359-1364, 1958.

Wismaya, M.B., 1981, private communication.

Woppard, G.P., The new gravity system -- changes in international gravity  
base values and anomaly values, Geophys., 44, 1352-1366, 1979.

### Figure Captions

1. Tectonic and geographic map of the eastern Sunda Arc and vicinity. Active volcanoes are represented by triangles and bathymetric contours are in kilometers. Thrust faults are shown with teeth on the upper plate. The dashed box encloses the study area.
2. Bathymetric and free-air gravity maps of the Bali Basin and vicinity. Contours are in meters and mGals ( $10^{-5}$  m/s<sup>2</sup>), respectively, and are dashed or omitted where data control is poor. The lighter points show the locations of measurements. Heavy lines show the locations of Lines 63, 67, and B22, and the brackets enclose the data used to construct Line 1. Large dots show the locations of the earthquakes discussed in this paper.
3. Free-air gravity profiles and line drawings of seismic reflection profiles (from Silver et al. [1983]) across the Bali Basin near Lombok. The locations of these lines are shown in Fig. 2.
4. Seismic profile crossing the southern Sunda Shelf and Bali Basin north of Lombok (from Ben-Avraham [1973]). Location of profile is shown in Fig. 2. The top figure shows the digitized bathymetry (dots) at high vertical exaggeration and theoretical curves for a flexed elastic plate. For a plate deflected vertically at its free end, the solution is of the form  $z(x) = z_0 \cos(\lambda x) e^{-\lambda x}$ , where  $z$  is the deflection at distance  $x$ ,  $z_0$  is the deflection at  $x=0$ ,  $\lambda = ((\rho_m - \rho_w)g/4D)^{1/2}$ ,  $g$  is the gravitational acceleration (9.8 m/s<sup>2</sup>), and  $D$  is the flexural rigidity of the plate [Watts and Talwani, 1974]. Assumed densities for the mantle and water are:  $\rho_m = 3300$  kg/m<sup>3</sup>,  $\rho_w = 1000$  kg/m<sup>3</sup>. The curves are for flexural rigidity values of 1, 5, and  $10 \times 10^{22}$  Nm (as marked).

5. (a) Seismicity of the Bali region from 1964-1979 (all events listed by the ISC). Depth intervals are in km. (b) Cross-section of seismicity in the Bali region. This projection passes through 8°S, 115°E, at an azimuth of 10°, and includes all events within 300 km and recorded by more than 50 seismograph stations. In both plots, triangles show the locations of active volcanoes.

6. Plots of waveforms and fault plane solutions for Bali Basin earthquakes. As in all following figures, observed seismograms are shown by solid lines and the dashed lines are calculated seismograms. On the left in each plot are the P waves and on the right are the SH waves. Letters at the lower right of station codes correspond to those in the focal sphere and an asterisk indicates that the seismogram was not included in the inversion. The small vertical bars show the time window used in the inversion. The normalized source time function is shown on the time axis and the amplitude scale is for seismograms (normalized to an instrument magnification of 3000 and an epicentral distance of 40°).

7. (a) Lower hemisphere projections of fault plane solutions near Bali Island determined in this study. Stippled quadrants are those with compressional P wave first motions. P and T axes are shown by large dots. Events shown with larger focal spheres have seismic moments greater than  $10^{18}$  Nm.

(b) Cross-section of Bali earthquakes with side projections of their fault plane solutions. The dipping lines through the hypocenters represent the projections of the inferred fault planes and the vertical lines show the range of possible depths.

8. Short-period P wave seismograms for events 3 and 4. The fault plane solutions and source structures are the same as for the long-period data (Fig. 6 and Table 1). Amplitudes have been normalized by the rms amplitude within the inversion window.

9. Selected short- and long-period P seismograms for event 3, used to examine the effects of the assumed source structure on the waveforms. For the short-period data, the amplitudes are normalized (see Fig. 8) and the source orientation is fixed. The orientation was allowed to vary for the long-period data. Clearly, the best fit to both the long- and short-period data is for case E.

10. Structural models and gravity data for the Bali Basin. The numbers in each layer give its density in  $\text{kg/m}^3$  (except for the slab in which the density contrast is given). (a) Isostatically balanced model along Line 1. The top structural model is for the crustal structure (vertical exaggeration of 4) and the bottom shows the entire assumed structure (no vertical exaggeration). (b) Structural model beneath Line 67 that satisfies gravity data and assumes a constant thickness for the crystalline crust of the Sunda Shelf. The small lines beneath kms 250 to 280 show the relocated positions of the earthquakes (based on arrival time data) relative to this model. The slopes of the lines show roughly the dips of the inferred fault planes for the events. Note that the waveform data suggest that the earthquakes occurred beneath thick sediments that are probably found 10 to 30 km to the north of the positions shown.

A1. Comparison of observed (solid lines) and calculated (dashed lines) P wave seismograms of event 2 for a range of depths. The depth is held fixed while the remaining parameters (strike, dip, rake, moment, and the source time function) are determined by the inversion. The variance is normalized by the variance of the best-fitting solution. Seismic moment is in units of  $10^{16}$  Nm.

A2. Comparison of observed and calculated P wave seismograms of event 6 for a range of depths. Format as in Fig. A1.

A3. Comparison of observed and calculated P wave seismograms of event 8 for a range of depths. Format as in Fig. A1.

A4. Comparison of observed and calculated P and SH wave seismograms of event 2 for a range of strike angles. Format as in Fig. A1.

A5. Comparison of observed and calculated P and SH wave seismograms of event 3 for a range of strike angles. Format as in Fig. A1.

A6. Comparison of observed and calculated P and SH wave seismograms of event 3 for a range of dip angles. Format as in Fig. A1.

A7. Comparison of observed and calculated P and SH wave seismograms of event 3 for a range of rake angles. Format as in Fig. A1.

Table 1. Earthquake hypocentral and fault plane solution data.

No.	Date	Origin Time <sup>1</sup>	Lat. °S	Lon. °E	Depth (km) ISC	Mo <sup>2</sup> "pP"	Wave- form	Duration m <sub>b</sub> <sup>3</sup> (s)	Auxiliary Plane			Fault Plane			Layer <sup>4</sup> (km)					
									Str	Dip	Rake	Str	Dip	Rake						
1	May 18, 1963	12:20:31.5	8.21	115.55	54	--	16.0 <sup>±</sup> 1.0 <sup>8</sup>	4.3 <sup>±</sup> 2.5	3.9	--	25.9 <sup>±</sup> 2	7.6 <sup>±</sup> 2	8.4 <sup>±</sup> 5	102	15	112	13	11	0.0	0
2	May 22, 1963	21:53:01.6	8.14	115.66	56	--	13.4 <sup>±</sup> 0.8	7.9 <sup>±</sup> 2.9	2.5	--	26.6 <sup>±</sup> 2	7.8 <sup>±</sup> 2	8.3 <sup>±</sup> 4	116	14	119	15	14	0.0	0
3	July 14, 1976	7:13:23.7	8.17	114.79	37	53	13.7 <sup>±</sup> 0.6 <sup>8</sup>	6.94 <sup>±</sup> 8.4	2.7	6.1	27.9 <sup>±</sup> 2	5.8 <sup>±</sup> 1	8.7 <sup>±</sup> 2	105	32	94	17	7	0.5	6
4	July 14, 1976	10:23:46.8	8.15	114.79	41	10	9.6 <sup>±</sup> 0.6 <sup>7</sup>	4.2 <sup>±</sup> 4	1.3	5.9	27.5 <sup>±</sup> 2	5.8 <sup>±</sup> 1	8.2 <sup>±</sup> 2	110	33	102	8	6	0.5	5
5	May 21, 1979	16:31:1.8	8.33	115.87	44	36	12.3 <sup>±</sup> 1.1	5.5 <sup>±</sup> 2.6	2.9	5.6	26.5 <sup>±</sup> 3	6.1 <sup>±</sup> 2	6.9 <sup>±</sup> 3	123	35	122	7	5	1.3	6
6	May 30, 1979	9:38:55.3	8.31	115.86	40	20	11.0 <sup>±</sup> 0.5	2.36 <sup>±</sup> 8.4	3.4	6.0	27.1 <sup>±</sup> 1	6.1 <sup>±</sup> 1	7.3 <sup>±</sup> 1	123	33	117	19	5	1.5	6
7	Oct. 20, 1979	1:41:10.3	8.38	115.87	37	38	13.7 <sup>±</sup> 0.6	4.87 <sup>±</sup> 8.0	6.0	5.9	27.0 <sup>±</sup> 2	6.3 <sup>±</sup> 1	7.8 <sup>±</sup> 2	115	29	112	20	8	1.5	6
8	Dec. 17, 1979	19:58:23.0	8.50	115.76	22	92	18.0 <sup>±</sup> 0.8	4.48 <sup>±</sup> 11.0	5.2	5.6	26.0 <sup>±</sup> 2	7.5 <sup>±</sup> 1	7.0 <sup>±</sup> 4	134	25	141	18	10	1.0	3

<sup>1</sup> Relocated epicenter and origin time.<sup>2</sup> Seismic moment is in  $10^{16}$  Nm.<sup>3</sup> Taken from ISC Bulletins.<sup>4</sup> W represents water depth. S represents sediment thickness.<sup>5</sup> All quoted formal errors are 2 standard deviations.<sup>6</sup> 13.3<sup>±</sup>0.2 from short-period data<sup>7</sup> 8.0<sup>±</sup>0.3 from short-period data

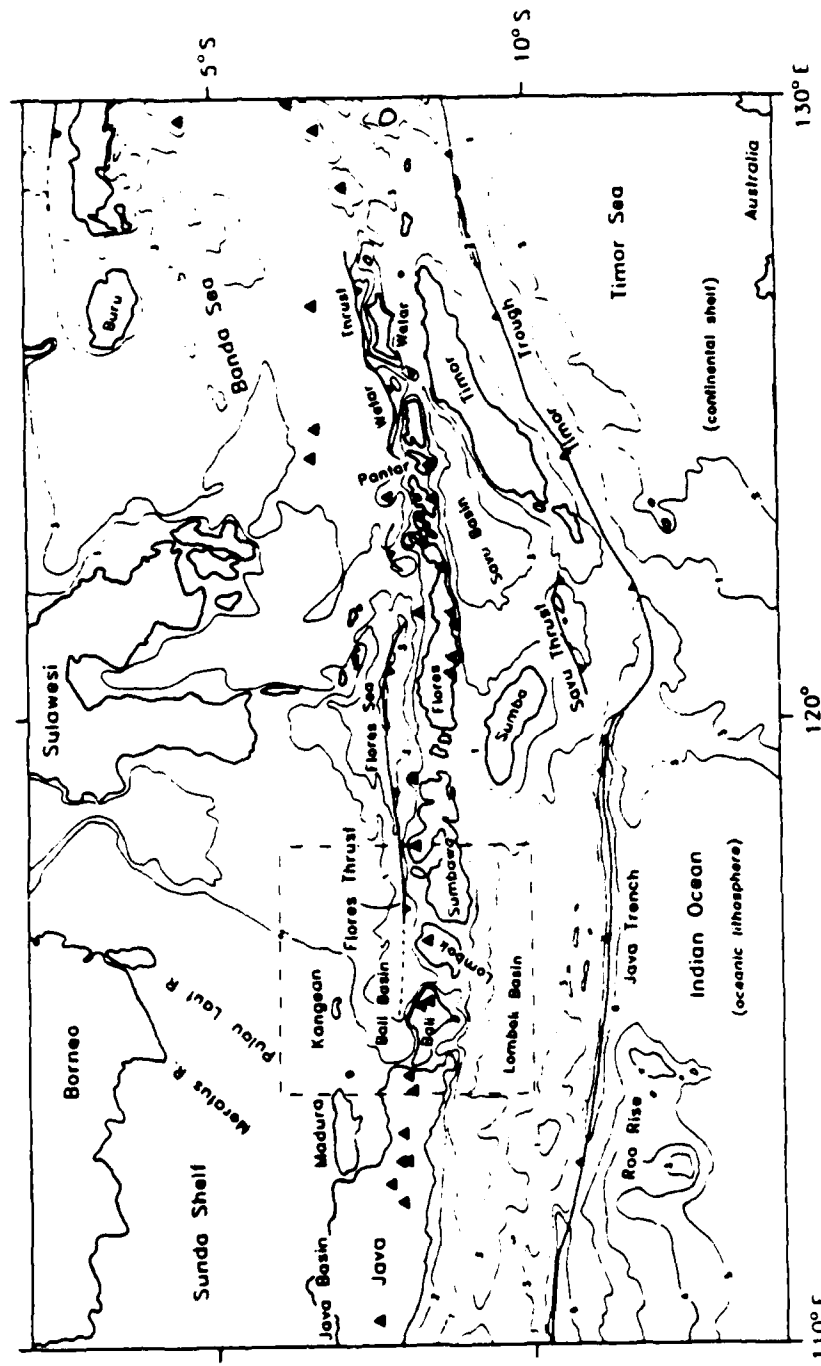


FIGURE 1

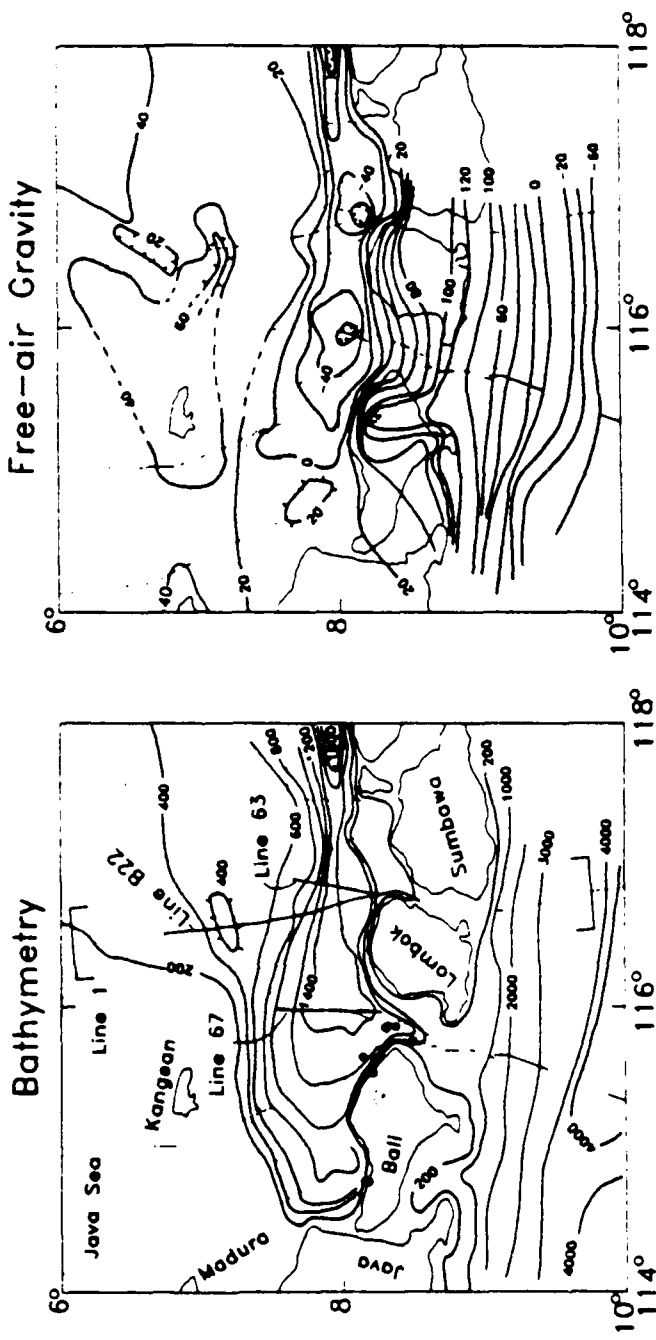


FIGURE 2

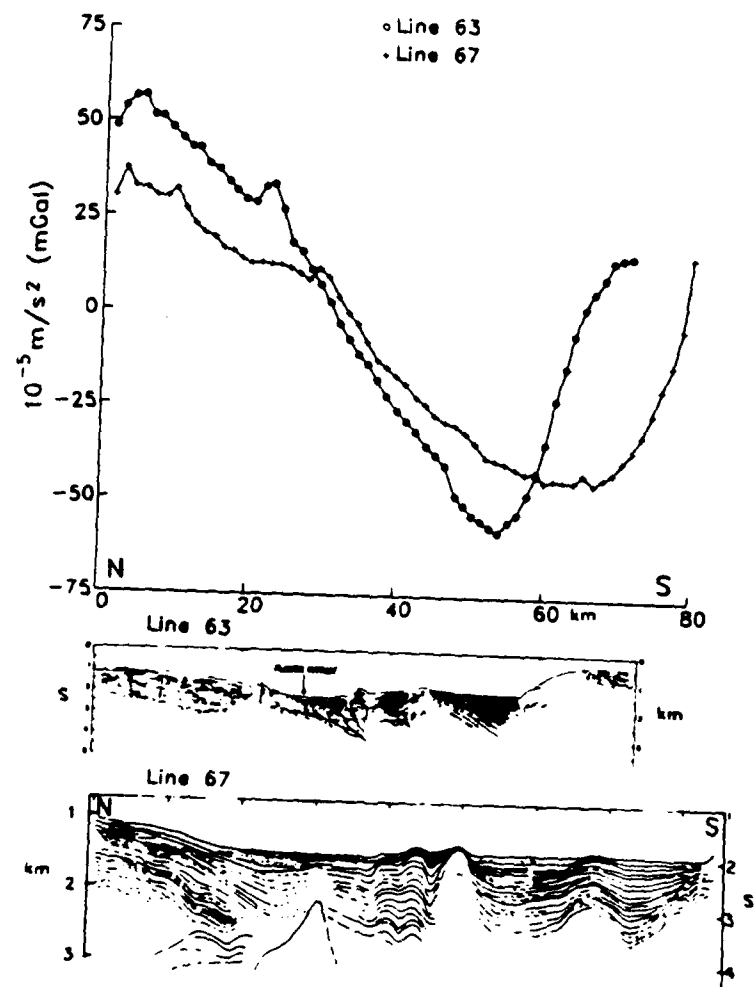


FIGURE 3

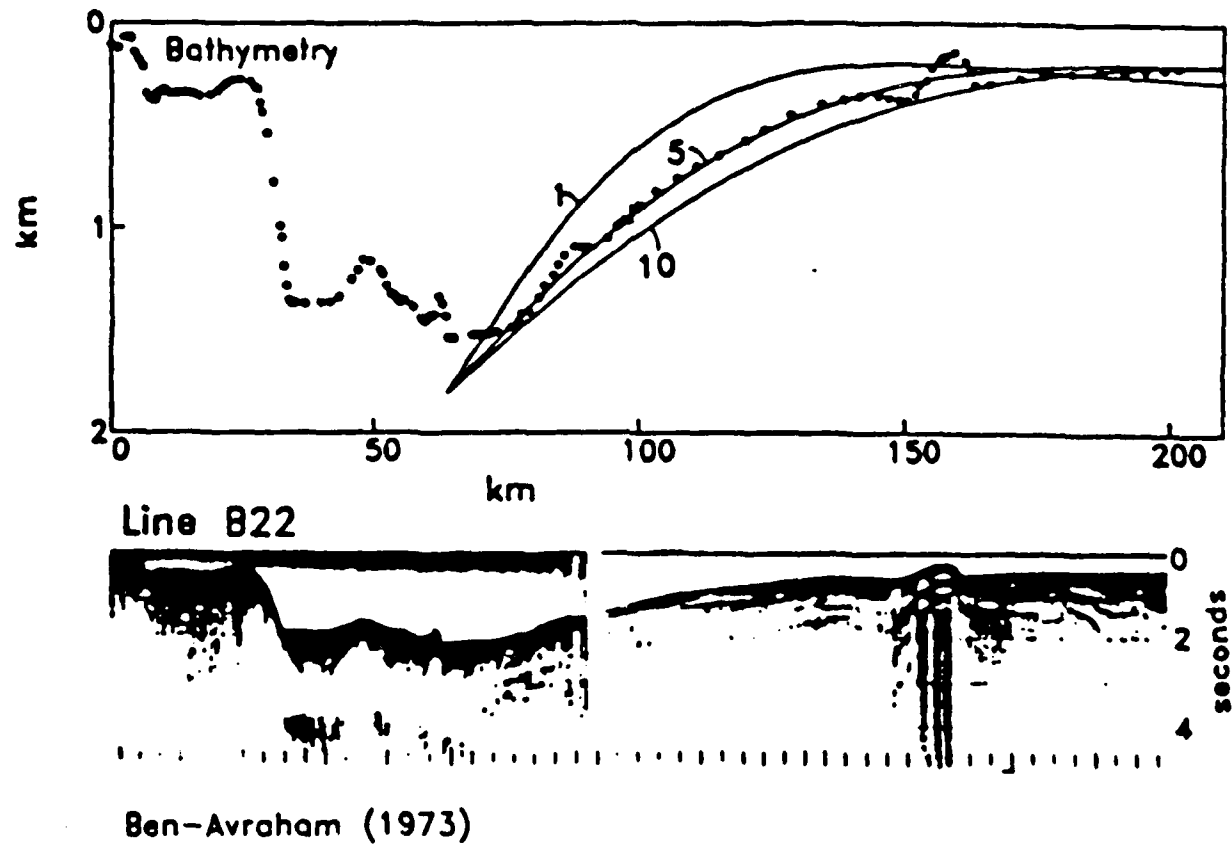


Figure 4

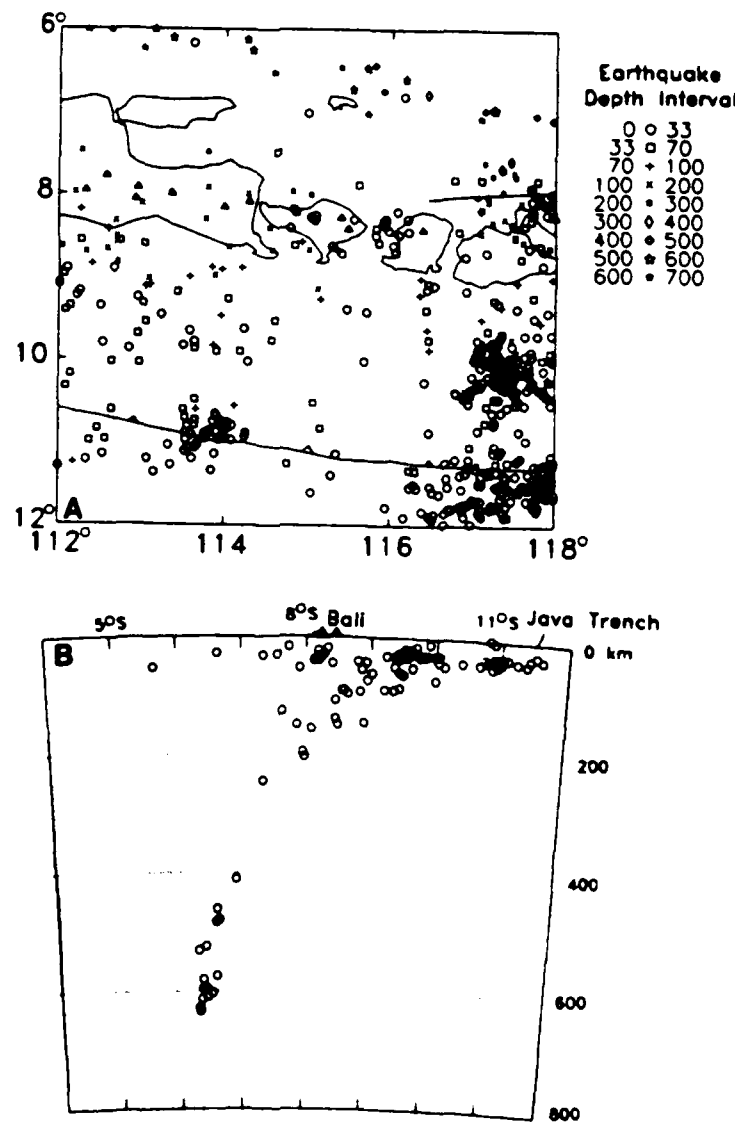
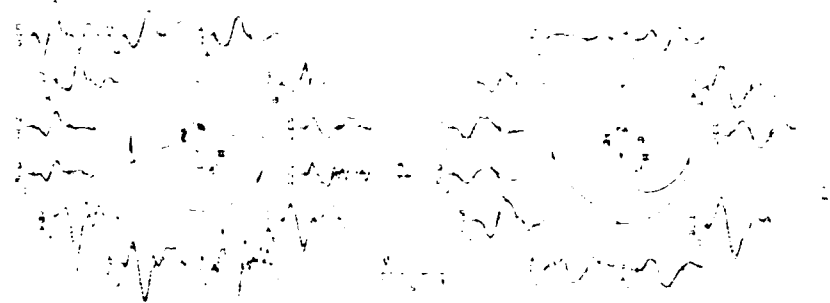
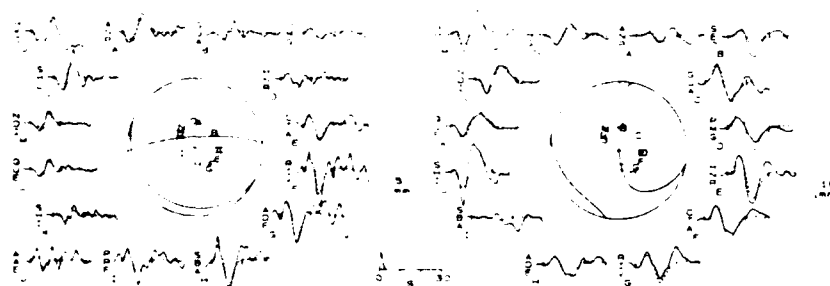


FIGURE 5

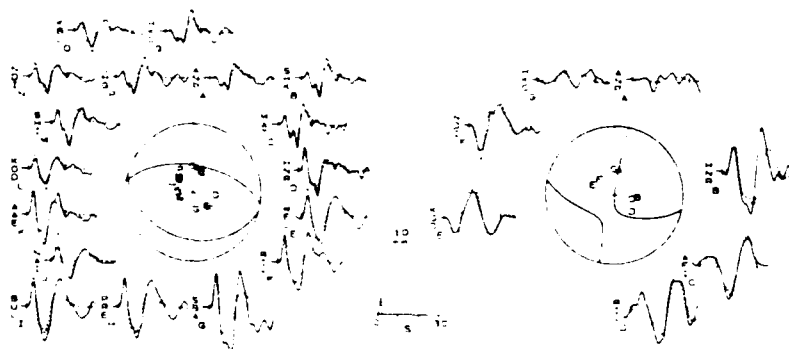
(1) 18 May 1963



(2) 22 May 1963



(3) 14 July 1976



(4) 14 July 1976

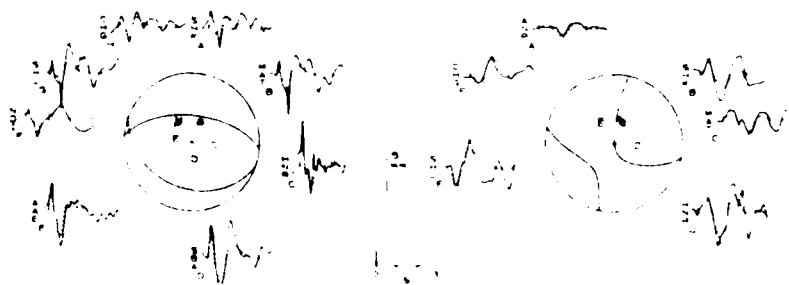
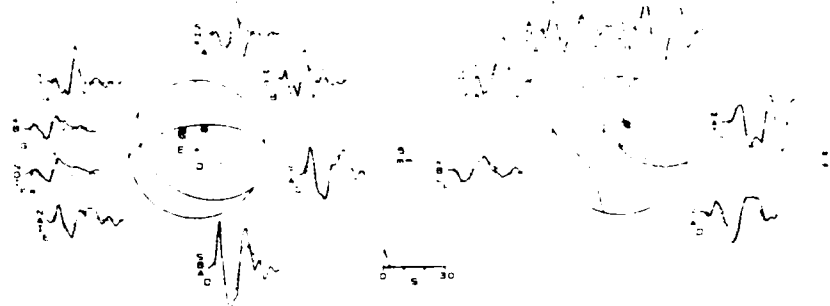
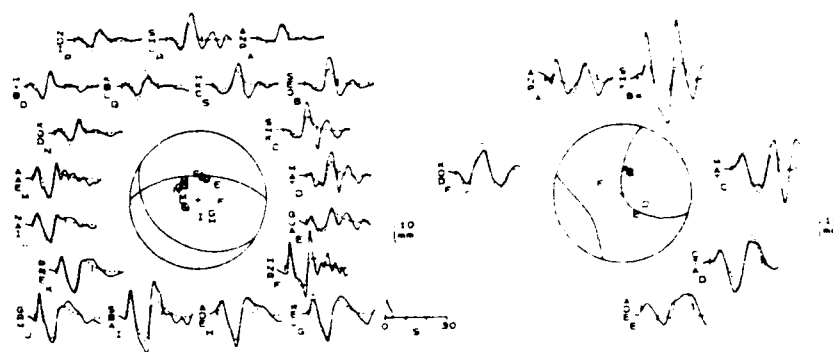


Fig. 6. Plots of waveforms and fault plane solutions for Bali Basin earthquakes. In all plots, observed seismograms are shown by solid lines, and the dashed lines are calculated seismograms. On the left in each plot are the P waves, and on the right are the SH waves. Letters at the lower right of station codes correspond to those in the focal sphere, and an asterisk indicates that the seismogram was not included in the inversion. The small vertical bars enclose the time window used in the inversion. The normalized source time function is shown on the time axis, and the amplitude scale is for seismograms (normalized to an instrument magnification of 3000 and an epicentral distance of 40°).

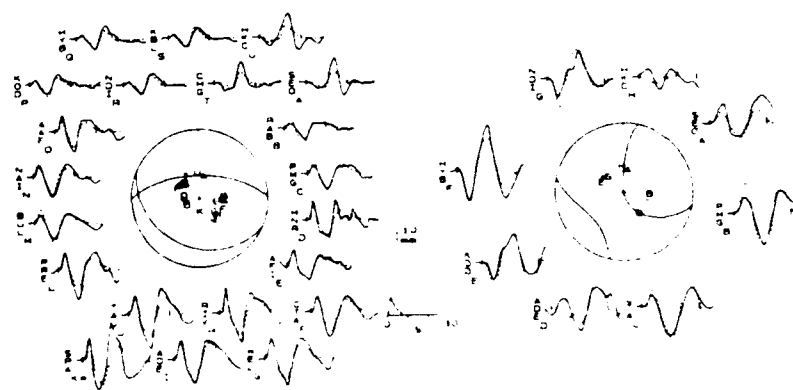
(5) 21 May 1979



(6) 30 May 1979



(7) 20 October 1979



(8) 17 December 1979

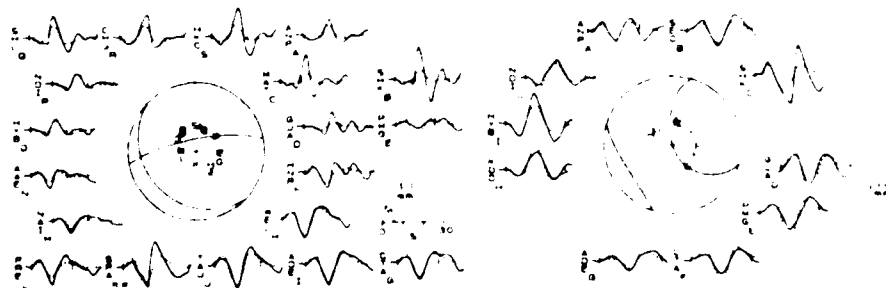


Fig. 6 (continued)

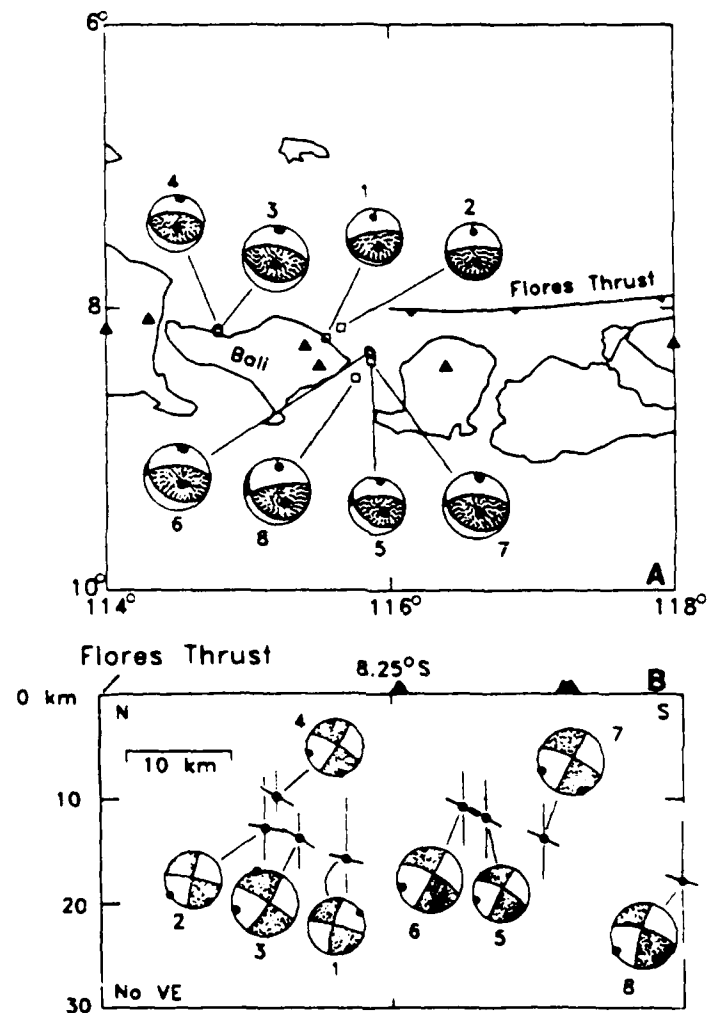


FIGURE 7

(3) 14 July 1976

(4) 14 July 1976 (II)

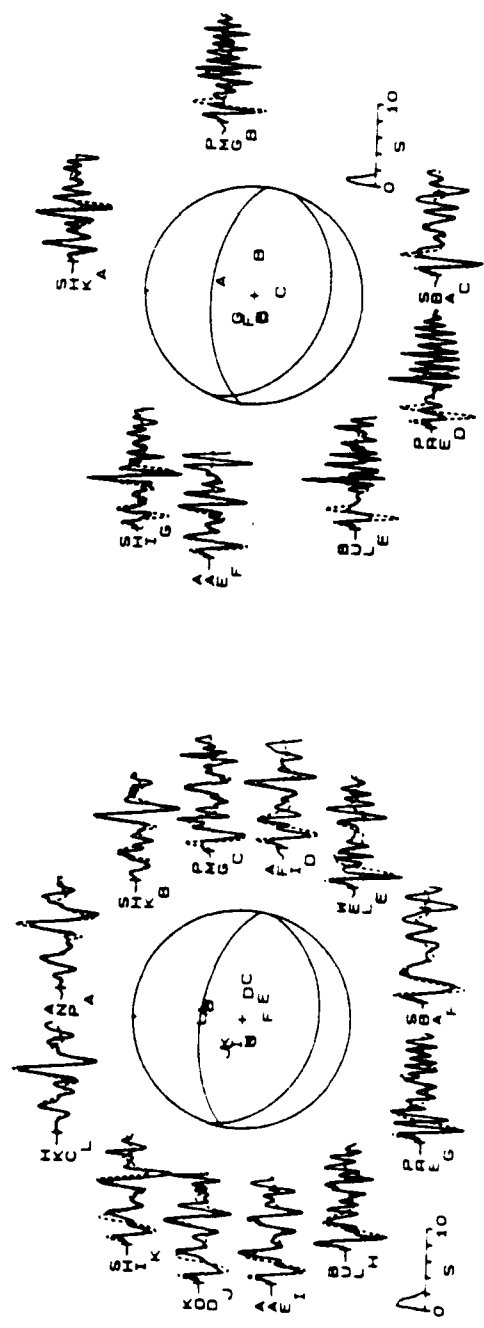


FIGURE 8

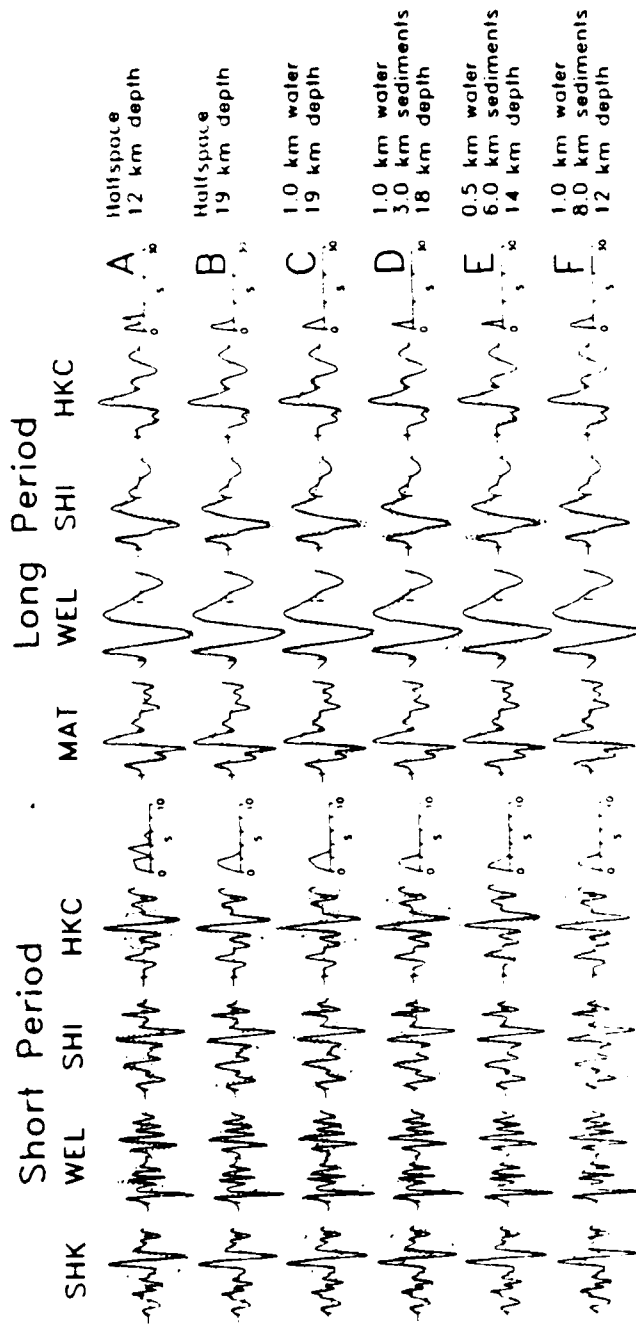
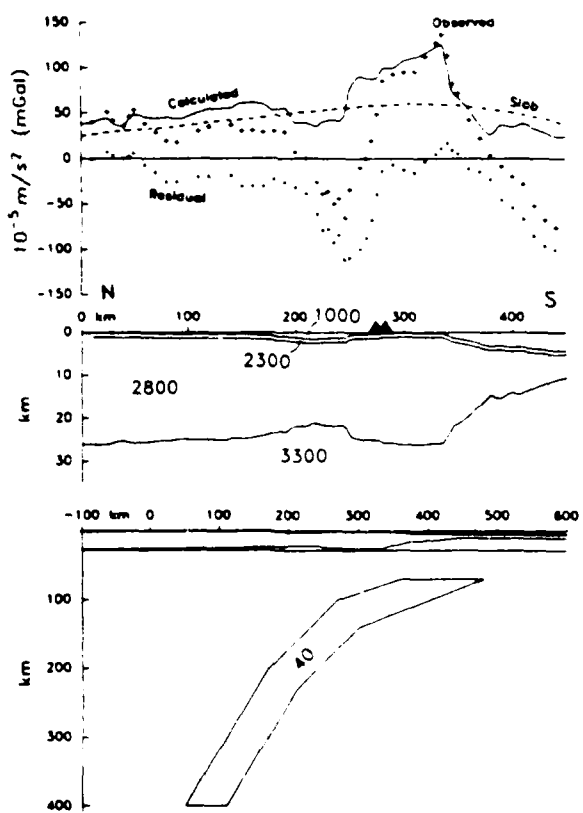


FIGURE 9

**A Line 1 Balanced with slab**



**B Line 67**

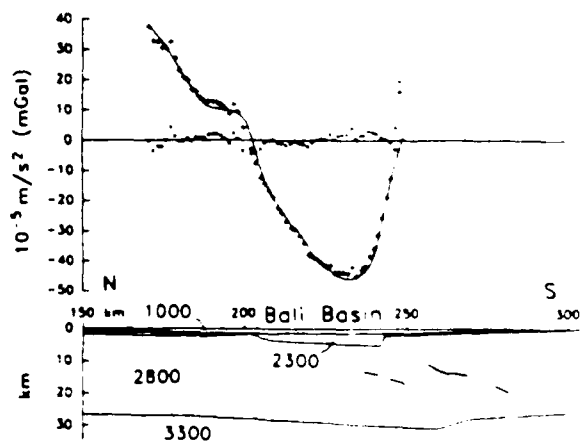


FIGURE 10

A3

	ANP	HNR	SBA	AAE
1	✓	✓	✓	✓
2	✓	✓	✓	✓
3	✓	✓	✓	✓
4	✓	✓	✓	✓
5	✓	✓	✓	✓
6	✓	✓	✓	✓
7	✓	✓	✓	✓
8	✓	✓	✓	✓
9	✓	✓	✓	✓
10	✓	✓	✓	✓
11	✓	✓	✓	✓
12	✓	✓	✓	✓
13	✓	✓	✓	✓
14	✓	✓	✓	✓
15	✓	✓	✓	✓
16	✓	✓	✓	✓
17	✓	✓	✓	✓
18	✓	✓	✓	✓
19	✓	✓	✓	✓
20	✓	✓	✓	✓

A1

140

	ANP	HNR	WEL	AAE
1	✓	✓	✓	✓
2	✓	✓	✓	✓
3	✓	✓	✓	✓
4	✓	✓	✓	✓
5	✓	✓	✓	✓
6	✓	✓	✓	✓
7	✓	✓	✓	✓
8	✓	✓	✓	✓
9	✓	✓	✓	✓
10	✓	✓	✓	✓
11	✓	✓	✓	✓
12	✓	✓	✓	✓
13	✓	✓	✓	✓
14	✓	✓	✓	✓
15	✓	✓	✓	✓
16	✓	✓	✓	✓
17	✓	✓	✓	✓
18	✓	✓	✓	✓
19	✓	✓	✓	✓
20	✓	✓	✓	✓

	ANP	HNR	WEL	AAE
1	✓	✓	✓	✓
2	✓	✓	✓	✓
3	✓	✓	✓	✓
4	✓	✓	✓	✓
5	✓	✓	✓	✓
6	✓	✓	✓	✓
7	✓	✓	✓	✓
8	✓	✓	✓	✓
9	✓	✓	✓	✓
10	✓	✓	✓	✓
11	✓	✓	✓	✓
12	✓	✓	✓	✓
13	✓	✓	✓	✓
14	✓	✓	✓	✓
15	✓	✓	✓	✓
16	✓	✓	✓	✓
17	✓	✓	✓	✓
18	✓	✓	✓	✓
19	✓	✓	✓	✓
20	✓	✓	✓	✓

A2

140

A4

CHG P HKC P ANP SH KOD SH HKC SH

Strike Normalized Variance Depth Dip Rate Moment

249 1.27 13 57 97 682

259 1.16 13 58 92 689

269 1.05 13 58 88 693

279 1.00 14 58 87 694

289 1.03 14 57 85 678

299 1.13 14 57 81 658

309 1.24 15 56 75 645

MAT P CHG P HKC P AFI SH KOD SH

Dip Normalized Variance Depth Strike Rate Moment

048 1.67 15 286 89 639

053 1.16 14 282 88 703

058 1.00 14 279 87 694

063 1.16 13 278 87 625

068 1.49 13 278 88 544

HNR P AAE P ANP SH HNR SH KOD SH

Rate Normalized Variance Depth Strike Dip Moment

057 1.50 15 292 58 663

067 1.24 14 286 58 686

077 1.07 14 279 58 699

087 1.00 14 279 58 694

097 1.04 13 277 58 676

107 1.18 13 274 58 653

117 1.39 13 267 58 632

A5

A6

A7

1985-1986 AFGL-SCEEE GEOPHYSICS SCHOLAR PROGRAM

Sponsored by the

AIR FORCE GEOPHYSICS LABORATORY

Conducted by the

THE SOUTHEASTERN CENTER FOR ELECTRICAL ENGINEERING EDUCATION

FINAL REPORT

THE\_SCRIBE\_PROGRAM:\_AN\_OVERVIEW

Prepared by Dr. George F. Tucker

Research Location: THE AIR FORCE GEOPHYSICS LABORATORY,  
OPTICAL PHYSICS DIVISION

AFGL Research Contact: Dr. George Vanasse

Date: October 31, 1986

Contract No: F19620-83-C-0097

THE SCRIBE PROGRAM: An Overview

by

George F. Tucker

ABSTRACT

An overview is presented of the stratospheric cryogenic interferometer balloon experiment (SCRIBE). This program is designed to yield high resolution emission spectra of the earth's atmosphere. The program's history is briefly summarized. The data encoding and transmission schemes employed are described and the procedures used for data reduction are detailed. The results of data analysis performed by groups at the University of Denver, the University of Massachusetts, and the Air Force Geophysics Laboratory are reviewed. A bibliography of all SCRIBE related publications and tables of the processed spectra produced by the instrument are included.

Acknowledgements

The author thanks the Air Force Geophysics Laboratory and the Southeastern Center for Electrical Engineering Education for the opportunity to engage in this research. Dr. George Vanasse my technical focal point at the AFGL, who is the creator and principal investigator of the SCRIBE program, provided valuable guidance in many areas of the work.

Thanks are also given to: Dr. Hajime Sakai, University of Massachusetts; Dr. Aaron Goldman and Dr. Frank J. Murcay, University of Denver; Mr. Charles Eastman, Stewart Radiance Laboratory; and Mr. William Gallery, Optometrics Incorporated. All of whom have cooperated in this endeavor in the true spirit of scientific research.

## THE SCRIBE PROGRAM: AN OVERVIEW

### Introduction

The STRATOSPHERIC CRYONIC INTERFEROMETER BALLOON EXPERIMENT is an on-going project of the Optical Physics Division of the Air Force Geophysics Laboratory whose goal is to obtain high resolution atmospheric emission spectra at up to 40 km altitudes. These measurements are of importance to the Air Force because the emission characteristics of the stratosphere must be considered in the design of surveillance systems which look at targets through the stratosphere or against a stratospheric background. In addition to its military importance, the SCRIBE data may be used to help answer a variety of environmental questions relating to the role anthropogenic trace gases play in the photochemistry of the atmosphere and their effect on the earth's radiation budget.

Initial design of the SCRIBE instrument began in the mid-1970's with flights starting in 1980 and continuing until the present. During the course of this work data reduction and analysis have been performed by several groups, using similar although not identical methods. Their results have not been collected in one document and no updated overview of the SCRIBE program exists. Because of the uniqueness of the SCRIBE measurements and the increased interest shown in them by researchers, this report was prepared to provide such an overview. It is hoped that it will serve to acquaint potential researchers with the program and the data which it has generated and to provide current investigators with a quick reference to the SCRIBE program.

### The SCRIBE Instrument

SCRIBE is a balloon launched Fourier transform spectrometer (FTS) operated at liquid nitrogen temperature. Optical alignment over a wide temperature range was accomplished by choosing a cat's eye interferometer optical system and fabricating all mechanical parts from the same low expansion coefficient material. Mirror position is determined by a mechanical transducer and HeNe laser fringes. The length of travel of the moving mirror is five cm. The FTS is mounted in a large dewar equipped with an uncooled ZnSe window of low emissivity. The entire dewar is tipped to allow viewing from about -5 degrees to +5 degrees about horizontal. A flat mirror can be inserted for nadir viewing and an ambient temperature blackbody can also be inserted to aid in calibration. A gold doped germanium detector operated at liquid helium temperature is employed. The detector signal is sampled by a 12-bit analog to digital converter whose output, along with a variety of housekeeping signals is fed to a custom pulse code modulation (PCM) encoder. The PCM encoder generates a 72-bit frame at a rate of  $10^4$  frames per second. The data is relayed to a ground station via an S-band telemetry link. The exact form of the PCM stream will be considered in more detail in the discussion on data reduction. The preceding discussion applies to the instrument as it was flown in 1983, modifications for a specific flight are described in the next section.

### Program History

In 1973 at the initiation of Dr. George Vanasse, AFGL entered into a contract with James L. Pritchard of Idealab, Inc. for the development of a cryogenically-cooled

interferometer. At the conclusion of this contract in 1976, the basic SCRIBE interferometer as it exists today had been constructed [10,11]. In its initial form the interferometer utilized a  $\text{LN}_2$  cooled HgCdTe detector and needed major modifications before it could be flown. Under a contract from AFGL the Department of Physics of the University of Denver undertook the tasks of making SCRIBE flight ready and conducting a flight program [5]. Among the modifications they made were; replacing the HgCdTe detector with a liquid helium cooled HgGe detector; interfacing the A/D converter and PCM encoder; repacking all electronics to ensure survival at 40km.; mounting the dewar in a gondola with provisions for tilting the dewar and introducing a mirror or blackbody into the field of view. On October 8, 1980 SCRIBE was flown for the first time for Holloman Air Force Base in New Mexico. Unfortunately, problems with the interferometer's drive and loss of laser fringes limited the data obtained to a few noisy spectrum taken at low altitude. The instrument was flown again on October 7, 1981 [17] and June 16, 1982 but in each case problems limited the value of the measurements obtained [6]. However, these three flights served to demonstrate the potential of the interferometer [13,14,20] and served to point out flaws in the system which were subsequently corrected [12].

On October 23, 1983 the SCRIBE instrument as described in the previous section was successfully flown from Holloman AFB, New Mexico [7]. All systems worked well during the ascent and float altitude ( 29 km) was reached at 0750 MDT. At some point the balloon developed a leak and after 30 minutes at float began to descend. While at float, a series of scans at various look angles along with blackbody measurements were obtained. During the descent a series of nadir viewing scans were taken. The flight was terminated when the balloon descended to 18 km.

Based on the results of this flight an optical filter was added to the optical path, reducing source noise from the strong 15 micrometer  $\text{CO}_2$  band and resulting in improved performance in the higher wavenumber region. This instrument was flown from Roswell, Texas on July 5, 1984 and reached float altitude (30.8 km) at 0745 MDT [9]. All systems worked extremely well with the only problem being strong winds at float which limited the time the balloon was in telemetry range. Good data was obtained on ascent and for approximately 1 1/2 hours at float.

After the 1984 flight the primary goal of obtaining high resolution atmospheric emission spectra at a variety of observation angles had been accomplished and it was now possible to plan flights designed to make measurements of specific compounds which are thought to play key roles in atmospheric photochemistry. The initial compound to be studies was  $\text{N}_2\text{O}_5$ , whose presence is predicted as a result of reactions between  $\text{NO}_x$  and ozone. The interferometer was optimized for the  $1250 \text{ cm}^{-1}$  spectral region where  $\text{N}_2\text{O}_5$  has a major band and was launched on June 21, 1985 at 0255 MDT in order to be at float just before dawn when the  $\text{N}_2\text{O}_5$  was predicted to peak [9]. An unexpected wind change (just after inflation began) made for a difficult launching. Just after release the payload struck the ground causing a loss of command and balloon control links. As a result, instrument elevation angle and detector bias could not be changed and the data from this flight was severely degraded [4].

After this flight, major modifications were undertaken to narrow the field of view of the instrument, provide better control of the viewing angle, and visually verify the emission source. This was accomplished by adding an uncooled telescope and ground controlled steering mirror to the optical path and adding a bore-sighted television camera

to the system. An operator viewing a television monitor could control the view by manipulating a joystick. The new system designated SCRIBE-99 was successfully flown on August 10, 1986. The balloon was launched at 0700 MDT and reached a float altitude of 76 kft. All systems operated successfully and a large number of horizontal and nadir scans were acquired.

Plans for future flights are being developed, with a high priority being given to a flight plan similar to the 1985 flight.

#### DATA REDUCTION

Because the large volume and high acquisition rate of data by the SCRIBE instrument exceeds the capabilities of flight qualified tape recorders, an S-band telemetry link to a ground recording station is employed. The analog output of the detector preamplifier is fed through a 12-bit analog to digital converter whose output is sampled by a custom built PCM encoder. An interface between the A/D converter and the encoder is necessary because the time required between interferogram samples is slower than the rate at which the encoder outputs its data words. Since it is crucial that a sample not be repeatedly transmitted, a signal from the encoder clears the A/D outputs and sets a data valid bit to zero. Any frames sent before a new measurement is made contain 12 zero data bits. When a new measurement is made the data valid bit is reset to one. The 12-bit interferogram sample is combined with four status bits to form a 16-bit word. Bit 13 is tied to ground, bit 14 shows drive direction (1; forward), bit 15 indicates the detector amplifier gain (1; high gain) and bit 16 indicates if the data is valid (1;valid). The PCM encoder generates

72-bit frames at a rate of approximately  $10^4$  frames/sec. Each frame consists of two 8-bit sync words, an 8-bit counter, the 16-bit interferogram/status word, two 8-bit words indicating carriage position and speed, and two 8-bit words containing auxiliary data. Because the auxiliary measurements do not require as high a sampling rate as the interferometer, they are commutated, allowing 30 data channels to be sampled at a rate of 700 samples per second. Among the measurements on these channels are detector impedance, amplifier gain, laser fringe amplitude, various internal and external temperatures, elevation angle, altitude (pressure), and instrument azimuthal position. Other data was recorded on these channels but it varied from flight to flight. The University of Denver group has the channel assignments as well as the calibration data which allows these digital signals to be interpreted. On the ground the telemetry signal after passing through a bit synchronizer is recorded, along with millisecond resolution time code (IRIGB) data on analog 1/2" magnetic tapes at a speed of 60 ips. Simultaneously the output of a parallel bit synchronizer is directed to a University of Denver Nova 1200 computer acting as a decommutator, where the interferogram words are culled from the data stream, redundant samples discarded, and the resulting interferograms are formatted and stored on digital magnetic tapes. Generally at least two ground stations make analog recording of each flight, but only one digital recording is done. Ground radar stations also record the balloon's X, Y, Z coordinates and radiosondes are flown to provide supporting meteorological data. The reduced radar and sonde data are archived at AFGL.

In the case of the digital tapes, several operations must be performed before they can be transformed into

spectra. First the interferograms must be corrected for gain changes that occur during and between scans. These changes are necessary because of the widely varying radiance levels observed and the limited resolution of the 12-bit A/D converter. The first gain change occurs in each interferogram at approximately 800 points where the gain is increased by a factor of 10.91 to allow the region beyond zero path difference to be sampled at a reasonable resolution. During the flight, the peak amplitude of each interferogram is monitored. If the signal falls outside the optimum range the gain is automatically adjusted up or down by a factor of 2 as required before the next scan is performed. These gain changes are recorded as one of the auxiliary data channels on PCM encoder. Finally, whenever the instrument views the blackbody or the nadir, the gain is reduced by changing the detector bias by a factor of 2.1.

After the gain corrections are made, a spike detector and removal program is run. This is necessary because occasionally a few spurious points far the above the normal signal levels are seen. They are believed to be due to an electrical problem in the payload. The removal program interpolates new values at these points. In some cases a channel spectrum caused by the window is present and must be removed in a similar manner. Next a program is run which phase corrects the interferogram. A fast Fourier transform is done to produce a spectrum. The blackbody spectra can be used to generate an instrument function, which when applied to the spectrum, yields a calibrated spectrum. Using this method the University of Denver group has processed selected spectra from the 1983 and 1984 flight. From the 1983 flight a series of co-added nadir spectra were produced (Table 1) and from the 1984 flight four sets of co-added spectra taken

at the elevation angles of 1.9, -3.2, -3.7 and -90.0 degrees while the balloon was at float were obtained.

The analog tapes must be played on a tape recorder, whose output is fed to a decommutator. After this step, the resulting digital data can be treated as described above but with the added feature that the housekeeping channels are also available. Unfortunately, in practice, the process of recording and playing back the analog tapes has created major problems for several of the investigators. Dr. Sakai's group at the University of Massachusetts, Amherst Astronomy Research Facility, using a custom built decomutator encountered problems due to the low signal levels and variations in the speeds of the recording and playing tape recorders. Although these caused significant delays this group produced a number of calibrated spectrum from the 1983 flight (Table 2), of which a representative sample are stored at AFGL (Table 3) [16]. However, because of these problems no nadir views were processed. A number of spectra were also produced from the 1984 flight (Table 4) but because of an unexplained modulation in the blackbody spectra, no calibration was performed [19]. AFGL has a number of these spectra on file (Table 5). Plans are underway to archive all the spectra in Tables 1 and 4 at AFGL. For a complete discussion of the University of Massachusetts effort, see references [12-19].

At AFGL, work has been directed toward reducing both the digital and analog tapes in house. Working with OptiMetrics, Inc. and Stewart Radiance Laboratory, programs have been developed to cull the data, correct the gain and remove spikes. Phase correction, Fourier transform and blackbody calibration programs similar to those used by Dr. Sakai have also been implemented. Great difficulty was encountered in processing the analog tapes. After

considerable effort this was traced to a faculty playback tape recorder which was repaired. Presently high quality digital tapes can be produced and all the necessary programs for producing finished spectra exist. All that remains is to integrate all the programs to allow batch processing of the large volume of data produced by the SCRIBE program.

#### DATA ANALYSIS

Although data reduction has accounted for most of the effort to date, data analysis has resulted in several interesting results.

Dr. Sakai's group found features due to  $\text{CO}_2$ ,  $\text{O}_3$ ,  $\text{HNO}_3$ ,  $\text{H}_2\text{O}$  and  $\text{N}_2\text{O}$  in the 1983 spectra [16]. The Q branch of the  $\nu_2$  band of  $\text{CO}_2$  at  $667 \text{ cm}^{-1}$ , which is very opaque, was used by them to measure temperature in the vicinity of the balloon. The values obtained were about 10 K higher than those measured in a less opaque spectral region for the atmosphere at a similar altitude some distance from the instruments. They attributed this discrepancy to a mass of warm air carried along with the balloon on its ascent. The  $\text{HNO}_3$  features were identified as  $\nu_5$  and  $2\nu_9$  bands. These bands showed maximum emission for an elevation angle with a tangent height of 20 km, indicating that the concentration of  $\text{HNO}_3$  is a maximum around the tropopause. By a similar analysis it was concluded that the majority of the  $\text{O}_3$  observed occurred below 30 km. They also compared that SCRIBE spectra to synthetic spectra generated from the AFGL line computation.

The University of Denver group performed a similar analysis [7] and in addition to the aforementioned molecules also identified features due  $\text{CFCl}_3$  (freon 11) and  $\text{CF}_2\text{Cl}_2$  (freon 12). They also obtained a laboratory absorption

spectrum of  $\text{HNO}_3$ . By comparing this spectrum with the SCRIBE data, the assignment of  $\text{HNO}_3$  features in the SCRIBE spectra was verified. In addition, the laboratory spectrum was used to confirm that the resolution of the SCRIBE interferometer is  $0.06 \text{ cm}^{-1}$  (FWHM). They concluded that the instrument has sufficient sensitivity to measure atmospheric emission at high altitudes at its full resolution. Also at the University of Denver, Dr. Aaron Goldman prepared comparisons of simulated and SCRIBE spectra [3]. He found generally good agreement of his model with the observed radiance, but noted major inadequacies in the  $830 \text{ cm}^{-1}$  window region.

Dr. Goldman has also prepared similar comparisons for the 1984 flight [1,2]. These comparisons were made for elevation angles of 1.9, -3.2, -3.7 and 90.0 degrees while the interferometer was at float. Again reasonable agreement was found but a number of adjustments to the model were necessary before this could be accomplished.

Dr. Lawrence Rothman of AFGL has compared 1983 downlooking spectra obtained at 61, 70, 81 and 88 kft with synthetic spectra generated by the FASCODE modeling program from the AFGL line parameter file. Preliminary results indicate that there is a major discrepancy between the spectra in the region of the  $\text{CO}_2 \nu_2$  Q branch at  $667 \text{ cm}^{-1}$ . This discrepancy is not yet understood and additional analysis is being undertaken with a more complete set of spectra.

At present, a more detailed analysis of the 1983 and 1984 data is being undertaken by personnel from the AFGL and OPTiMetrics, Inc. As a first step, an atlas of the spectra shown in Tables 2 and 5 is being prepared. The entire

wavelength region of each spectrum is plotted at  $1\text{ cm}^{-1}$  resolution, and the opaque region around  $667\text{ cm}^{-1}$  and the window region around  $810\text{ cm}^{-1}$  are plotted at  $0.06\text{ cm}^{-1}$  resolution. Also modifications to the FASCOD2 computer model are being done to allow it to be more easily used in comparisons with the SCRIBE data.

The University of Denver and AFGL are also beginning to analyze the 1986 data but no results are currently available. This analysis will initially focus on the effect of the uncooled telescope on quality of the data obtained.

The bibliography that follows includes all the publications concerning SCRIBE on file at AFGL. The reader is referred to them for detailed descriptions of the various aspects of the program.

SCRIBE Bibliography,

1. Goldman, A. Cold Interferometer July 5 1984 Flight  
Scientific Report, Dept. of Physics, U. of  
Denver, Denver, CO., (1985)
2. Goldman, A., Preliminary Qualitative Comparison of  
Calculated and Experimental Cold Interferometer  
Spectra, Scientific Report, Dept of Physics, U. of  
Denver, Denver CO., (1985)
3. Goldman, A. Atmospheric Radiance in the 8.6 -13.6  
Micrometer Region-an Update, Scientific Report, Dept of  
Physics, U. of Denver, Denver CO.,(1986)
4. Ground, J.E., 21 June 1985, private communication.
5. Murcray, F. H., Murcray F. J., Murcray D. G., and  
Williams, W. J., Stratospheric Cryogenic Infrared  
Balloon Experiment, Air Force Geophysics Laboratory,  
Hanscom AFB, MA, AFGL-TR-81-0186, AD-A104 168 (1981)
6. Murcray, F. H. and Murcray F. J., Balloon-Borne  
Cryogenically Cooled Interferometer System, Air  
Force Geophysics Laboratory, Hanscom AFB, MA., (1983)
7. Murcray, F.H., Murcray F. J., Murcray D. G., Prichard  
J., Vanasse G. and Sakai H., Liquid Nitrogen Cooled  
Fourier Transform Spectrometer System for Measuring  
Atmospheric Emission At High Altitudes, J. Atm. and  
Oceanic Tech., 1.,351-357, AD-A152 451 (1984)
8. Murcray, D. G., Murcray F. H., Murcray F. J. and Vanasse  
G., Measurements of Atmospheric Emission at High  
Spectral Resolution, J. of Met. Soc. Japan, 53, 321-  
324, AD-A159 338 (1985)
9. Murcray, F.H., Murcray F. J., Murcray D. G., and Edman  
A, Measurement of Atmospheric Emission Spectra at High  
Altitudes, Air Force Geophysics Laboratory, Hanscom  
AFB, MA, AFGL-TR 81-0181, AD-A104 168 (1981)

12. Sakai, H., SCRIBE I DATA ANALYSIS Air Force Geophysics Laboratory, Hanscom AFB, MA, AFGL-TR-81-0129, AD-A102 262 (1981)
13. Sakai, H., Li, T. C., Pritchard, J., Murcray, F. J., Murcray, F. H., Williams, J. and Vanasse, G. Measurement of Atmospheric Emission using a Balloon-Borne Cryogenic Fourier Spectrometer SPIE Publ. 289, 196-198, AD-A111 343 (1981)
14. Sakai, H., Barowy, W., Pulchtopek, S., Pritchard, J., Murcray, F. J., Murcray, F. H. and Vanasse G., Study of Atmospheric Infrared Emission Using a Balloon-Borne Cryogenic Fourier Spectrometer, SPIE Publ. 364, 38-45, (1982)
15. Sakai, H., and Vanasse, G., SCRIBE II DATA ANALYSIS, Air Force Geophysics Laboratory, Hanscom AFB, MA, AFGL-TR-82-0150, AD-A116 250 (1982)
16. Sakai, H., and G. Vanasse, SCRIBE Data of October 23, 1983, Air Force Geophysics Laboratory, Hanscom AFB, Ma., AFGL-TR-84-0208, AD-A154 862 (1983)
17. Sakai, H. and Vanasse, G., Atmospheric Infrared Emission Observed at Altitude of 27000 to 28000 m, SPIE Publ. 366, 165-172, AD-A133 472 (1983)
18. Sakai, H., Vanasse, G., Murcray, F. H. and Murcray, F. J., Detector-Nose-Limited Sensitivity of Fourier Spectroscopy Plus Stratospheric Emission Measurements and Observed Trace Gas Spectra, Proceeding of the 13th Congress of the International Commission for Optics, 550-551, (1984)
19. Sakai, H., Processing of Scribe Data, Air Force Geophysics Laboratory, Hanscom AFB, MA, AFGL-TR-85-0279, AD-A165 226 (1985)
20. Vanasse, G. A., Stratospheric Cryogenic Interferometer Balloon Experiment (SCRIBE), Air Force Geophysics Laboratory, Hanscom AFB, MA, AFGL-TR-81-0048, AD-A100 718 (1981)

21. Vanasse, G. A., Murcray, D. G., Murcray, F. H., and Murcray, F. J., Fourier and Computerized Infrared Spectroscopy, SPIE Publ. 553, 425-426, (1985)
22. Vanasse, G. A., Murcray, D. G., Murcray, F. H. and Murcray, F. J., SCRIBE Interferometer Atmospheric Emission Spectra, Proceeding of the 5th General Assembly of the International Association of Geomagnetism and Aeronomy 2,430,(1985)

Table 1. Co-Added Spectra From the October 23, 1983 SCRIBE Flight

File Name	Co-Added Files	Altitude (kft)
den. 1	Tape 4 Files 86, 87, 88, 90, 91, 92	90.5
den. 2	Tape 5 Files 2, 3, 4, 5, 6, 7, 8, 9	87.7
den. 3	Tape 5 Files 10, 11, 12, 13, 14, 15, 16, 17	86.3
den. 4	Tape 5 Files 18, 19, 20, 21, 22, 23, 24, 26	85.5
den. 5	Tape 5 Files 27, 28, 29, 30, 32, 33, 35, 36	84.3
den. 6	Tape 5 Files 37, 38, 39, 40, 41, 42, 43, 44	82.3
den. 7	Tape 5 Files 45, 46, 47, 48, 49, 50, 51, 52	80.8
den. 8	Tape 5 Files 53, 55, 56, 57, 58, 61, 62, 63	78.4
den. 9	Tape 5 Files 64, 66, 67, 68, 69, 61, 72, 73	75.0
den.10	Tape 5 Files 74, 75, 76, 77, 78, 79, 80, 81	70.0
den.11	Tape 6 Files 2, 3, 4, 5, 6, 7, 8, 9	61.0

Notes:

1. All spectra are Nadir views.
2. The resolution of all spectra is  $0.24 \text{ cm}^{-1}$  FWHM.
3. A blackbody calibration was applied to all spectra.
4. All spectra were processed by the University of Denver and the co-added file numbers are their designation.
5. Altitudes are approximate because the balloon was descending during this period.
6. The spectra are archived on magnetic tape and floppy disk at the AFGL.

Table 2. Calibrated Spectra Processed by the University of Massachusetts, Amherst from the October 23, 1983 SCRIBE Flight.

File Names	Time (GMT)	Altitude (kft)	Elevation Angle (degrees)	View
SP830A1-A7	12:16	10	7.5	Horizontal
M1-M7	12:20	20	7.5	Horizontal
N1-N7	12:25	25	7.5	Horizontal
O1-O7	12:30	30	7.5	Horizontal
11-17	13:15	70	1.7	Horizontal
21-27	13:45	95	-90.0	Nadir
V1-V7	13:50	95	-90.0	Nadir
W1-W7	13:54	95	-90.0	Nadir
B1-B7	14:00	95	-90.0	Nadir
C1-C7	14:05	95	-90.0	Nadir
D1-D7	14:08	95	-90.0	Nadir
31-37	14:13	95	-0.4	Horizontal
E1-E7	14:17	95	-0.4	Horizontal
F1-F7	14:20	95	-0.4	Horizontal
G1-G7	14:24	95	*-0.4/2.9	Horizontal
H1-H7	14:27	95	-2.9	Horizontal
I1-I7	14:30	95	-2.9	Horizontal
J1-J7	14:33	95	*-2.9/-5.4	Horizontal
K1-K7	14:37	95	-5.4	Horizontal
L1-L7	14:40	95	-5.4	Horizontal
41-47	14:45	95	-5.4	Horizontal
61-67	14:48	95	-5.4	Horizontal
71-77	14:53	95	-	Black Body
81-87	14:55	95	-	Black Body
91-97	15:02	95	7.5	Horizontal
P1-P7	15:06	95	*7.5/-90.0	H/N
Q1-Q7	15:10	95	-90.0	Nadir
R1-R7	15:15	90	-90.0	Nadir
S1-S7	15:18	90	-90.0	Nadir
T1-T7	15:22	90	-90.0	Nadir
U1-U7	15:25	90	-90.0	Nadir

Notes:

1. Resolution of all scans is  $0.06 \text{ cm}^{-1}$  /FWHM.
2. \* Indicates the quantity changes during the interval.
3. A Blackbody calibration was applied to all spectra.
4. Times are approximate.
5. These files are stored on magnetic tape at the University of Massachusetts, Amherst.

Table 3. Tape FTHY06: Calibrated Spectra from the October 23, 1983 SCRIBE Flight.

File Name	Time (GMT)	Altitude (kft)	Elevation Angle (deg)	View
SP830M4	12:20	20	7.5	Horizontal
N1	12:25	25	7.5	Horizontal
O1	12:30	30	7.5	Horizontal
V3	13:50	95	-90.0	Nadir
W1	13:54	95	-90.0	Nadir
B1-B7	14:00	95	-90.0	Nadir
C1-C5	14:05	95	-90.0	Nadir
D1	14:08	95	-90.0	Nadir
31,36	14:13	95	-0.4	Horizontal
E1	14:17	95	-0.4	Horizontal
F6	14:20	95	-0.4	Horizontal
G1-G3	14:24	95	*-0.4/-2.9	Horizontal
H1-H2	14:27	95	-2.9	Horizontal
I1,I2	14:30	95	-2.9	Horizontal
J2,J7	14:33	95	*-2.9/-5.4	Horizontal
K3-K7	14:37	95	-5.4	Horizontal
L1,L2	14:40	95	-5.4	Horizontal
41-47	14:45	95	-5.4	Horizontal
95.97	15:02	95	7.5	Horizontal
P1,P3	15:06	95	*7.5/90.0	Nadir
Q1	15:10	95	-90.0	Nadir

Notes:

1. Resolution of all scans is  $0.06 \text{ cm}^{-1}$  /FWHM.
2. \* Indicates the quantity changes during the interval.
3. A Blackbody calibration was applied to all spectra.
4. Times are approximate.
5. These files were prepared by Dr. Sakai at the University of Massachusetts, Amherst and are stored on magnetic tape at AFGL

Table 4. Uncalibrated Spectra Processed for the University of Massachusetts, Amherst from the July 5, 1984 SCRIBE Flight

Time (GMT)	File Names	Elevation Angle (deg)	Gain	Bias
12:21-12:22	MI-MK	4.9	1	2.1
12:24-12:33	QE,QF,QL,PE QJ,QK,PF,PC	4.9	2	2.1
12:50-13:45	KA-KL,LA-LI, LK,LL,MA,MB, ME,HI,HK,HL, IA-IL,JA-JL	1.9	2	2.1
13:58-14:05	GA,GB,GD-GJ	-0.6	2	2.1
14:10-14:35	HA-HH,TA-TH, UA-UH	-3.2	1	2.1
14:47-14:58	AA-AL,BA,BB, BD-BF	-3.7	1	2.1
15:06-15:12	DA-DH	-1.2	2	2.1
15:28-15:30	EA-ED	Blackbody	1	1
15:45	RB	-1.2	1	1
15:48	RF	-90.0	2	1
15:50-15:53	RH-RL	-90.0	1/2	1

Notes:

1. Resolution of all scans is  $0.06 \text{ cm}^{-1}$ .
2. No blackbody calibration was performed.
3. These files are stored on magnetic tape at the University of Massachusetts, Amherst.

Table 5. Tape FTHY85: Uncalibrated Spectra from the July 5, 1984 SCRIBE Flight

File Name	GMT	Altitude (kft)	Elev.Ang. (deg)	Gain	Bias
847MJ	12:22	40	4.9	1	2.1
847QA	12:45	60	1.9	1	2.1
847LC	13:01	70	1.9	2	2.1
847HJ	13:21	75	1.9	2	2.1
847IA	13:24	80	1.9	2	2.1
847IK	12:33	85	1.9	2	2.1
847JB	13:36	90	1.9	2	2.1
847JI	13:43	94	1.9	2	2.1
847FA	13:49	100	1.9	2	2.1
847GB	13:58	100	-0.6	2	2.1
847HB	14:11	100	-3.2	2	2.1
8475C[TC]	14:22	100	-3.2	2	2.1
847UC	14:31	100	-3.2	1	2.1
847AC	14:48	100	-3.7	1	2.1
847BF	14:58	100	-1.2	1	2.1
846DC	15:05	100	-1.2	2	2.1

Notes:

1. Resolution of all scans is  $0.06 \text{ cm}^{-1}$ .
2. No blackbody calibration was applied to the spectra.
3. File 8475C[TC] was obtained from a coadd of eight interferograms.
4. These files were prepared by Dr. Sakai at the University of Massachusetts, Amherst and are archived on magnetic tape at AFGL.

Table 6. Interferograms Prepared by the University of Denver from the July 5, 1984

Tape Number	Files	Elevation Angle (deg)	Altitude (kft)	Gain	Bias
1	2-66	4.9	*	1/2	1
1	67-100	4.9	*	1	2.1
1	101-125	4.9	*	2	2.1
2	2-6	4.9	*	2	2.1
2	12-113	1.9	*	2	2.1
3A	2-74	1.9	*	2	2.1
3A	78-112	-0.6	100.3	2	2.1
4A	2-10	-3.2	100.3	2	2.1
4A	11-73	-3.2	100.3	1	2.1
4A	79-98	-3.7	100.3	1	2.1
5A	2-39	-3.7	100.3	1	2.1
5A	43-97	-1.2	100.3	2	2.1
6A	5-7	-1.2	100.3	2	2.1
6A	11-46	Blackbody	100.3	1	1
6A	51-83	-90.0	100.3	1/2	1
6A	87-96	-1.2	*	*	*

Notes:

1. \* indicates the quantity varied during the interval.
2. These interferograms are stored on magnetic tape at AFGL.
3. Files are not listed where the data was questionable, for example, when the interferometer was being moved to a new elevation angle.

1985-1986 AFGL-SCEEE GEOPHYSICS SCHOLAR PROGRAM

Sponsored by the

AIR FORCE GEOPHYSICS LABORATORY

Conducted by the

SOUTHEASTERN CENTER FOR ELECTRICAL ENGINEERING EDUCATION

FINAL REPORT

Simulating Nonperiodic Systems

Prepared by: Earl F. Witt

Academic Department: NA

University: NA

Research Location: Air Force Geophysics Laboratory  
(PHA)

AFGL Research Contact: W. Burke

Date: March 12, 1986

Contract Number: F19628-83-C-0097

Simulating Nonperiodic Systems

by

Earl F. Witt

ABSTRACT

Modifications to the previously created one-dimensional, periodic plasma simulation code are described. These modifications allow simulation of diode-type systems in which the particles are not periodic and various boundary conditions may be imposed on the fields. Particles are injected from reservoirs on either side of the simulation box according to some predetermined Maxwellian distribution function; particles that exit the system on either side are absorbed by that wall. The walls function as capacitor plates: when a particle leaves the wall it leaves behind a charge equal and opposite to its own, and when the particle is absorbed by a wall it contributes its charge to that wall. The potential in the box is determined by Poisson's equation subject to one of three possible boundary conditions: 1) the potential is set equal to zero at both ends, 2) the potential is fixed at zero on the left and a specified value on the right, or 3) the potential is zero on the left and floats on the right. In case 3 the charge in the walls makes a difference. Tests of the nonperiodic part of the simulation code are described.

## I. INTRODUCTION

A plasma simulation with periodic boundary conditions on the fields and particles simulates infinite plane waves in an infinite medium. If one starts one species of particles with a given drift and then lets the system develop, one is watching the decay of an infinite beam as it propagates through the infinite medium. If one is instead interested in the evolution of plasma in one spatial location through which a beam is directed, a nonperiodic system is more appropriate. A nonperiodic system is also useful in modeling various configurations of isolated probes in a surrounding plasma. Since one of the principal interests at this research location is the propagation of beams through plasma, the development of the simulation code was continued so as to allow simulation of nonperiodic systems.

The simulation code, except for the nonperiodic options, is a subset of ES1 (see Birdsall and Langdon, 1985). The momentum conserving, linear weighting code is used without any provision for smoothing of charge densities or fields. As in ES1, field variables are calculated on a grid and linearly interpolated to particle positions. The particles themselves are, in effect, finite width planar charge sheets. In the periodic part of the code, periodic boundary conditions are imposed on both the fields and the particles; when a particle exits one end of the simulation box it is reinserted in the other end with the same speed. One may study propagation of waves at any angle with respect to a uniform magnetic field. Diagnostic data such as electric field profiles, phase space information, and information on particle distribution functions (much the same as in ES1) are written to a separate data file which can be used by separate programs to plot the

diagnostics. One of these programs just plots the data in the order it was written. The other, a postprocessor, can plot any interval of time of history data, and can also make and plot discrete Fourier transforms of these time intervals.

Since the possibility of nonperiodic simulations was always in mind, provisions were made in the original coding to aid in such simulations. In this latest research period, these provisions were used, modified, and expanded. Modifications made to allow for nonperiodic particles, and modifications in calculating the fields in nonperiodic systems are described below.

## II. OBJECTIVES

The objectives of this research effort were:

- 1) To continue development of the one-dimensional, electrostatic simulation code,
- 2) To update the user documentation and educate people in the use of the code,
- 3) To use the code in support of data analysis from beam-plasma experiments.

## III. Nonperiodic Modifications to the Simulation Code

As before, the source code of F1D, as described in Birdsall and Langdon, 1985, and parts of F1W (Lawson, 1984) proved useful as models for one- and two-dimensional codes. The nonperiodic part of the code can be roughly divided into two parts, that dealing with treatment of the particles, and that dealing with calculation of the fields. Below I describe the overall philosophy behind this code, discuss the ideas behind each of the treatments of particles and of the fields, and then I present some of the test calculations of the code. Details of all

of this material are given in the users guide which has been prepared for workers on site.

System: The simulation system may be thought of as a diode with capacitor plates for its two walls. One may think of the plates also as particle guns that leak or direct plasma, pulled from the plates themselves, into the system. The two plates may either be joined by a conductor (short circuit conditions), connected to a battery (fixed potential drop), or left to float (no connection). The picture is complicated somewhat by the option of treating any given species as periodic. In this case, the periodic species sees the system as a toroid; when the particle exits one end, it enters the other end with its velocity unchanged.

Particles: To accommodate the injection of particles, provisions were made for creation of reservoirs from which particles are injected at each time step. The reservoirs are loaded with Maxwellian distributions in the same manner that particles were loaded in the periodic code, and thereafter are not changed; one cycles repeatedly through the list of reservoir velocities as needed to choose the velocities of entering particles. In the reservoirs, particles are sorted into left going and right going particles, and the initial numbers of particles in each of these groups are recorded. One has the option of setting a cutoff number such that if the number of right or left going particles falls below that number, no particles of that group are injected.

Enough particles are injected each timestep to reflect the proper number of entering particles implied by the Maxwellian distribution and the flux density chosen for that particle species. In practice, the flux is

some noninteger number of particles per timestep. If this is left over after particles are deleted, the next timestep will have a different number of particles, etc., after another timestep, etc. In effect, particles are created at random from time to time, and the number between 0 and 1, where 0 is the maximum and 1 is the minimum, is the simulation timestep, and the number of the step in the simulation is present as  $i$ . It is assumed that the elements of the array at the boundary, the last  $i$  elements of the array, will be initialized to zero times the same random number.

It may be seen from the code examples in the end of the chapter that `spcnum` is the max number of particles in the code. The `part` array contains the index of the last `spcnum` particles, and the number of extra spaces reserved for deleted particles in the particle arrays. Logical arrays, certain flags that indicate whether a given location in the particle array is occupied by a simulation particle, and the total number of locations being used is also kept track of. Whenever the number of "dead or excited" particles plus the number of live particles exceeds the space allotted for particles, the arrays are repacked. If at any time more particles need to be inserted than space was allowed for, even after repacking, a note is made of the fact and the simulation terminates.

Tests run on this part of the code indicate that this book keeping works **very well**.

Fields: The first change from the periodic code is in how the charge density is calculated. In both the periodic and nonperiodic codes, the charge due to a particle is linearly distributed between the two neighboring grid points around the particle. In the periodic code, the

charge on the  $N_{\text{grid}} + 1$  grid point is then added to the first grid point, and then the charge on the  $N_{\text{grid}} + 1$  grid point is set equal to that of the first. At each time step, the initial neutralizing charge on grid point  $NRD$ , except on grid points 1 through  $NG$ . In the nonperiodic code, the charge on the  $N_{\text{grid}} + 1$  grid point is kept distinct from that on the first, so the setting of the first and last charges is done in concert. For the left cell on the ends the neutralizing charge is distributed evenly on grid points 1 through  $NG$ , and half that amount is added to grid points 1 and  $NG + 1$ .  $NRD$  is only calculated at the start of the simulation and thereafter remains unchanged.

After the charge density is found, the fields are calculated as follows. If one fixes a potential difference between the first and last grid points, the tridiagonal solver described in appendix B of Birdsall's book (Birdsall and Langdon 1985) is employed. If floating right-hand boundary is assumed, the potential is calculated via a centered difference form of Poisson's equation with the boundary condition that zero charge resides outside grid points 1 and  $NG + 1$ , and that the potential of grid point 1 is zero. The calculation proceeds from left to right. If short circuit boundary conditions are assumed, a linear term is added to the potential at each grid point found from the 'floating' calculation so that the potential of grid point  $NG + 1$  is zero. In all cases, the electric field on the two boundaries is calculated via a two point difference formula, and the electric field within is calculated via a centered difference formula.

Tests: Except for short runs to debug the code, only two types of simulations have been run which might serve as tests of the nonperiodic code. These are 1) an attempt to reproduce simulations run in Chodura

(1982) involving injection of unequal fluxes of electrons and ions through one boundary into an absorbing wall at the other boundary (with no magnetic field present), and 2) a two-stream simulation in which cold electrons of equal density are injected from opposite walls. The intent here is to compare the results of the nonperiodic system to those of the periodic simulation of a similar system.

The results are inconclusive, but, in case 2, promising. In Chodura's simulations a steady state was arrived at in which the potential made a smooth transition from zero at the injection boundary to a negative potential at the absorbing wall. The wall potential depended on a straightforward way on the ratio of the injected fluxes. In simulations run with the present code, no steady state was arrived at even after 2000 plasma periods. Even potential profiles averaged over 4 plasma periods ( 251 time steps) showed no sign of settling down. The wall potentials in the averaged profiles were consistently below (sometimes below half) as much as the theory predicted. It could be the injection scheme that is at fault (too much noise?), or something else.

In the case of the two-stream simulation, the results seem more straightforward. Figures 1-5 show a comparison between diagnostics taken in the periodic case (left column in each Figure) and those taken in the nonperiodic case (right column in each Figure). In both runs, the simulation boxes were initially filled with 128 particles of each species with the following parameters:

$L=2\pi$ ,  $DT=0.2$ ,  $NG=32$  for the system, and  $N=128$ ,  $WP=1.0$ ,  $QM=-1.$ ,  $VO=1.$ , and an initial perturbation of position according to  $x \rightarrow x + 0.01\cos(2*x)$ . Similar behavior is observed in both simulations, with differences that one might expect. For instance, the

mode that was initially excited (mode 2) grows in both cases with about the same growth rate (see Fig. 1). The phase space of right going particles (Fig. 2) and right going particles (Fig. 3) have similar features, and the growth of mode 2 is clearly seen initially. Also the potential and electric fields (Figures 4 and 5) show similar features. However, as can be seen in the phase space diagrams, the symmetry of the periodic phase space pictures between species one and two (right and left going), and for each species individually, is lacking in the nonperiodic diagrams. This is to be expected since the velocity of the nonperiodic particles is clamped to plus or minus one at one boundary. The potential of the nonperiodic simulation eventually deviates from that of the periodic case because of reflection of particles in the box, and absorption of particles by the walls; note that the integral of the potential with respect to position is not zero in the final panel. The general correspondence between these two simulations in the early development, however, leads to the qualitative conclusion that there is good physics represented here. Without a detailed model of what one should expect in the nonperiodic case, however, one cannot make more quantitative statements.

#### IV. Documentation of Code

The users guide has been updated to reflect the new changes, and to describe how to add diagnostics to the code at will. Many comments have been added to the source listings. In addition, several people have been instructed in the use of the code.

## V. Support of Data Analysis

Only one simulation with inconclusive results was run to simulate a beam passing through a plasma. The bulk of the time was occupied with objectives 1 and 2.

## IV. Recommendations

- a) Given the users guide, a copy of the source programs on a floppy disk and on tape, and the instruction of a few people in the use of the code, the simulation code should be readily available and useful after I have left. When the operating system of the local computer changes, some changes may have to be made in the plotting routines; one may wish to do so any way in order to get better graphs. The programs should, however, be useful as they stand.
- b) Better tests should be devised for the existing code. There should be a wealth of literature on the Pierce diode (see Birdsall book for reference or the PDW1 reference guide) from which one might extract useful test simulations. Another possible test would be to calculate the linear evolution of the two stream system pictured in the Figures here, and to compare that evolution with what was seen.
- c) One modification in the particle injection scheme may be worth trying. Instead of randomly locating the incoming particles, a smoother injection scheme would locate the particles at injection sites spaced a distance  $L/N$  apart and travel from the boundary at an average velocity determined by the specified distribution function. In the case of injecting cold particles, sites at intervals of  $L/N$  apart would flow into the simulation box at a speed equal to that of the initial drift. The added complexity might be repaid with a quieter simulation.

ACKNOWLEDGEMENTS

This work was sponsored by the Air Force Geophysics Laboratory, United States Air Force, under Contract F19628-83-C-0097.

REFERENCES

Birdsall, Charles K. and A. Bruce Langdon, Plasma Physics via Computer Simulation, McGraw-Hill Book Company, New York, 1985.

Chodura, R., Plasma-wall transition in an oblique magnetic field, Phys. Fluids, 25, 1628, 1982.

Lawson, W. S., PDW1 User's Manual, Memorandum No. UCB/ERL M84/37, ERL, College of Engineering, University of California, Berkeley, CA 94720, April 1984.

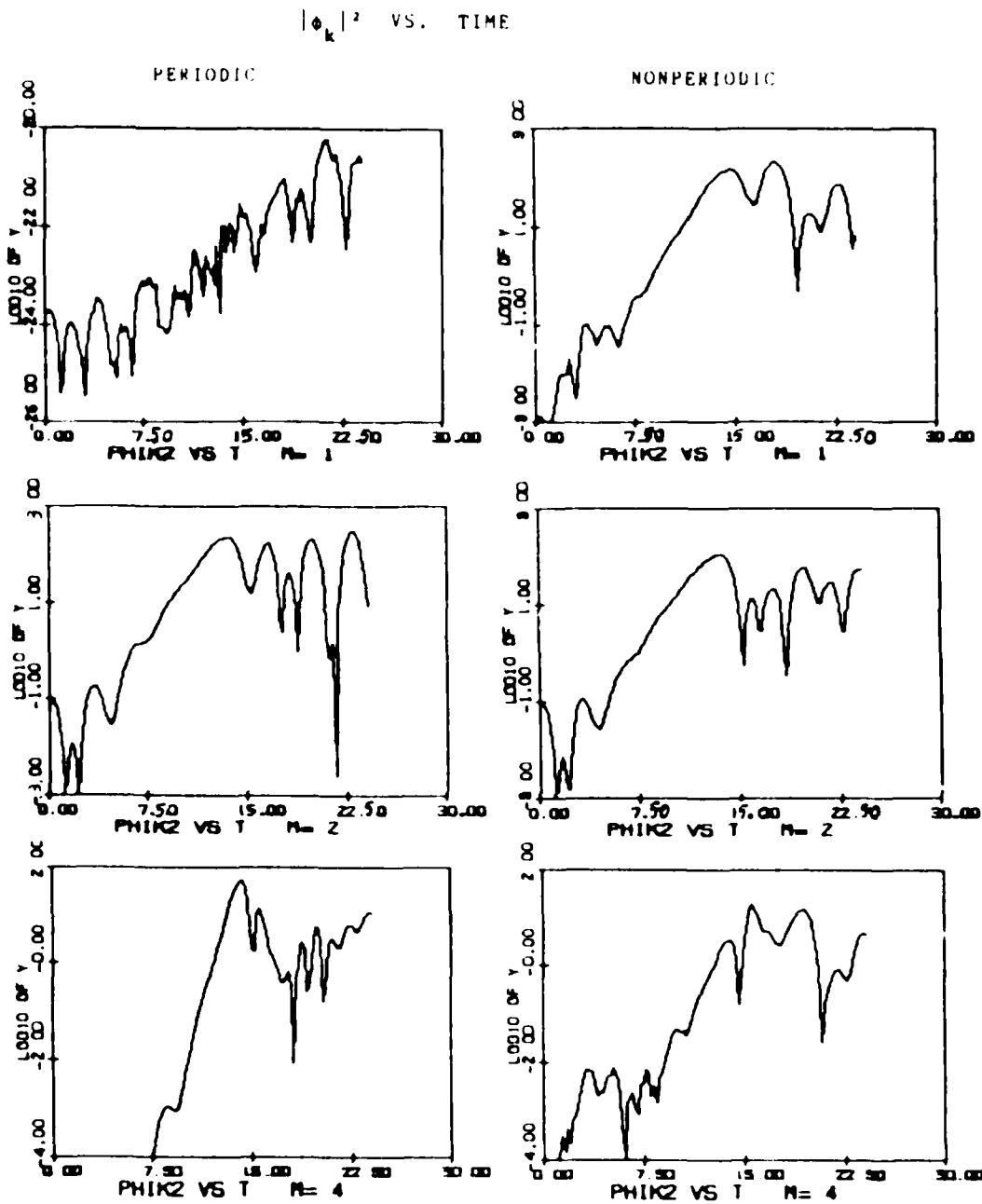


Figure 1. Log, base 10, of the modulus squared of spatial Fourier modes 1, 2, and 4 of the electrostatic potential as a function of time from the periodic simulation (left) and the nonperiodic simulation (right).  
 $k_n = 2n\pi/L = n/2$  for these simulations.

Phase Space Snapshots of Right-Going Species

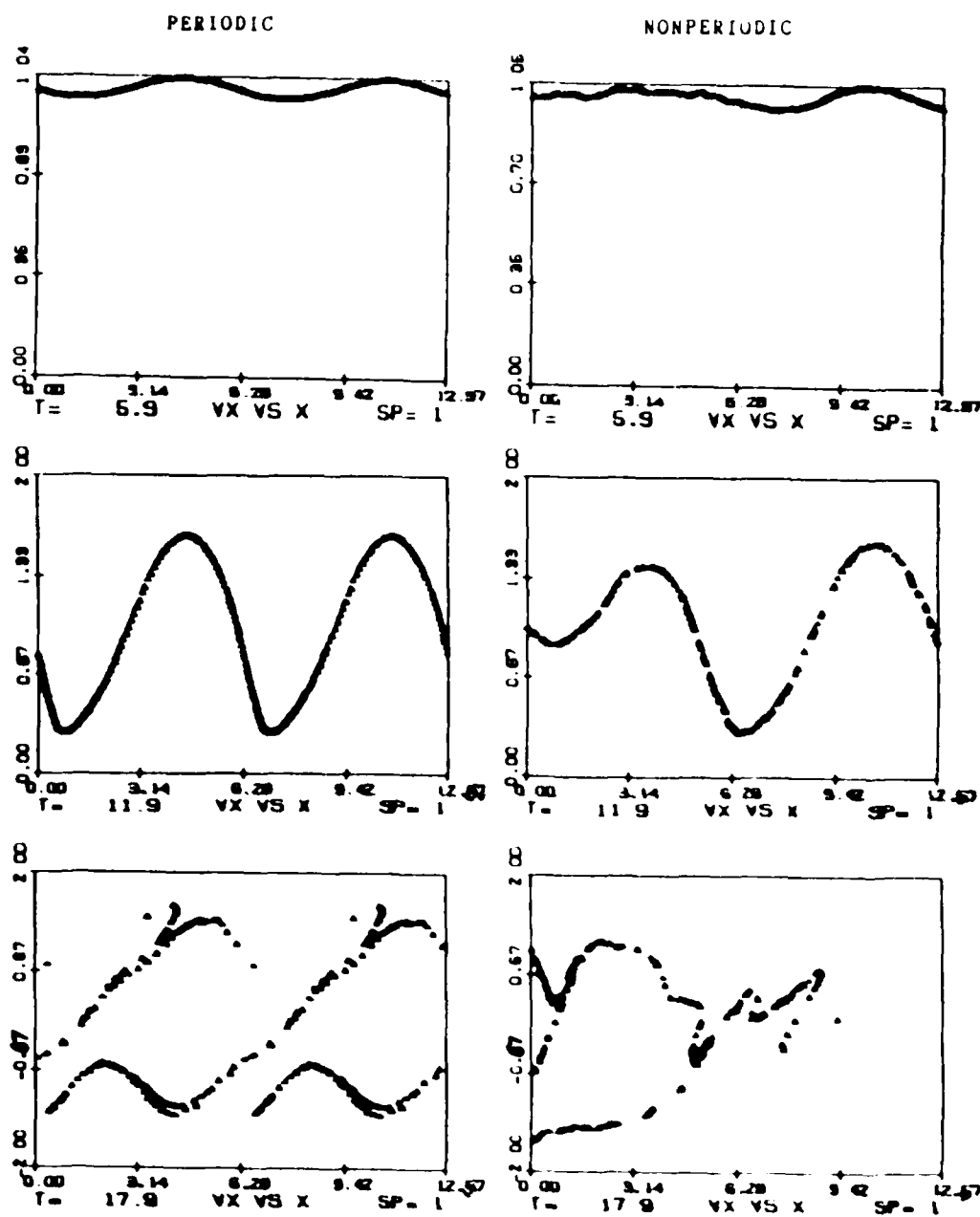


Figure 2. Phase space (velocity in the simulation direction vs. position for each of the particles in the simulation box) at three different times for right-going particles from the periodic (left) and nonperiodic (right) simulations.

Phase Space Snapshots of Left-Going Species

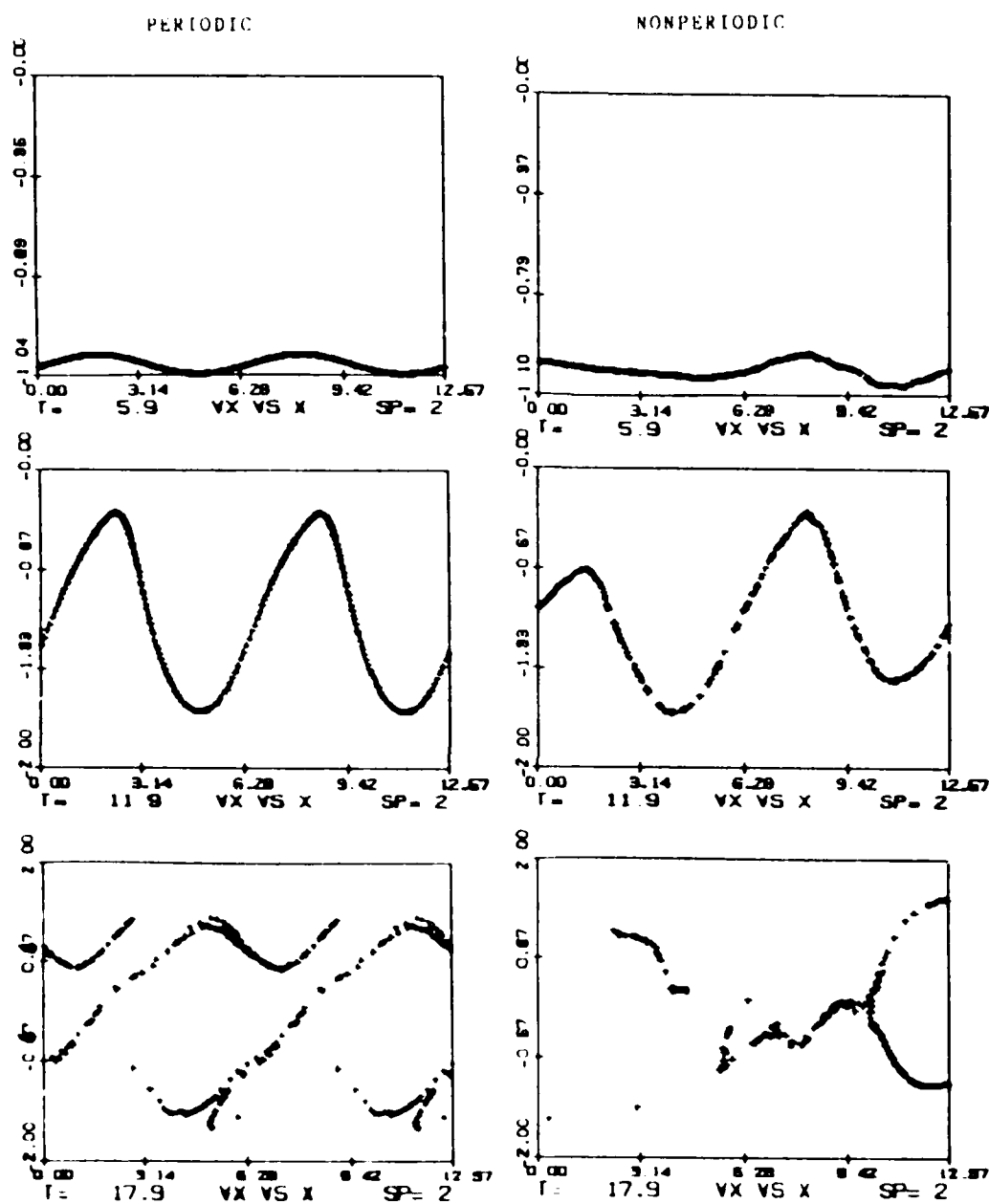


Figure 3. Same as Figure 2, but for the left-going particles.

Snapshots of Electrostatic Potential vs. Position

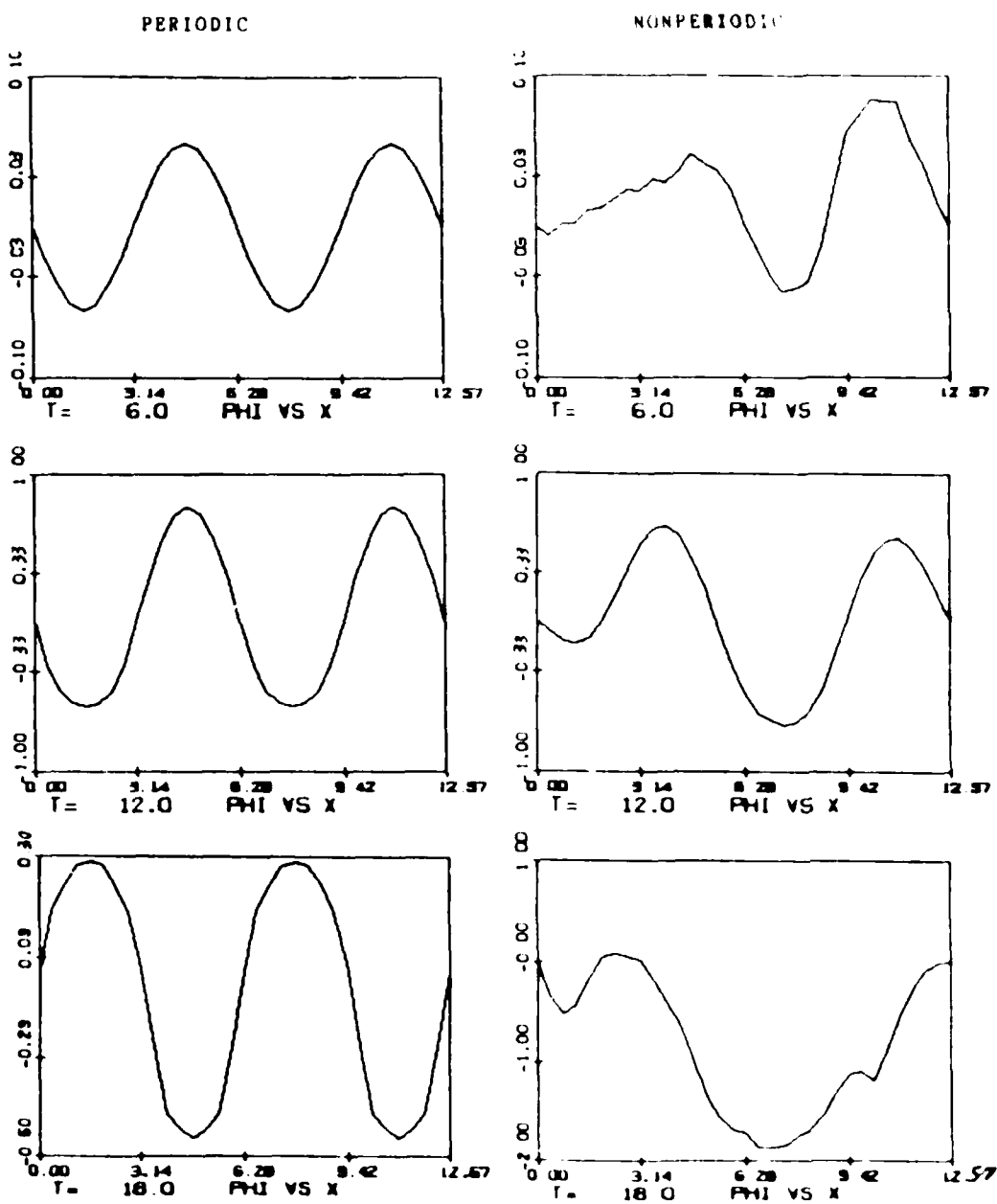


Figure 4. Electrostatic potential vs. position at three different times in the periodic simulation (left) and nonperiodic simulation (right).

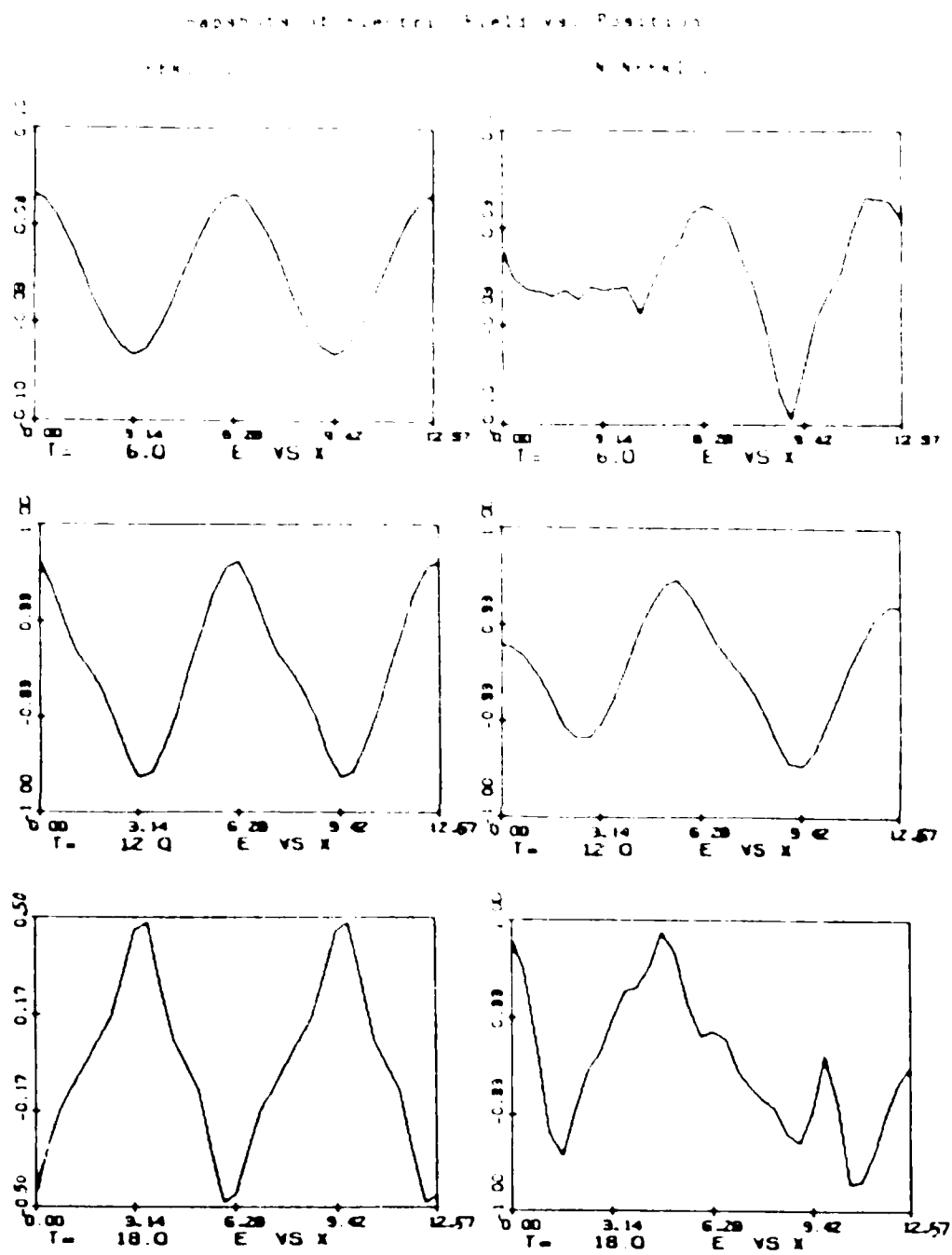


Figure 5. Electric field vs. position at three different times in the periodic simulation (left) and nonperiodic simulation (right).

A

N

D

6

—

87

D T I C